THE UNIVERSITY *of* EDINBURGH

Study of the N=Z nucleus ^{62}Ga using a new fast beta-decay tagging system

Helena May David

Thesis submitted for the degree of
Doctor of Philosophy
at
The University of Edinburgh

June 2013

Abstract

Several low-lying levels in the exotic N = Z nucleus ^{62}Ga have been observed for the first time using a new fast β-decay tagging system at the Argonne National Laboratory. The system provides enhanced selectivity on proton-rich nuclei, produced in heavy-ion fusion-evaporation reactions, that exhibit 'fast' β decays compared with isobaric contaminants. A 103 MeV beam of ^{40}Ca ions, produced by the Argonne Tandem-Linac Accelerator System (ATLAS), was used to bombard an isotopically enriched ^{24}Mg target, allowing ^{62}Ga nuclei to be produced via the evaporation of one proton and one neutron in heavy-ion fusion-evaporation reactions. Prompt γ rays were detected by the Gammasphere array, and recoiling reaction products dispersed by their mass-to-charge ratio by the fragment mass analyzer (FMA). New β-tagging capabilities were provided by the installation of a 1 mm thick, highly segmented 160×160 double-sided Silicon strip detector (DSSD) at the focal plane of the FMA, which allowed implanted reaction residues to be correlated in both space and time with subsequent β^+ decays. The experiment was carried out with the benefit of digital acquisition systems for the Gammasphere, FMA and DSSD.

The exotic nucleus ^{62}Ga has a β-decay half-life of $\sim$ 100 ms. The main contaminants in the ^{40}Ca + ^{24}Mg fusion-evaporation reaction are ^{62}Zn, which has a $\sim$ 9 hour half-life, and ^{58}Ni, which is stable. A clean 'singles' γ-ray spectrum of ^{62}Ga transitions was made permissible for the first time by the high levels of selectivity achieved, through requiring the detection of a β particle in the DSSD in close proximity to implanted reaction residues within 400 ms of implantation. Several low-lying low-spin states are reported in this thesis work, and discussed in the context of previous experimental results and theoretical predictions made using shell model, deformed shell model and IBM-4 calculations.

Lay summary

A chemical element is uniquely identifiable by the number of protons present within its nucleus. Variants of a chemical element that have the same number of protons but different numbers of neutrons are called 'isotopes'. At present, 118 different chemical elements have been discovered, and over 7000 different isotopes of these elements are expected to exist. Many isotopes are in stable configurations, so that the number of protons and neutrons in the nucleus does not change over time. However, many are in unstable configurations, and undergo radioactive decay to become more stable.

Light nuclei with similar numbers of protons and neutrons tend to be stable, but more neutrons than protons are required in the atomic nucleus for stability in heavier nuclei. All but the lightest nuclei with similar numbers of protons and neutrons are known as 'proton-rich', and are typically very unstable. Studying these exotic nuclei gives an insight into interesting physics effects not exhibited by other types of nuclei. As neutrons and protons are almost identical particles, except that the proton has positive charge and the neutron has no charge, nuclei with similar numbers of protons and neutrons possess a special symmetry, known as 'isospin symmetry', that reveals fundamental properties of nuclear structure. Proton-rich nuclei are also very important in explosive astrophysical sites, such as novae and X-ray bursts.

This thesis presents the results of a study of the nucleus ^{62}Ga, which has equal numbers of protons and neutrons and is very unstable. A typical ^{62}Ga nucleus only survives for about 0.1 seconds before decaying into a different chemical element. The experiments described in this thesis were carried out using a new experimental system installed at the Argonne National Laboratory, which takes advantage of the very fast decays exhibited by ^{62}Ga to isolate it from contaminants that do not display the same fast decays. A significant extension to the current knowledge of the nuclear structure of ^{62}Ga has been obtained in this way.

Declaration

The experiments described in this thesis were performed by myself, fellow members of the Edinburgh University Nuclear Physics Group and collaborators at the Argonne National Laboratory. I declare that the analysis and interpretation of the results contained herein are my own except where explicitly stated otherwise in the text, and that I composed this thesis. No portion of this work has been submitted for any other degree or professional qualification.

(*Helena May David, June 2013*)

Acknowledgements

I would like to thank my supervisor, Prof. Philip Woods, for teaching me a great deal over these recent years, for strengthening my abilities as a scientist and for making this thesis possible.

I would also like to thank my second supervisor, Dr. Gavin Lotay, for the many valuable discussions we have had and for sharing his expertise on all matters of γ-ray spectroscopy.

I would like to thank the staff and students in the Edinburgh Nuclear Physics Group, both past and present, for their unwavering support and encouragement. In particular, I thank Tom Davinson, Alex Murphy, Dan Watts, Marialuisa Aliotta and Dan Doherty for their valued and appreciated contributions to my studies.

I would like to thank my collaborators at the Physics Division at the Argonne National Laboratory for their unrivalled professionalism and their support during experiments and during my studentship at the Division. In particular, I thank Dr. Darek Seweryniak, who has played an essential role in the success of this thesis work, for his guidance in matters both technical and scientific and for his patience.

I would like to thank my family and those close to me, especially Paul, for making the difficult times bearable and the good times wonderful.

Finally, I am deeply thankful to my parents, Nick and Jacqueline, for teaching me to follow my heart without fear and never to stop learning.

Contents

List of Figures

List of Tables

Chapter 1

Introduction

Developments in humanity's understanding of the universe go hand in hand with technological advancements. For hundred of years, scientists have driven advances in experimental capabilities to explore aspects of physical phenomena that are out of reach with the available technical knowledge. The development of accelerated beam facilities and detector technology has made large areas of the nuclear terrain accessible for study in the laboratory using a wide variety of experimental techniques. However, nuclear properties of many exotic nuclei at the utmost limits of stability remain elusive with contemporary methods. Innovative new methods must therefore be conceived in order to further extend our knowledge of exotic nuclei, which are known to exhibit a diverse array of nuclear physics phenomena. Structure information for a wide range of exotic nuclei allows systematic trends to be identified that would not become apparent with information only for localised regions.

The limits of nuclear existence are defined by the proton and neutron drip-lines, which are the boundaries either side of the valley of stability at which nuclei become unstable with respect to ground-state nucleon emission. The neutron drip-line lies much farther from the valley of stability than the proton drip-line as protons experience Coulomb repulsion from other protons in the nucleus, resulting in acute differences in nuclear physics effects exhibited by exotic nuclei at the opposing limits [1]. Although the neutron drip-line has only been experimentally investigated up to ^{31}F [2] due to its considerable distance from the valley of stability, several interesting phenomena have nevertheless been uncovered. The exotic nucleus ^{11}Li is the heaviest bound Lithium isotope, and therefore lies on

the neutron drip-line. In the 1980s, ^{11}Li was found to have a matter radius comparable in size to ^{208}Pb [3]. This effect, known as a two-neutron 'halo', is attributed to two weakly bound neutrons, as depicted in Figure 1.1. Recently, the neutron drip-line nucleus ^{22}C was also shown to exhibit a two-neutron halo [4]. Several other nuclei have also been identified as exhibiting neutron-halos, including ^{6}He, ^{11}Be, ^{14}B and ^{17}B [5]. Although the formation of proton halos is hindered by electrostatic effects and thus proton halo nuclei are rare, ^{8}B, ^{12}N and ^{17}Ne have been found to exhibit this phenomenon. A recent review of experimental progress in studies of halo nuclei can be found in [6].

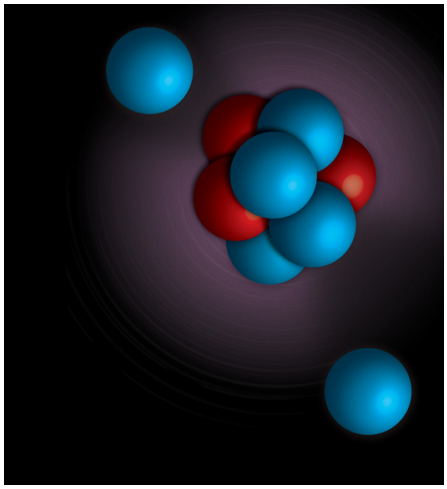

Figure 1.1 Depiction of the ^{11}Li two-neutron halo, taken from [7].

Evidence of new shell closures have also been identified in neutron drip-line nuclei. The nucleus ^{24}O behaves as though doubly-magic, with apparent shell closures at $Z = 8$ and $N = 16$ [8]. Studies of heavier neutron drip-line nuclei are expected to uncover more phenomena, such as 'pygmy dipole resonances' and de-coupled halo configurations [9].

Along the proton drip-line, a rather different array of nuclear physics effects are exhibited. Although light nuclei with $N \sim Z$ lie in, or close to, the valley of stability, heavier nuclei with $N \sim Z$ up to the region of the doubly-magic $N = Z$ nucleus ^{100}Sn lie close to the proton drip-line. As such, interesting isospin effects are apparent in this region, particularly for self-conjugate nuclei. Shape coexistence is also exhibited in some nuclei with $N \sim Z$ in the mass $A = 34 - 40$ region due to large shell gaps for deformed nuclei with nucleon numbers of 34 and 36 (oblate) and 38 and 40 (prolate), in addition to the spherical shell gap at $N, Z = 40$ [10]. Krypton isotopes of mass 72-78 [11–13] and Selenium isotopes of mass 68, 70 and 72 [14, 15] have been shown to exhibit this phenomenon.

β-decay Q-values become very large close to the proton drip-line, allowing exotic decay modes to occur [1]. For example, β-delayed one-, two- and three-proton emission from the proton-rich nucleus ^{45}Fe has recently been observed [16]. Several nuclei that exhibit one- and two-proton ground-state decays have also been identified [17]. Additionally, a recent study of the β^+ decay of the doubly-magic proton-rich nucleus ^{100}Sn reported the lowest $\log_{10} ft_{1/2}$ value observed to date [18]. Superallowed α decays are also predicted to occur in the ^{100}Sn region [17].

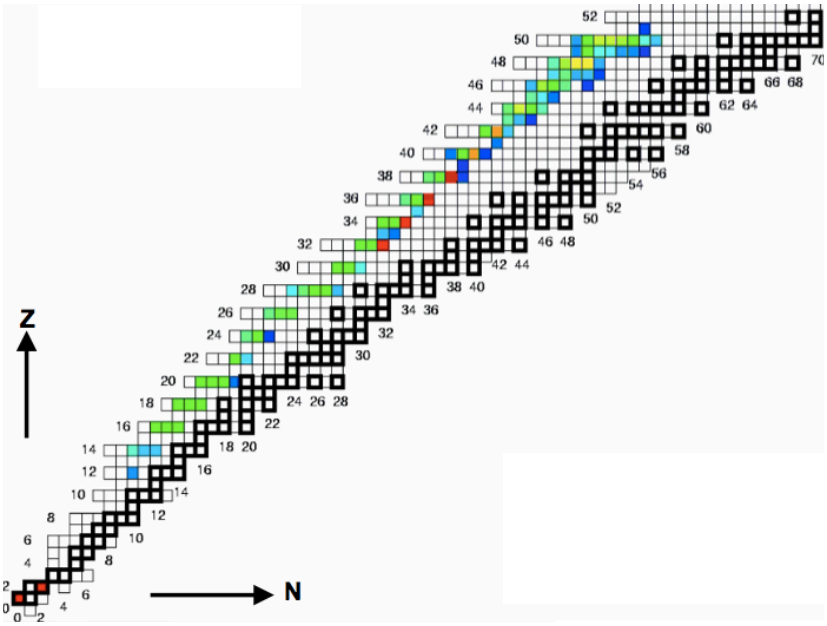

Figure 1.2 Possible rp-process reaction path [19]. Stable isotopes are indicated by black squares.

Nuclei close to the proton drip-line are crucial in both quiescent and explosive astrophysical scenarios. For example, Solar models require a very high degree of precision of the rate of the ^{7}Be(p, γ)^{8}B reaction, as this value critically affects the Solar neutrino flux [1, 20]. Explosive astrophysical scenarios such as novae, X-ray bursts (XRBs) and X-ray pulsars are possible sites for the astrophysical 'rp-process' [21]. The rp-process consists of a series of rapid proton and α capture reactions, interspersed with β^+ decays, that drives the reaction path close to the proton drip-line [22]. A possible reaction path for the rp-process is shown in Figure 1.2.

Nuclear properties such as masses, lifetimes, level densities and spin-parities of states for many nuclei close to the proton drip-line must be known to fully understand the rp-process. XRBs occur in binary stellar systems where a compact

neutron star accretes Hydrogen- or Helium-rich material from a companion star [23]. Type I XRBs occur when accretion rates are less than 10^{-9} $M_{\odot}$ per year [21], and are characterised by extremely energetic ($\sim 10^{39}$ ergs) 'bursts' of X-ray radiation that recur in a very regular fashion on a timescale of hours-days. The bursts themselves last for tens to hundreds of seconds, and are the result of a thermonuclear runaway under the extreme temperature ($\geq 10^{9}$ K) and density ($\rho \sim 10^{6}$ g/cm^{2}) conditions on the surface of the neutron star [24]. A recent review of type I XRBs can be found in [25]. Although the large gravitational potential generated by neutron stars is thought to prevent the rp-process from contributing to the chemical composition of the universe, knowledge regarding the rp-process is nevertheless crucial in understanding energy generation in, for example, XRB scenarios. Additionally, the chemical composition of the ashes that remain on the surface of the neutron star as a consequence of the rp-process are critically affected by the precise path and rate of progression of the thermonuclear reactions that constitute the rp-process [21].

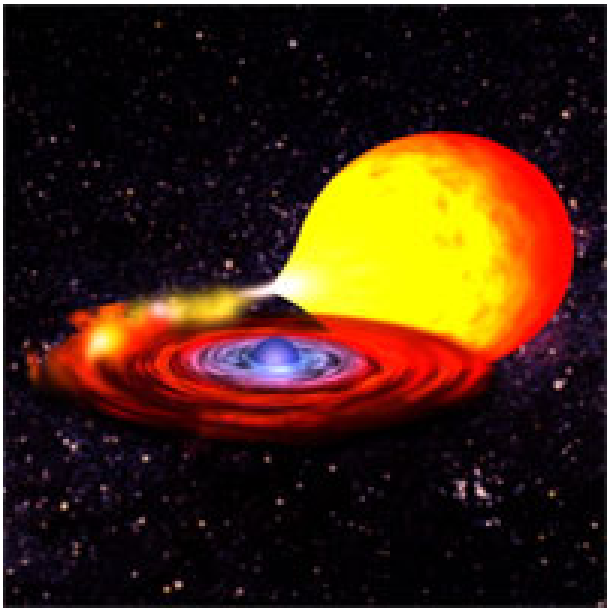

Figure 1.3 Artist's impression of an X-ray burst [26].

It is thought that proton-rich $T_z = -1$ nuclei (where $T_z = \frac{1}{2}(N - Z)$) in particular play a critical role in XRB scenarios [21, 27]. For example, a recent theoretical study by Parikh *et al.* highlighted the radiative proton capture reactions ^{61}Ga$(p,\gamma)^{62}$Ge and ^{65}As$(p,\gamma)^{66}$Se as reactions that critically affected the chemical yields generated in XRBs [24]. As such, detailed structure information for states above the proton threshold in the $T_z = -1$ nuclei ^{62}Ge and

^{66}Se is required. However, only limited information regarding the lowest-lying $2^+ \rightarrow 0^+$ transition has been recently reported for ^{66}Se [28], and no confirmed structure information has been obtained for ^{62}Ge. Consideration of mirror nuclei indicates that level densities in the astrophysically relevant energy regions are very low, rendering statistical methods, such as Hauser-Feshbach calculations [29], inappropriate in these cases [1]. Indeed, the proton capture reaction rates may be dominated by a single resonance.

Nuclei along the N = Z line

As discussed earlier in this Chapter, many nuclei up to ^{100}Sn that lie close to the proton drip-line have similar numbers of neutrons and protons. The effects of isospin symmetry are therefore particularly evident in exotic nuclei with N $\sim$ Z as neutrons and protons occupy similar orbitals resulting in the enhancement of shell effects. In particular, the neutrons and protons in nuclei with N = Z occupy identical single-particle levels [30, 31], providing an ideal environment for isospin effects to be investigated.

Although like-nucleon pairs are known to dominate in nuclei that do not lie close to the N = Z line, neutron-proton (np) pairing plays a dominant role in nuclei with N $\sim$ Z [10]. Odd-odd nuclei with N = Z are of particular interest, as np pairs can couple to a total isospin, T, of either 0 or 1. The precise role of T = 0 np pairs in N = Z nuclei remains unknown. Competition between T = 0 and T = 1 states occurs at low excitation in odd-odd N = Z nuclei. In fact, all known odd-odd nuclei with N = Z with A $>$ 40 have T = 1 ground states (with the exception of ^{58}Cu).

As isospin plays such an important role in nuclei with N $\sim$ Z, theoretical models in recent years have endeavoured to include 'good' descriptions of isospin [32, 33]. Advances in experimental capabilities play a fundamental role in measuring properties of exotic nuclei close to N = Z, highlighting the limitations of current understanding and predictive powers of the most recent models. For example, T = 1 dominance in the odd-odd N = Z nuclei ^{82}Nb and ^{86}Tc was inferred through experimentally determined properties of low-lying states in a recent study [30, 34].

A consequence of isospin symmetry is the considerable similarity of the structure of 'mirror nuclei' - nuclei with the number of protons and neutrons interchanged.

Isobaric sets of nuclei with $T_z = -1$, 0 and 1, known as isobaric triplets, must all have $T = 1$ states with almost identical properties due to isospin symmetry. In-depth information regarding isospin-breaking effects can be obtained through detailed knowledge of Coulomb energy differences (CEDs) between isobaric analogue states for members of the same triplet [35].

As discussed in the previous Section, nuclei close to the proton drip-line play a fundamental role in the astrophysical rp-process. It is thought that the path of the rp-process may be driven up to the region of the N = Z nucleus ^{100}Sn. Studies of nuclei with $A \sim 100$ close to the N = Z line, expected to be possible with the advent of new radioactive beam facilities, is highly anticipated.

Experimental considerations and challenges

Studying exotic nuclei near the proton drip-line in the laboratory presents a number of experimental challenges. An initial consideration must be a choice of reaction that will populate the nuclei of interest with a large enough cross-section to make experimental measurements feasible. Once a suitable reaction is identified, an appropriate detector configuration providing the means to obtain the desired nuclear structure information must be available. Cross-sections of exotic nuclei close to the proton drip-line are typically many orders of magnitude smaller than cross-sections of competing reaction channels. As such, methods of providing selectivity on the reaction channel of interest must be devised in order to reduce levels of contamination from unwanted species.

To obtain nuclear structure information through measuring γ-ray radiation, a suitable reaction must be chosen that will populate the nuclei of interest in excited states. As increasingly heavy stable nuclei have an increasing value of N/Z, the fusion of two lighter stable species produces neutron deficient nuclei in the region of the N = Z line. The fused 'compound' nucleus is produced in an excited state, and can subsequently de-excite through the evaporation of light particles. The logistics of this type of reaction, known as 'heavy-ion fusion-evaporation reactions', are often simplified by the use of stable target and beam configurations. For successful fusion of target and beam nuclei to occur, the energy in the centre of mass must exceed the Coulomb barrier. The resulting compound nucleus has a lifetime $> 10^{-20}$ s, allowing thermal equilibrium to be reached and all "memory" of the mode of production to disappear. De-excitation of the compound nucleus

can then occur via high energy γ-ray emission or the emission of protons, neutrons or α particles. The emission of charged particles is hampered by the Coulomb barrier, whereas neutron emission is inhibited by a growing neutron separation energy for nuclei produced increasingly further away from stability. Cross-sections for various particle evaporation channels range across several orders of magnitude depending on the number and type of particles emitted, typically from tens of nanobarns to tens of millibarns.

Structure information for all odd-odd N = Z nuclei from ^{46}V to ^{78}Y has been obtained using heavy-ion fusion-evaporation reactions [31, 36–41]. However, high-spin states are preferentially populated in heavy-ion fusion-evaporation reactions due to the large amount of angular momentum transferred to the compound nuclei. Although charge transfer reactions, such as (p,n) reactions, can be used for low-spin studies, a lack of stable target material past A = 58 means (p,n) studies of heavier odd-odd N = Z nuclei are not feasible without radioactive beam facilities. The situation is articulated well in a 2001 theory paper by Juillet, Van. Isacker and Warner, where it is noted that "...[a limitation of the experimental techniques currently used to access the N = Z line] stems not only from the high sensitivity required but also from the nature of the reactions used to populate the nuclei of interest, which yield information only on the yrast structure" [33].

In recent decades, very powerful γ-ray spectrometers have been coupled with recoil-separators, which disperse recoiling reaction products by their mass-to-charge ratio (A/Q), to gain structure information for nuclei close to the proton drip-line. Although additional information regarding the recoiling reaction products can be obtained using ionisation chambers and other ancillary detectors, only limited Z resolution can be obtained for all but relatively light nuclei. As such, isobaric contamination remains a significant issue, with the γ rays of interest swamped by those emitted from contaminant isobars. Selectivity on exotic nuclei near the N = Z line has been achieved using arrays of particle detectors, allowing events where evaporated particles are associated with reaction channels of contaminant nuclei to be vetoed. However, these traditional methods do not provide levels of cleanliness sufficient to produce 'singles' γ-ray spectra. Structure information has then been obtained through the requirement of γ-ray coincidences with strong known transitions. Several non-yrast states in the exotic N = Z nucleus ^{62}Ga have been observed in this way in recent decades [31, 42, 43]. However, limitations on the extent of information regarding non-yrast structure arise due to the requirement of coincidences with strong known transitions.

The experimental technique of 'recoil decay tagging' (RDT) has been used to great success obtaining structure information for exotic nuclei with N $\sim$ Z in the last 30 years [1]. The technique takes advantage of proton, α, or β-delayed particle characteristic decay modes exhibited by exotic nuclei to provide increased levels of selectivity on the nuclei of interest. A typical RDT experimental setup, shown in Figure 1.4, consists of a large γ-ray array surrounding a target, which detects prompt γ rays emitted following heavy-ion fusion-evaporation reactions, coupled with a recoil-separator to provide A/Q selectivity. A position and time sensitive Silicon detector, installed at the focal plane of the recoil-separator, is then used to correlate implanted reaction products with their subsequent characteristic decay modes.

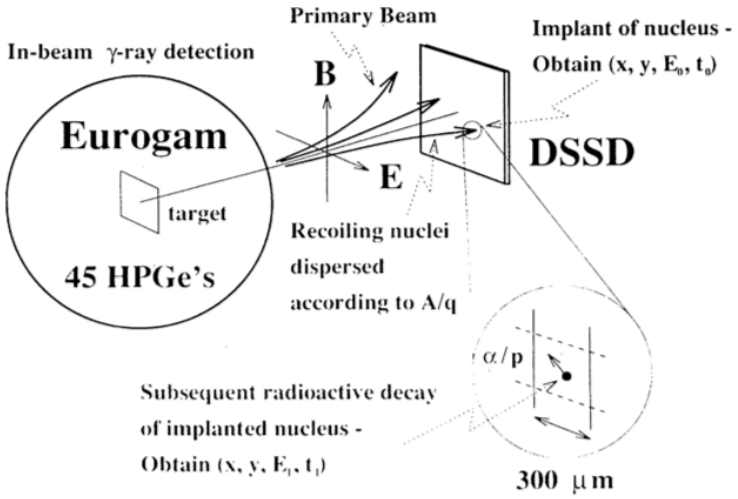

Figure 1.4 Typical recoil decay tagging system [44].

It might seem a natural progression from studying nuclei that exhibit proton, α or β-delayed particle decay modes, to nuclei that exhibit β decays. This technique, known as recoil beta tagging (RBT), was successfully developed in recent years at the Jyväskylä laboratory (JYFL), and used to study the structure of the odd-odd N = Z nuclei ^{74}Rb and ^{78}Y [41]. However, tagging with β particles presents a number of challenges not encountered in traditional RDT methods due to the nature of the positrons themselves, as will be discussed in Chapter 5.

In the present work, a significant extension of the low-lying level scheme of the exotic N = Z nucleus ^{62}Ga has been obtained using a new fast β-decay tagging system designed to provide selectivity on β-unstable proton-rich nuclei at the ATLAS facility at the Argonne National Laboratory. The new system

uses the Gammasphere detector array to detect prompt γ rays, coupled with the Argonne fragment mass analyzer (FMA) to provide A/Q discrimination on reaction products. A highly segmented 160×160 double-sided Silicon strip detector (DSSD), installed at the focal plane of the FMA, allows implanted reaction products to be correlated with subsequent β decays.

The exotic nucleus ^{62}Ga is a member of an isobaric triplet that also contains ^{62}Ge and ^{62}Zn. The 2^+ and 4^+ isobaric analogue states to the 2^+ state at 954 keV and the 4^+ state at 2186 keV in ^{62}Zn have not been confirmed in either ^{62}Ga or ^{62}Ge. ^{62}Ga has a world-averaged β-decay half-life of 116.121(21) ms [45]. High-precision values of the half-life for ^{62}Ga are available as the superallowed Fermi decay of ^{62}Ga is used to determine matrix elements in the Cabibbo-Kobayashi-Maskawa (CKM) matrix [46]. The $T_z = -1$ nucleus ^{62}Ge has a half-life of 129(35) ms [47]. In contrast to the 'short' ($\sim$100 ms) half-lives exhibited by ^{62}Ga and ^{62}Ge, the isobar ^{62}Zn has a 'long' $\sim$ 9 hour half-life, making the new system ideal for studies of the mass A = 62 isobaric nuclei. Several new states in ^{62}Ga have been identified using the new experimental system.

Chapter 2

Theoretical considerations and models

2.1 Modelling the nuclear landscape

As of 2012, 118 distinct chemical elements and a total of ∼3000 isotopes have been discovered. Current estimates, however, predict that the number of bound nuclei with $2 \leq Z \leq 120$ approaches 7000 [48].

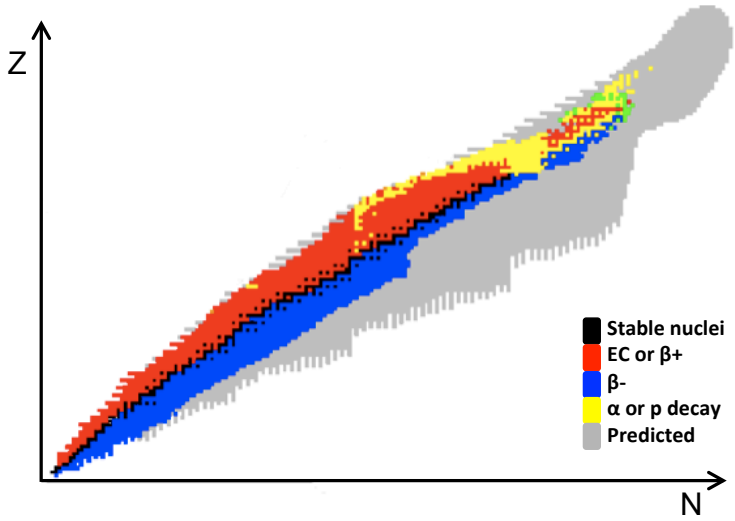

Figure 2.1 Chart of nuclides, adapted from [49].

The Segré chart shown in Figure 2.1 provides a means of 'mapping' nuclei, with stable nuclei indicated by black squares and the various decay modes exhibited

by unstable nuclei denoted by coloured boxes. Away from the valley of stability, increasing the excess of protons or neutrons causes nuclei to become increasingly unstable until eventually the limits of the nuclear landscape are met. The nuclear binding energy, defined as the energy required to break up a nucleus into its constituent neutrons and protons, is a useful measure of nuclear stability. The realisation in the 1920s that bound nuclei have less mass than the sum of the constituent nucleon masses was critical to our understanding of nuclear reactions, and provided the first inklings about the source of energy in the Sun. For a nucleus with N neutrons and Z protons and atomic mass $\mathrm{M}\left(\mathrm{N},\mathrm{Z}\right)$, the nuclear binding energy $\mathrm{B}\left(\mathrm{N},\mathrm{Z}\right)$ is given by

$$\mathrm{B}\left(\mathrm{N},\mathrm{Z}\right) = \mathrm{Z}\mathrm{M}_{\mathrm{H}}c^2 + \mathrm{N}\mathrm{M}_{\mathrm{n}}c^2 - \mathrm{M}\left(\mathrm{N},\mathrm{Z}\right)c^2, \tag{2.1}$$

where M_{H} is the mass of the hydrogen atom, and M_{n} is the mass of the neutron. The binding energy per nucleon as a function of A for stable nuclei in their ground states, shown in Figure 2.2, is not smooth, with the most stable nuclei residing at the peaks, reaching a maximum value for ^{62}Ni.

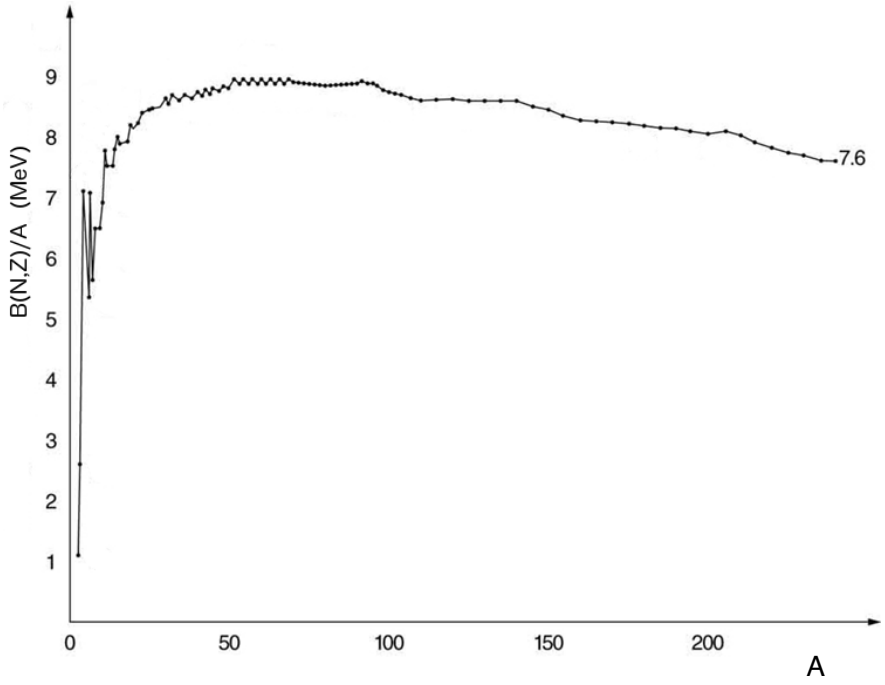

Figure 2.2 Binding energy per nucleon for stable nuclei, adapted from [50].

At the extreme limits of stability lie the proton and neutron drip-lines, beyond which nuclei are susceptible to the spontaneous ground state emission of protons and neutrons, respectively. These boundaries describe the point at which the separation energy for nucleons, defined by the energy required to remove a

nucleon, becomes negative. The separation energies for a single proton, S_p, and for a single neutron, S_n, are given by

$$S_p = B(N, Z) - B(N, Z-1), \tag{2.2}$$

and

$$S_n = B(N, Z) - B(N-1, Z), \tag{2.3}$$

where B is the binding energy as given in equation 2.1. Although nuclei beyond the drip-lines can exist, they are unstable with respect to ground state nucleon emission.

2.1.1 The liquid-drop model

The empirical observations shown in Figure 2.2 give physicists the first clues regarding the extremely complex nature of the structure of nuclei, and any successful model must have the ability to reproduce these features, as well as global trends. The Weizsäcker semi-empirical mass formula (SEMF), given in equation 2.4, provides a good approximation of the nuclear binding energy.

$$B(N, Z) = \alpha_1 A - \alpha_2 A^{2/3} - \alpha_3 \frac{Z(Z-1)}{A^{1/3}} - \alpha_4 \frac{(N-Z)^2}{A} + \delta. \tag{2.4}$$

The first three terms in the SEMF are based upon the liquid-drop model, the first nuclear mass model, which proposes that a nucleus could be described as analogous to an incompressible droplet of liquid with uniform density. The first term gives a first order approximation as the binding energy per nucleon is relatively constant with the exception of very light nuclei, hence $B(N, Z) \approx \alpha_1 A$, where α_1 is a constant of the order of 8 MeV. An implication of the approximately linear relationship between binding energy and mass is that nucleons interact only with their nearest neighbours, and not all other nucleons in the system which would result in an $\sim A^2$ dependence. In the liquid-drop model, however, nucleons close to the surface of the nucleus will have fewer neighbouring nucleons than those in the interior, causing the first term to overestimate the binding energy. The second term in equation 2.4 is proportional to the surface area and accounts for the effect of the smaller contribution to the binding energy from surface nucleons, allowing the sharp decline in binding energy per nucleon for very light nuclei to be described. The third term takes Coulomb repulsion between the protons in the nucleus into account. The Coulomb potential of a uniformly charged sphere,

which can be used to approximate the Coulomb potential of a nucleus, can be shown to equal $\frac{3}{5}\frac{1}{4\pi\epsilon_0}\frac{Q^2}{R_0 A^{1/3}}$, where $R_0 \approx 1.2$ fm. As each proton repels all of the other protons, the total charge Q squared can be evaluated as $Ze(Z-1)e$. The constant α_3 is approximately 0.7 MeV, and the negative sign in the third term indicates that the Coulomb repulsion term reduces the binding energy. The fourth term has no basis in the liquid-drop model, instead arising from quantum mechanical considerations. A consequence of the Pauli exclusion principle is that stable nuclei have N ≈ Z (in particular for light species) in order to minimise the total energy of the system. The fourth term corrects for nuclei with an imbalance of neutrons and protons, with lessening effect for increasing values of A. The final term is purely based on the empirical observation of a tendency for like nucleons to pair together, resulting in a more stable configuration. The value of δ is given by $+\alpha_5 A^{-1/2}$ if both Z and N are even, $-\alpha_5 A^{-1/2}$ if both N and Z are odd, and 0 otherwise.

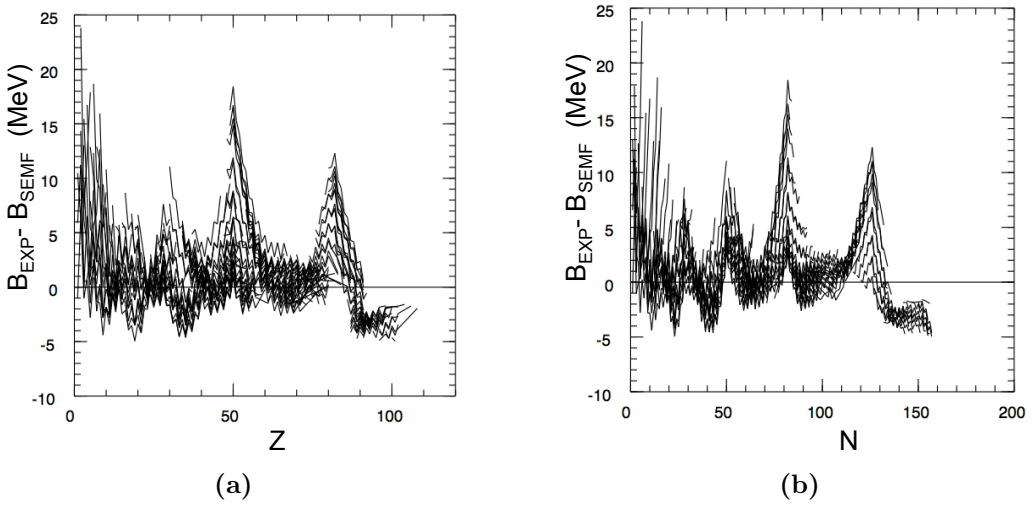

Figure 2.3 Difference in binding energy between experimental values and SEMF values for a) proton number and b) neutron number [51].

A comparison of the binding energies given by the SEMF with the observed values, shown in Figure 2.3, provides clues as to where the model is failing. It is clear from the Figure that nuclei with 28, 50 or 82 protons have significantly larger binding energies than predicted, with similar behaviour for the number of neutrons, except with the addition of another strongly bound feature at N = 126. Several other experimental results offer strong support to the hypothesis that nuclei with these 'magic' numbers of nucleons are particularly stable, including discontinuities in nucleon separation energies and an increase in excitation energy for the first excited states. Detailed analyses of the empirical data indicate that the numbers

2, 8, 20, 28, 50, 82 and 126 are magic. It was the pursuit of an understanding of the unusual behaviour of nuclei with magic numbers of nucleons that resulted in the development of the shell model, which is comparable in many respects with the atomic shell model and successfully describes much of the observed behaviour in nuclei.

2.1.2 The shell model

The shell model of the nucleus presents a simple picture that energy levels within a nucleus are filled with nucleons from the lowest energy states upwards. This microscopic approach to tackling the structure of nuclei allows a detailed description of the behaviour of individual nuclei that deviate from the average, unlike the macroscopic approach taken in the liquid-drop model that describes collective behaviour. In this picture of filled energy levels, the magic numbers can be attributed to the point at which a shell is completely filled with nucleons. The energy of the levels within the nucleus are determined by solving the many-body Schrödinger equation, with a suitable choice of potential. The choice of potential is critical to the success of the model and will be discussed in more detail. The independent motion in well defined orbits of each nucleon in a mean-field potential created by all nucleons in the system is an important assumption of the shell model, and might at first seem unmerited due to the close proximity of the nucleons. However, the Pauli principle greatly reduces the possibility of collisions resulting in energy transfer between nucleons as all states with lower energy are fully occupied.

At this point it is important to clarify some of the terminology used in the context of nuclear structure. An energy 'state' is a single solution to the Schrödinger equation, uniquely characterised by the quantum numbers n, l, j and m, which are the principle, orbital angular momentum, total angular momentum and magnetic quantum numbers, respectively. The values of the angular momentum quantum number $l = 0, 1, 2, 3, 4, 5, 6$ and 7 are represented by the spectroscopic notation s, p, d, f, g, h, i and j, respectively. A collection of energy states with the same n, l and j are 'orbits' denoted by the notation nl_j, for example $1f_{5/2}$. A 'shell' is then given by a collection of orbits that are close together in energy, for example the pf-shell.

As mentioned previously, a mean-field nuclear potential that describes the force felt by nucleons within the nucleus must be chosen. The nuclear potential should

be roughly constant within the confines of the nucleus and become 0 at a point beyond the nuclear radius, decreasing gradually over the range of the strong force. Once the form of the interaction, $V(r)$, is chosen, the single-particle energy levels are then given by solutions to the 3-dimensional Schrödinger equation:

$$\left\{ \frac{-\hbar^2}{2m}\nabla^2 + V(r) \right\} \psi(r) = E\psi(r). \tag{2.5}$$

The single-particle energies calculated using a simple harmonic oscillator central potential, given by

$$V(r) = \frac{1}{2}m\omega^2 r^2, \tag{2.6}$$

where ω is the oscillation frequency, are shown in Figure 2.4. The Schrödinger equation can be solved easily in this case, yielding solutions in the form

$$E_n = \hbar\omega \left(n + \frac{3}{2} \right), \tag{2.7}$$

where $n = 0, 1, 2, ...$ Permitted values of l are even when n is even, and odd when n is odd, between $0 \leq l \leq n$ in steps of 2 integers. Each value of l has a degeneracy of $2l + 1$, resulting in a total degeneracy for each value of n of $1/2(n + 1)(n + 2)$ as the energy neither depends on l or m_l, and the total occupancy of each level is given by $2j + 1$.

The neutron single-particle energy levels calculated for ^{208}Pb using the harmonic oscillator potential are shown to the left in Figure 2.4. The total occupancy of each level is indicated in square brackets, along with the cumulative occupancy total. The l and m_l independence is reflected in equally spaced levels, with shell closures appearing at cumulative occupancies of 2, 8, 20, 40, 70, 112 and 168. Although encouraging in some aspects as the reproduction of the lowest magic numbers gives credence to the shell model in general terms, the higher-lying magic numbers are not replicated.

A more realistic description is given by the Woods-Saxon potential,

$$V(r) = \frac{V_0}{1 + exp\left[(r - R)/a\right]}, \tag{2.8}$$

where R is the radius at which $V(r)$ is half its peak value, a is the surface

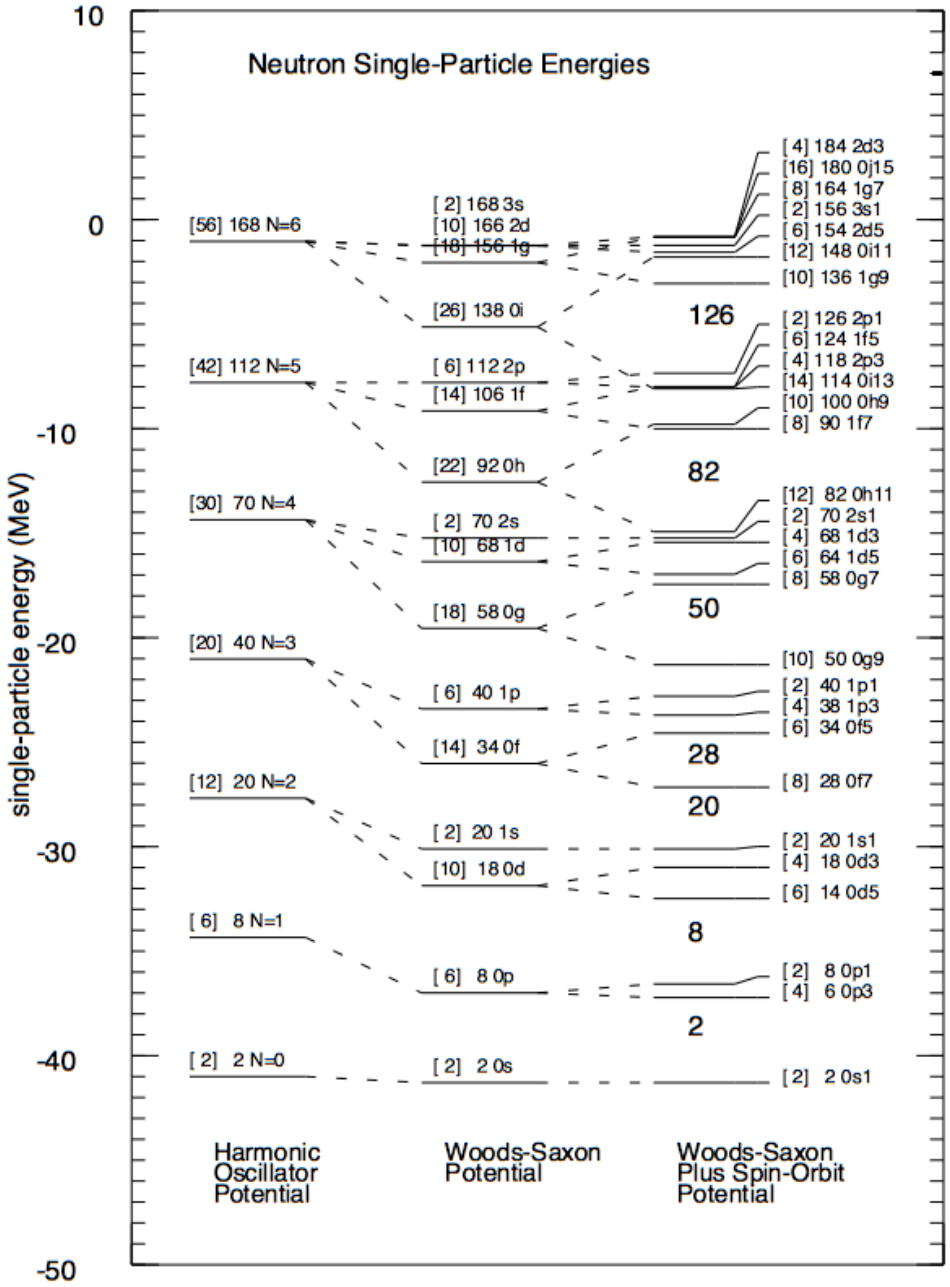

Figure 2.4 Comparison of calculated neutron single-particle energies for ^{208}Pb for the harmonic oscillator, Woods-Saxon and Woods-Saxon plus spin-orbit potentials, taken from [51]. The numbers in square brackets are the total occupancy of the levels. See text for a detailed description.

diffuseness parameter (a measure of the nuclear skin thickness) and

$$V_0 = \left(-51 + 33\frac{\mathrm{N}-\mathrm{Z}}{\mathrm{A}}\right)\mathrm{MeV}. \tag{2.9}$$

Typical values for the parameters in equation 2.8 are $R = 1.2\mathrm{A}^{1/3}$ fm and $a \approx 0.60$ fm. Although the Woods-Saxon potential provides a useful approach to calculating single-particle energies, it is a one-body potential so cannot be used for calculating total binding energies, where two- and many-body interactions must be considered. Neutron single-particle energy levels calculated with the Woods-Saxon potential are shown in the centre of Figure 2.4. The l-degeneracy exhibited by the harmonic oscillator potential is now lifted, but the magic numbers beyond 2, 8 and 20 are still not reproduced.

The introduction of a spin-orbit interaction, almost completely analogous to the spin-orbit interaction in the atomic shell model, by Goeppert-Mayer, and independently by Haxel, Jensen and Suess, allowed the observed magic numbers to be fully reproduced. In this description, the orbital angular momentum $\mathbf{l}$ and intrinsic spin $\mathbf{s}$ of each nucleon couple together to a total angular momentum $\mathbf{j} = \mathbf{l} + \mathbf{s}$, and $\mathbf{l}$ parallel to $\mathbf{s}$ is favoured. The addition of a term of the form $-V_{SO}(r)\mathbf{l}\cdot\mathbf{s}$, describing the spin-orbit interaction to the nuclear potential, results in an energy splitting for each value of l. From

$$j^2 = l^2 + s^2 + 2\mathbf{l}\cdot\mathbf{s}, \tag{2.10}$$

we see that

$$\langle \mathbf{l}\cdot\mathbf{s}\rangle = \frac{\hbar^2}{2}[j(j+1) - l(l+1) - s(s+1)], \tag{2.11}$$

giving the energy splitting, ΔE, between a level with $j = l + 1/2$ and a level with $j = l - 1/2$ to be

$$\Delta\mathrm{E} = V_{SO}\frac{\hbar^2}{2}(2l+1). \tag{2.12}$$

The calculated neutron single-particle energy levels for a Woods-Saxon plus spin-orbit potential are shown to the right of Figure 2.4, demonstrating the appearance of shell closures at N = 2, 8, 20, 28, 50, 82 and 126, reproducing the magic numbers.

2.1.3 More advanced models

Previous Sections have discussed the basic elements in both macroscopic and microscopic models of nuclear structure. However, beyond very simple nuclear systems, the many-body nature of nuclei warrants more complex potentials and the inclusion of residual interactions in order to describe observed nuclear behaviour. The Woods-Saxon nuclear potential described in Section 2.1.2 is a central potential and hence only describes spherically symmetric nuclei, whereas many nuclei with unfilled shells are non-spherical in their ground states, so the effects of 'deformation' must be considered. For example, the nucleus ^{62}Ga has a filled $f_{7/2}$ shell, which is seen as a ^{56}Ni 'core' in shell model considerations. In this formalism, the three protons and three neutrons outside of the core occupy the $p_{3/2}$ and $f_{5/2}$ orbitals which, in the deformed shell model, corresponds to an expected small prolate deformation [52]. Another limitation of the shell model in its simplest form is that, as nucleons are considered to only interact with the average nuclear potential and not with each other, nuclear states are considered to be isolated, with no interaction between them. However, pairing between nucleons can play an important role in nuclear structure (see Section 2.2.2), and superpositions of nuclear states close in energy, known as 'configuration mixing', must also be taken into account.

Despite many advances in the field of nuclear modelling and the availability of more powerful computing systems, no single model is able to reproduce empirical observations across the enormous range of nuclei that reside in the nuclear landscape. Experimental results such as those presented in this thesis are therefore absolutely key in order to not only test the predictive properties of the various models, but also to provide input parameters to tune them. Although it is a comparison of the results of the different nuclear models that are of interest in this thesis work, it is nevertheless important to have a qualitative understanding of the major features of each to allow interpretation of results.

2.1.3.1 Deformed shell model

In general terms, the surface of a deformed nucleus can be described by the 'effective radius', R, which is the distance from the centre to the surface at angles θ and ϕ [53]:

$$\mathrm{R}(\theta,\phi) = \mathrm{R}_{av}\left[1 + \sum_{\lambda=0}^{\alpha}\sum_{\mu=-\lambda}^{+\lambda}\alpha_{\lambda\mu}Y_{\lambda\mu}(\theta,\phi)\right], \tag{2.13}$$

where R_{av} is the average nuclear radius and $\alpha_{\lambda\mu}$ are coefficients for the spherical harmonics $Y_{\lambda\mu}$. A value of $\lambda = 0$ describes a spherically symmetric system and $\lambda = 1$ describes a translational displacement. Values of $\lambda = 2, 3, ...$ describe quadrupole deformation, octupole deformation and so on. In most instances the $\lambda = 2$ quadrupole term dominates terms of higher order, resulting in a spheroid shape, giving

$$\mathrm{R}(\theta,\phi) = \mathrm{R}_{av}\left[1 + \beta_2 Y_{20}(\theta,\phi)\right]. \tag{2.14}$$

The 'deformation parameter', $\beta_2 = \alpha_{20}$, is given by

$$\beta_2 = \frac{4}{3}\sqrt{\frac{\pi}{5}}\frac{\Delta\mathrm{R}}{\mathrm{R}_{av}}, \tag{2.15}$$

where ΔR is the difference between the semimajor axis (in the equatorial plane) and semiminor axis (in the polar plane). Positive and negative values of β_2 correspond to prolate and oblate ellipsoid shapes, respectively.

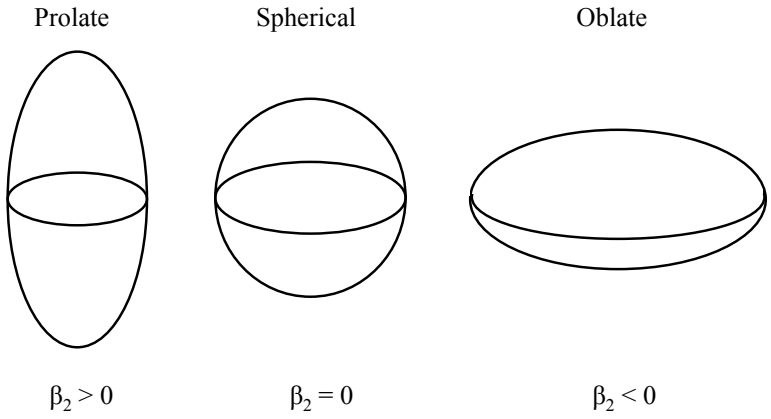

Figure 2.5 Ellipsoidal nuclear shapes.

The shell model was first generalised to include deformation in 1955 by S. Nilsson.

In this formalism, the single-particle Hamiltonian H is given by

$$\mathrm{H} = \mathrm{H}_0 - \mathrm{C}\mathbf{l}\cdot\mathbf{s} - \mathrm{D}\mathbf{l}^2, \tag{2.16}$$

where C and D are empirically determined constants, and H_0 is the Hamiltonian for a modified anisotropic harmonic oscillator given by

$$\mathrm{H}_0 = \frac{-\hbar^2}{2m}\nabla^2 + \frac{1}{2}m\left(\omega_x^2 x^2 + \omega_y^2 y^2 + \omega_z^2 z^2\right), \tag{2.17}$$

where ω_i are the oscillation frequencies in each dimension, analogous to the oscillation frequency ω in the simple harmonic oscillator potential given in equation 2.6. The $\mathbf{l}\cdot\mathbf{s}$ term in the Hamiltonian describes the spin-orbit coupling discussed in Section 2.1.2. The additional $\mathbf{l}^2$ term accounts for nucleons with larger $\mathbf{l}$, which tend to be at larger distances from the centre of the nucleus and therefore experience in reality a deeper potential than that described by the harmonic oscillator.

Conservation of the nuclear volume due to the incompressibility of nuclear matter then dictates that $\omega_x\omega_y\omega_z = \overline{\omega}_0^3$ is constant. For a nucleus symmetric about the z-axis,

$$\omega_x^2 = \omega_y^2 = \omega_0^2\left(1 + \frac{2}{3}\epsilon\right), \tag{2.18}$$

$$\omega_z^2 = \omega_0^2\left(1 - \frac{4}{3}\epsilon\right). \tag{2.19}$$

The parameter ϵ is directly proportional to the deformation parameter β_2.

More recent adaptations of the deformed shell model, met with success describing nuclei with A $\sim$ 60 and $\sim$ 80, include configuration mixing, and are based on self-consistent Hartree-Fock calculations [32, 54, 55]. The Hartree-Fock method is an ab initio approach to solving the Schrödinger equation for many-body Hamiltonians, where an initial approximation to the many-body wavefunction is based on antisymmetrised products of single-particle wavefunctions ('Slater determinants'). A variational approach is then used to obtain the true form of the wavefunction, in which the energy is minimised.

2.1.3.2 Interacting boson model

The Interacting Boson Model (IBM), sometimes known as the Independent Boson Approximation (IBA), was developed in its initial form by A. Arima and F. Iachello in 1975 [56], and has been met with success describing low-lying states in medium and heavy nuclei. Based upon a basic shell model formalism, the IBM assumes that valence nucleons couple to form pairs with total angular momentum $J = 0$ or 2, referred to as s and d bosons, respectively. Each valence boson then interacts with an inert core, usually taken to be ^{56}Ni in calculations for nuclei with $56 \leq A \leq 78$. The properties of collective low-lying states are then attributed to the single-particle boson states.

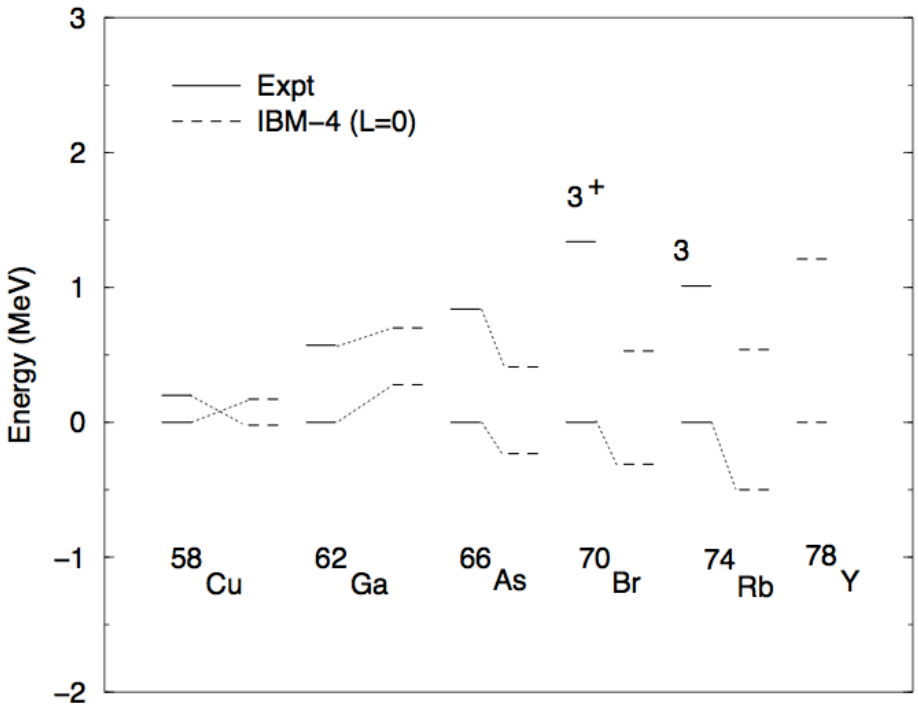

Figure 2.6 Experimentally determined lowest-lying T=0 and T=1 levels in odd-odd N=Z nuclei, compared with IBM-4 calculations, taken from [57].

The first versions of the IBM assumed absolute isospin symmetry, in that no distinction was made between neutrons and protons, and was limited to even-even nuclei only. The next iteration of the model, IBM-2, incorporates some aspects of isospin symmetry-breaking as bosons composed of nn pairs and pp pairs are considered distinctively. In more recent forms, the IBM-3 and IBM-4, all nucleon pairing configurations are included. Whereas IBM-3 and IBM-4 include T = 1 pairs with $T_z = 0, \pm 1$, IBM-4 also considers T = 0 pairs, allowing predictions of the competition between T = 0 and T = 1 pairings (see Section 2.2

for a full description of isospin). The experimentally determined energies of the first T=1 and T=0 states in odd-odd self-conjugate nuclei with mass 58 to 78 are compared with energies calculated using the IBM-4 in Figure 2.6.

2.2 Isospin

The indiscriminate treatment of protons and neutrons in many aspects of nuclear structure is based on the approximation that the strong interaction is both charge symmetric and charge independent, implying that the force between any combination of two nucleons is identical. This fundamental symmetry is violated by electromagnetic interactions and the small mass difference between up- and down-quarks, but has powerful implications in nuclear structure considerations nonetheless. The concept of isospin allows the neutron and proton to be considered different states of a single particle known as the nucleon, which are degenerate in the absence of electromagnetic interactions and small nuclear isospin-breaking effects. In this formalism, the nucleon has an 'isospin' quantum number $t = 1/2$, analogous to the intrinsic spin quantum number s for fermions. The two types of nucleon are then distinguishable by differing values of the projection of the isospin vector $t_z = m_t\hbar$, where $m_t = -1/2$ for protons and $m_t = +1/2$ for neutrons. In multi-nucleon systems the t_z of individual nucleons couple together to form a total isospin projection T_z, given by the following:

$$\mathrm{T}_z = \frac{1}{2}(\mathrm{N} - \mathrm{Z}). \tag{2.20}$$

The total isospin of the system, T, takes values between $|\mathrm{N}-\mathrm{Z}|/2$ and $(\mathrm{N}+\mathrm{Z})/2$ in integer steps.

Assuming that the strong interaction is both charge independent and charge symmetric then, if Coulomb effects are neglected, isobaric nuclei with identical numbers of nucleons will exhibit almost identical behaviour. Observed differences in nuclear structure between isobaric nuclei therefore provide an opportunity to probe in detail both Coulomb and nuclear isospin-breaking effects, providing a wealth of information regarding the underlying structure.

2.2.1 Isobaric multiplets and Coulomb energy differences

The simplest example of the effects of isospin symmetry is a 2-nucleon system, which has three ways of pairing the nucleons: *nn*, *pp* and *np*. Using equation 2.20, the three configurations will have T_z values of $+1$, -1 and 0, respectively. Nucleon pairings with $T = 0$ and $T = 1$ are referred to as having 'isoscalar' and 'isovector' character, respectively. For pairings between like nucleons, *nn* and *pp*, all states must have $T = +1$ as this is the only accessible value. Isospin symmetry then dictates that identical $T = 1$ states must exist in the *np* configuration. These sets of three states are known as 'isospin triplet states', and any differences observed between the states from the breaking of the isospin symmetry provide a deep insight into the inner workings of the nucleus. In general, isobaric multiplet states are known as 'isobaric analogue states', or IAS.

Pairs of nuclei with the number of constituent neutrons and protons interchanged are called 'mirror nuclei'. The power of isospin symmetry is particularly evident in these cases as, if Coulomb effects and isospin symmetry-breaking nuclear effects are neglected, the structure of the mirror pair is identical. The example shown in Figure 2.7 shows the experimentally determined low-lying level structure of the mirror nuclei ^{27}Al and ^{27}Si [58]. All states in one mirror have isobaric analogues in the other with almost identical J^π assignments and branching intensities, with very few exceptions.

Differences in energy between isobaric analogue states are referred to as 'Coulomb energy differences', or CED. The CED for an IAS in a mirror pair with excitation energy E and total angular momentum J, known as the 'mirror energy difference', or MED, is given by

$$\mathrm{MED_J} = \mathrm{E_{J,Z>N}} - \mathrm{E_{J,Z<N}}. \tag{2.21}$$

The CED for isobaric triplet states, or TED, with $T = 1$ and $T_z = 0, \pm 1$, is defined as the following:

$$\mathrm{TED_J} = \mathrm{E_{J,T_z=-1}} + \mathrm{E_{J,T_z=+1}} - 2\mathrm{E_{J,T_z=0}}. \tag{2.22}$$

It is important to note that the excitation energy of an IAS in these considerations is calculated with respect to the ground state energy, as isospin symmetry breaking is also manifested in differences between binding energies of isobaric multiplets. Ground state binding energy differences can be largely attributed to Coulomb effects, but the same cannot be said for energy differences between

Figure 2.7 Level schemes for the A = 27 mirror nuclei ^{27}Al (a) and ^{27}Si (b), taken from [58].

higher-lying IAS as such effects are mainly cancelled out through calculating excitation energy with respect to the ground state. The study of higher-lying CEDs in isobaric multiplets consequently provides an opportunity to probe isospin symmetry-breaking from the strong force, and subtle aspects of nuclear structure.

2.2.2 Pairing correlations in N = Z nuclei

Nuclei with N = Z provide a unique environment in which to study possible *np* pairing behaviour as neutrons and protons occupy the same orbitals and the Fermi surfaces are close in energy (although it is worth noting that an energy gap of several MeV between neutron and proton Fermi surfaces are present due to Coulomb interactions). Although isospin symmetry requires that isovector (T = 1) *np* pairings must exist, it remains an open question as to whether isoscalar T = 0 pairings also play a part [59].

Consider an even-even nucleus $^{A-2}_{Z-1}X_1$, where N = Z. If all of the like nucleons couple together to form pure T = 0 pairs, the ground state can be thought of as a 'condensate' of deuterons. The effect on the binding energy of the system through

the addition of an *np* pair to form the odd-odd N = Z nucleus ${}^{\mathrm{A}}_{\mathrm{Z}}\mathrm{X}_2$ can provide information regarding the nature of the pairing correlations present [60]. If the additional *np* pair is coupled to T = 0, it will behave similarly to the even-even 'condensate' core, resulting in a binding energy B (OO) that is approximately the average between the two even-even neighbours, ${}^{\mathrm{A-2}}_{\mathrm{Z-1}}\mathrm{X}_1$ and ${}^{\mathrm{A+2}}_{\mathrm{Z+1}}\mathrm{X}_3$, denoted B_{av} (EE). If the additional *np* pair is coupled to T = 1, however, a reduction in the binding energy of ${}^{\mathrm{A}}_{\mathrm{Z}}\mathrm{X}_2$ compared to the average between the two even-even neighbours would be observed. This difference in binding energy is known as the 'pair gap', Δ, and is given by:

$$\mathrm{B}_{av}\,(\mathrm{EE}) - \mathrm{B}\,(\mathrm{OO}) \approx \Delta_n + \Delta_p \approx 2\Delta. \tag{2.23}$$

The reverse argument is equally applicable: if the even-even core behaves as a condensate with T = 1 pairings, then a pair gap of 0 or 2Δ would arise if the *np* in the odd-odd system coupled to T = 1 or T = 0, respectively. If we consider a system where neither pure T = 0 nor T = 1 pairings constitute the even-even core, states that couple to both T = 0 and T = 1 in the odd-odd system will have binding energies with no observed pair gap.

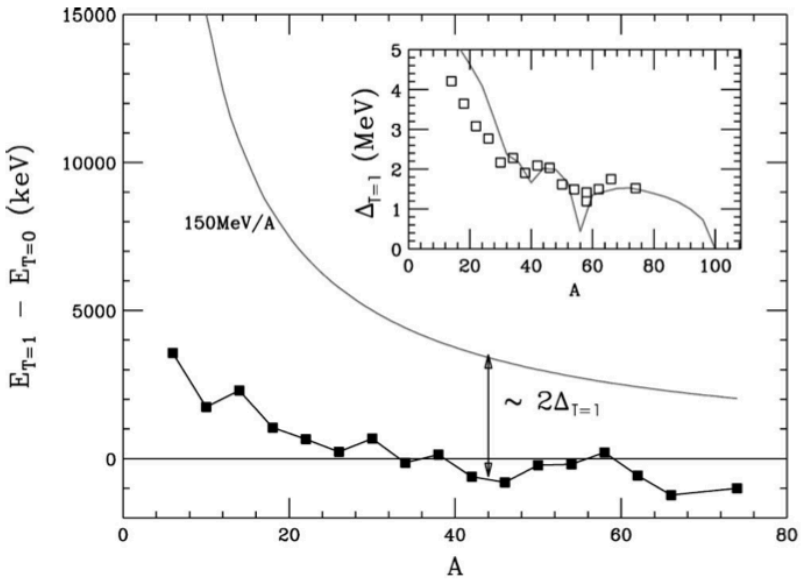

Figure 2.8 Energy differences between T = 0 and T = 1 states in odd-odd N = Z nuclei, taken from [59].

Evidence supporting the existence of pairing effects is given in Figure 2.8, which shows the experimentally determined difference in energy between the lowest-lying T = 0 and T = 1 states for odd-odd N = Z nuclei. The solid line indicates

the predicted differences if no pairing effects are present, suggesting that the lowest-lying T = 0 state should always be lower in energy that the first T = 1 state. It has been observed, however, that all self-conjugate odd-odd nuclei with A > 40 have T = 1 ground states, with the exception of ^{58}Cu. It is clear, therefore, that additional phenomena must be considered in order to explain the observed energy differences. It has been suggested that the experimental values can be explained if only T = 1 pairing is dominant, as states with T = 0 pairing would then 'block' the condensate behaviour, resulting in a reduction in binding energy and effectively pushing the energy of T = 0 states up [59]. The pair gap for T = 1, 2Δ, has a known $1/A^{1/2}$ dependence [61], which when subtracted from the pairing-independent prediction reproduces the experimental values well. The reversal of behaviour at ^{58}Cu can be attributed to the configuration of a single *np* pair more than the shell closure at N = Z = 28. In order to develop understanding of the competition between *np* pairs of isoscalar and isovector character in self-conjugate odd-odd nuclei, good knowledge of the low-lying T = 0 and T = 1 states is essential.

2.3 γ decay

Any nucleus in an excited state can de-excite by emitting γ radiation. In principle, this decay mechanism is always open, but in practice the transition probabilities vary widely, and are affected by properties of the initial and final states. Through consideration of conservation of energy and momentum, the difference in energy between the initial and final states, ΔE, is given by

$$\Delta E = E_\gamma + E_R, \tag{2.24}$$

where E_γ is the energy of the γ ray and E_R is the kinetic energy of the recoiling nucleus after de-excitation given by

$$E_R = \frac{E_\gamma^2}{2Mc^2}, \tag{2.25}$$

for a nucleus with mass M. Observed γ radiation is detected at discrete energies (within experimental limitation), as E_γ is governed by the excitation energies of the nuclear states, which remain fixed. Additional information regarding the nuclear states can be obtained through consideration of the decay selection rules, angular distribution measurements, and lifetime measurements. Consequently,

the measurement of γ radiation has long been used as a means to probe properties of the states within the nucleus.

2.3.1 γ-decay selection rules

The selection rules for γ decay can be constructed through conservation of total angular momentum and parity. Although similar in some respects to the construction of the β-decay selection rules (see Section 2.4.1), a key difference in this case is that γ-ray photons have an intrinsic spin of 1, so the total angular momentum associated with the γ ray, $\mathbf{L}$, must be at least 1. Accordingly, the following relation must hold:

$$\mathbf{J}_\mathrm{i} = \mathbf{J}_\mathrm{f} + \mathbf{L}, \tag{2.26}$$

where $\mathbf{J}_\mathrm{i}$ and $\mathbf{J}_\mathrm{f}$ are the angular momentum of the initial and final states, respectively. Consequently, L can take the following values in integer steps:

$$|\mathrm{J}_i - \mathrm{J}_f| \leq \mathrm{L} \leq \mathrm{J}_i + \mathrm{J}_f. \tag{2.27}$$

The value of L is referred to as the 'multipolarity' of the radiation, where $\mathrm{L} = 1, 2, 3...$ refers to dipole, quadrupole, octupole... and so on.

Radiation with multipolarity L is denoted EL or ML for electric and magnetic type, respectively. As the parity associated with each type of radiation is given by $\pi(\mathrm{ML}) = (-1)^{\mathrm{L}+1}$ and $\pi(\mathrm{EL}) = (-1)^{\mathrm{L}}$, transitions between initial and final states with the same parity must be composed of even electric and odd magnetic multipoles. Conversely, if a parity change exists between initial and final states, the transition must be composed of odd electric and even magnetic multipoles.

In some cases transitions are of a 'pure' multipolarity. One example of this is a transition from a 2^+ initial state to a 0^+ final state, then from equation 2.27 we see that $\mathrm{L} = 2$, and with no parity change we have radiation of pure E2 character. Many cases, however, have transitions with mixed character. In general, the lowest allowed multipolarity dominates as decay probabilities rapidly decrease with increasing values of L. However, the decay probability of electric radiation is $\sim 10^2$ times larger than magnetic radiation of the same multipolarity [62].

2.3.2 Anisotropy in γ decay

Information regarding the multipolarity of a γ-ray transition can be obtained through analysis of changes in intensity measured at different angles with respect to the decay angle. In order to observe anisotropy in γ decay the spins of the nuclei must be aligned, as decays observed from a collection of randomly oriented nuclei would appear isotropic. This is achieved in fusion-evaporation reactions as the spins of the recoiling nuclei are aligned (to a good approximation) perpendicularly to the beam direction. The intensity of a transition at a given angle with respect to the beam axis, $\mathrm{W}(\theta)$, can then be given by

$$\mathrm{W}(\theta) = \sum_{\mathrm{k}} \mathrm{A_k P_k} \cos(\theta), \tag{2.28}$$

where $\mathrm{P_k} \cos(\theta)$ are Legendré polynomials and $\mathrm{A_k}$ are angular distribution coefficents. The integer k takes even values up to $2\mathrm{l}_\gamma$, where l_γ is the angular momentum of the emitted γ ray. The coefficients $\mathrm{A_k}$ depend on the spins of the initial and final nuclear states, and the m (magnetic substate) population distribution.

γ decays with dipole or quadrupole character dominate those of higher multipolarity. Equation 2.28 then takes the form

$$\mathrm{W}(\theta) = 1 + \mathrm{A_2 P_2} \cos(\theta) + \mathrm{A_4 P_4} \cos(\theta). \tag{2.29}$$

When a sufficient level of statistics is available for a given transition, a full analysis of intensity changes across different detector angles can be performed, and the coefficients $\mathrm{A_2}$ and $\mathrm{A_4}$ extracted through performing fits to the empirical data. If the level of statistics is too low, or there is a high density of γ rays in the energy region of interest, angular correlations can be used in place of full angular distributions. One such method is Directional Correlations of Oriented states (DCOs), where requiring coincidence with a transition of known multipolarity (usually E2) can provide much cleaner γ-ray spectra for detectors at two different angles. A ratio of intensity for a given transition measured at the two angles (both with the same coincidence requirement) then provides information regarding the multipolarity of the transition. For very low levels of statistics, a ratio of intensity for a given photopeak between detectors at very forward angles with respect to the beam and detectors at ninety degrees can provide the means to discriminate between radiation of different character.

2.4 β decay

The term 'β decay' is generally used to describe three nuclear decay processes, in which nuclei transmute towards the valley of stability without any change in the number of nucleons, A. This nuclear transmutation occurs through the capture of an atomic electron by a proton in the nucleus, referred to as 'electron capture', or through the conversion of a single nucleon of one type into a single nucleon of the other. Conservation of charge and lepton number dictates that additional particles must be involved in all of the β-decay processes. The decay mechanism

$$\mathrm{n} \rightarrow \mathrm{p} + \mathrm{e}^{-} + \bar{\nu}_e \tag{2.30}$$

is referred to as β^- decay, as the conversion of a neutron into a proton results in the emission of an electron and an electron antineutrino, $\bar{\nu}_e$. Conversely, the decay mechanism

$$\mathrm{p} \rightarrow \mathrm{n} + \mathrm{e}^{+} + \nu_e \tag{2.31}$$

is referred to as β^+ decay, as a positron and electron neutrino, ν_e are emitted. The electron capture mechanism is described by

$$\mathrm{p} + \mathrm{e}^{-} \rightarrow \mathrm{n} + \nu_e. \tag{2.32}$$

In the context of this thesis, the term 'β decay' refers either of the β^-- or β^+-decay processes.

Figure 2.9 shows the form of the momentum distribution for β particles emitted during β decay. The continuous energy distribution was somewhat alarming for nuclear physicists at the time of discovery, as previously observed γ and α radiation had been detected at discrete energies, calling for entirely new phenomena beyond the limits of their understanding. It was Wolfgang Pauli who first postulated the existence of the neutrino, a weakly interacting neutral particle with half-integer spin, which is emitted in all β-decay processes. Neutrinos were impossible to detect with the limitations of experimental equipment at the time of the first β-decay observations, and direct observation was not reported until more than 20 years later. The continuous energy distribution of β particles emitted in β-decay processes is then attributed to the emission of a pair of leptons, which 'share' the available energy in the decay. The electron (or positron) can be emitted with any energy from 0 up to the total amount of accessible energy, or

'end-point', given by the decay Q-value:

$$\mathrm{Q}_{\beta^-} = [\mathrm{M_P} - \mathrm{M_D}]\, c^2, \tag{2.33}$$

$$\mathrm{Q}_{\beta^+} = [\mathrm{M_P} - \mathrm{M_D} - 2\mathrm{m_e}]\, c^2, \tag{2.34}$$

where $\mathrm{m_e}$ is the mass of the electron, and $\mathrm{M_P}$ and $\mathrm{M_D}$ are the atomic masses of the parent and daughter nuclei, respectively.

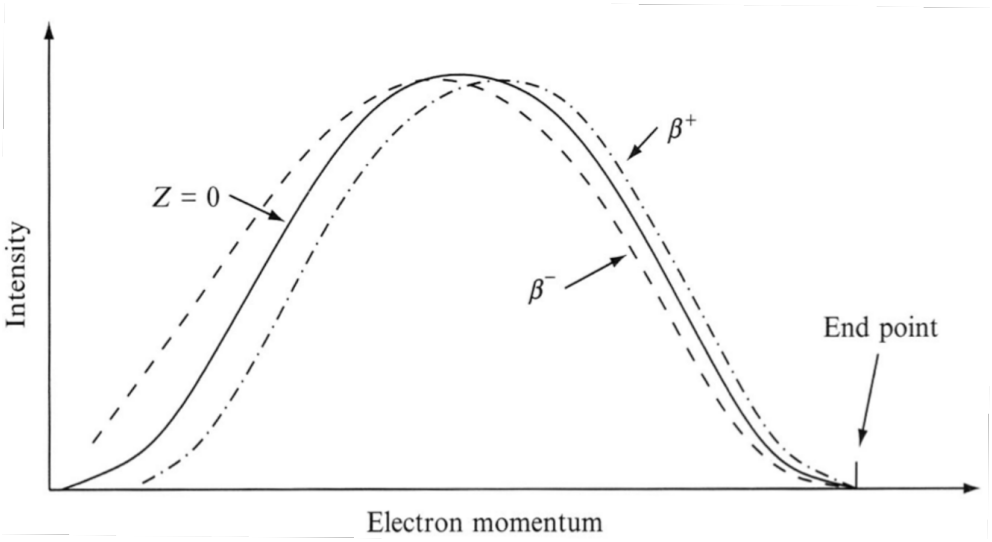

Figure 2.9 Schematic momentum distribution for β decay [63]. Differences in the distribution between β^- and β^+ are due to Coulomb interactions.

The transition rate for β decay between an initial state i and final state f, λ, is given by Fermi's Golden Rule [62, 64], which states that

$$\lambda = \frac{2\pi}{\hbar} |M_{\mathrm{fi}}|^2 \frac{\mathrm{dn}}{\mathrm{dE}}, \tag{2.35}$$

where M_{fi} is the nuclear matrix element, equal to the integral of the interaction between the initial and final states, and dn/dE is the density of final states.

Instead of using the decay half-life, $t_{1/2}$, as a basis of comparison between decay probabilities of nuclei, it is useful to introduce the 'comparative half-life', $ft_{1/2}$. The 'Fermi integral', f, is a dimensionless quantity given by [62]

$$f\left(\mathrm{Z}', \mathrm{E}_0\right) = \kappa \int_0^{p_{max}} F\left(\mathrm{Z}', p\right) p^2 \left(\mathrm{E}_0 - \mathrm{E_e}\right)^2 \mathrm{d}p, \tag{2.36}$$

where κ is a constant, $\mathrm{E_e}$ and p are the kinetic energy and momentum of the

electron (or positron), respectively, and E_0 is the decay end-point. The 'Fermi function', $F(\mathrm{Z}', p)$, where Z' is the atomic number of the daughter nucleus, serves to correct for Coulomb interactions between the electron (or positron) with the atomic nucleus. The factor of $p^2 (\mathrm{E}_0 - \mathrm{E}_\mathrm{e})^2$ is a statistical representation of the density of final states.

The dependency of the decay rate on E_0 and Z' are incorporated into the Fermi integral, numerical values of which have been tabulated. The comparative half-life then gives a measure of changes in the nuclear matrix element, M_{fi}, in the following way [62]:

$$ft_{1/2} \propto \frac{1}{|M_{fi}|^2}. \tag{2.37}$$

As values of $ft_{1/2}$ vary across many orders of magnitude, it is customary to use $\log_{10} ft_{1/2}$. For Gamow-Teller transitions, which are described in the following Section, an important quantity is the β-decay 'strength' for a given energy level in the daughter nucleus, B(GT), which is given by [65]

$$\mathrm{B(GT)} = \frac{K \mathrm{I}_\beta}{ft_{1/2}}, \tag{2.38}$$

where I_β is the branching intensity to the given energy level, $K = 3833$ seconds [66] and the half-life $t_{1/2}$ is in seconds.

2.4.1 β-decay selection rules

Conservation of angular momentum dictates that the difference between the angular momentum of the initial state, denoted $\mathbf{J}_\mathrm{i}$, and the angular momentum of the final state, $\mathbf{J}_\mathrm{f}$, must be equal to the total angular momentum of the lepton pair. Additionally, despite the well-known phenomenom of parity violation in β decay, parity must also be conserved when considering selection rules between nuclear states. If the lepton pair, each with intrinsic half-integer spin, couple with anti-parallel spins (known as a 'Fermi' transition), the following relation must hold:

$$\mathbf{J}_\mathrm{i} = \mathbf{J}_\mathrm{f} + \mathbf{L}, \tag{2.39}$$

where $\mathbf{L}$ is the orbital angular momentum carried by the lepton pair. Conversely, if the lepton pair couple with parallel spins (known as 'Gamow-Teller' transitions), then

$$\mathbf{J}_\mathrm{i} = \mathbf{J}_\mathrm{f} + \mathbf{L} + \mathbf{1}. \tag{2.40}$$

For an 'allowed' β decay, the lepton pair carry no orbital angular momentum, and as the parity associated with L is given by $(-1)^L$, there can be no parity change between nuclear states. 'Forbidden' decays are also possible, despite what the nomenclature may suggest, but are less likely to occur than allowed decays. Decays where the lepton pair carry orbital angular momenta $L = 1, 2, 3...$ are referred to as first, second and third forbidden transitions, and become increasingly less probable to occur. Parity changes between nuclear states will occur if L is odd.

'Superallowed' transitions can occur if the wavefunctions of the initial and final nuclear states are very similar, resulting in a matrix element close to 1. One such example is transitions between isobaric analogue states, which are discussed in previous Sections. Superallowed transitions are characterised by very low $\log_{10} ft_{1/2}$ values of ~ 3.5, whereas allowed and first forbidden transitions have $\log_{10} ft_{1/2}$ values of ~ 5.5 and ~ 7.5, respectively. Recently, the lowest ever recorded $\log_{10} ft_{1/2}$ value of $2.62^{+0.13}_{-0.11}$ was observed in the β^+ decay from the doubly-magic nucleus ^{100}Sn [18].

Chapter 3

Previous experimental and theoretical studies of ^{62}Ga

As the results presented in this thesis work include structure information not observed in any previous experimental work, it is important to discuss the differences between the techniques used in previous studies in order to understand how differences in results may arise. This Chapter describes all previous in-beam γ-ray studies of ^{62}Ga. A study of the β decay of ^{62}Ge is also discussed, as well as selected relevant theoretical studies of ^{62}Ga.

3.1 In-beam γ-ray studies of ^{62}Ga

G. de Angelis et al., Nuclear Physics A 630, 426 (1998)

The first in-beam γ-ray measurements of transitions in ^{62}Ga were carried out at the Legnaro National Laboratory (LNL) in 1998 [42]. A beam of ^{32}S, accelerated to 140 MeV using the Tandem XTU at LNL, was incident on an enriched ^{40}Ca target of thickness 0.5 mg/cm^2. ^{62}Ga nuclei were produced in the 2αpn evaporation channel in heavy-ion fusion-evaporation reactions. Prompt γ rays were detected using the GASP detector array, consisting of 40 Compton suppressed HPGe detectors and 80 BGO detectors [67]. Selection of reaction residues was achieved through the use of ISIS, a 4π charged-particle detector consisting of 40 ΔE $-$ E telescopes, with each positioned in front of one of the 40

HPGe detectors that constitute the GASP array. For details of the ISIS-GASP coupling, please see reference [68]. Selectivity on the nucleus ^{62}Ga was achieved in offline analysis through selecting events where γ rays were measured by the GASP array in coincidence with two α particles and a proton detected by ISIS. A $\gamma\gamma$ matrix was then constructed using γ events measured in coincidence with the detection of the desired evaporation residues. Although recoil selection was carried out offline, the hardware trigger required a multiplicity of at least 2 in the HPGe detectors, with the addition of one BGO element.

A coincidence spectrum for ^{62}Ga is shown in Figure 3.1, created by summing γ spectra measured in coincidence with the 246 and 376 keV transitions. Transitions at 246, 376, 571, 946, 1108, 1180, 1241 and 2355 keV were identified, although neither a level scheme nor any spin-parity assignments were proposed.

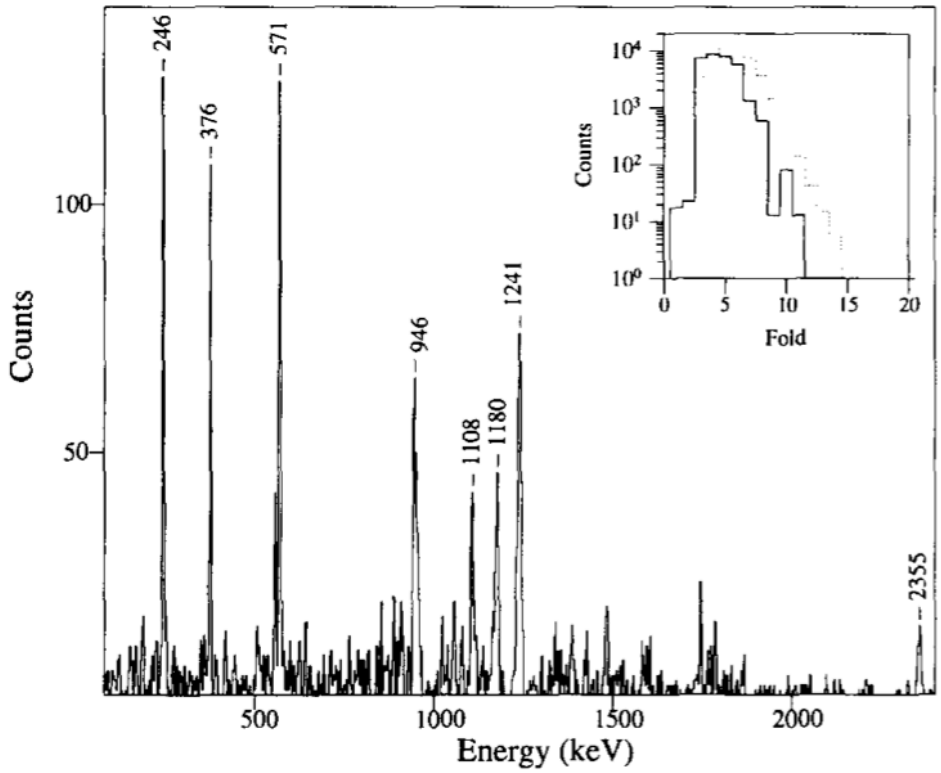

Figure 3.1 Summed coincidence spectrum of γ rays measured by de Angelis *et al.* [42]. See text for details.

S. M. Vincent et al., Physics Letters B 437, 264 (1998)

Shortly after the de Angelis study, the results of two more in-beam γ-ray experiments were published by Vincent *et al.* [43]. The first experiment was

carried out at the Niels Bohr Institute, where a beam of ^{28}Si was accelerated to 88 MeV and collided with a 1 mg/cm^2 target of enriched ^{40}Ca, producing ^{62}Ga in the αpn evaporation channel. The PEX spectrometer [69], an array of 28 Compton suppressed Germanium detector elements, was used to measure in-beam γ rays. As with the de Angelis study, recoil selection was achieved through the use of a spherical Silicon charged-particle detector array surrounding the target. However, an array of neutron detectors at forward angles was also used in this case to provide additional selectivity on evaporation channels involving neutrons. The hardware trigger required at least two coincident γ-ray events measured by the PEX spectrometer, along with signals in both the charged-particle and neutron detectors. A $\gamma\gamma$ matrix, consisting of γ rays emitted in coincidence with evaporated particles corresponding to the production of ^{62}Ga, was created in offline analysis.

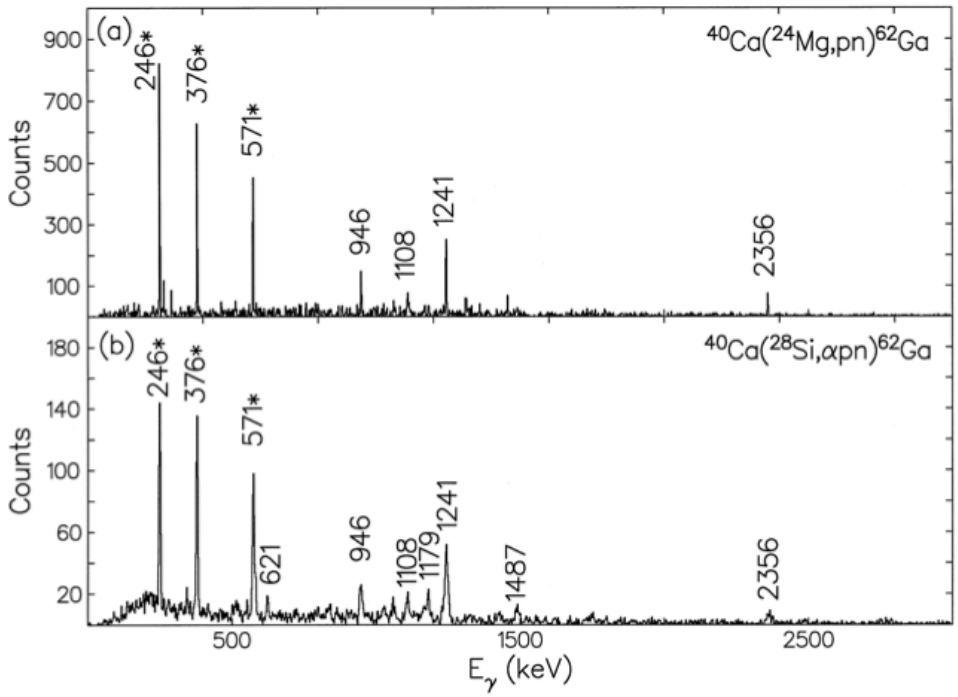

Figure 3.2 Summed coincidence spectrum of γ rays measured by Vincent *et al.* using a) the AYEBALL array and b) the PEX spectrometer [43].

The second experiment was carried out at the Argonne National Laboratory, where a beam of ^{24}Mg ions was accelerated to 65 MeV by the ATLAS accelerator. Two targets of gold-coated ^{nat}Ca were used, with a 20 mg/cm^2 backing on one in order to stop the recoiling reaction products in the target. The other target had a thin 60 μg/cm^2 backing to allow reaction products to pass through into the FMA and allow recoil identification based on mass-to-charge ratio (A/q). ^{62}Ga nuclei

were produced in the pn evaporation channel, with prompt γ rays measured by the AYEBALL detector array [70]. As with the PEX data, events with γ-ray multiplicities of at least 2 were recorded.

In the PEX data, transitions were observed at 246, 376, 571 and 1179 keV in a total projection of the $\gamma\gamma$ matrix. Additional transitions at 621, 946, 1108, 1241, 1487 and 2356 keV were observed when requiring coincidence with either the 246, 376 or 571 keV transitions. The summed coincidence spectra for both the PEX and AYEBALL data are shown in Figure 3.2, with both requiring coincidence with any of the 246, 376 or 571 keV transitions. It is important to note that the levels of selectivity demonstrated by the AYEBALL+FMA configuration were insufficient to identify Z = 31 residues, so coincidences with strong transitions in ^{62}Ga previously identified in the PEX data were required. The results from both experiments are consistent with those reported by de Angelis *et al.*

Statistics from the two experiments were sufficient to deduce some spin and parity assignments on the basis of angular distribution analyses. It was therefore possible to assign the first four T = 0 yrast states, as well as provide tentative information regarding the excitation energies of three higher-lying yrast states and two non-yrast states, all with T = 0. The 3^+ yrast state at 818 keV was found to be isomeric, with a mean life-time of 4.6 ± 1.6 ns. No excited T = 1 states were observed.

D. Rudolph et al., Physical Review C 69, 034309 (2004)

The most extensive investigation of the structure of ^{62}Ga prior to the current work was carried out by Rudolph *et al.* in 2004 [31]. The Tandem XTU at LNL was used to accelerate a beam of ^{24}Mg to 60 MeV that bombarded an enriched ^{40}Ca target of thickness 0.5 mg/cm^2. It is worth noting that the reaction used to populate states in ^{62}Ga was the same as for the AYEBALL experiment carried out in the Vincent study, but with a 5 MeV increase in beam energy. The target used by Rudolph *et al.* was isotopically enriched, and was backed with a 7 mg/cm^2 Tantalum foil in order to stop all recoiling reaction products in the target. As with the de Angelis work, the GASP detector array was used to detect prompt γ rays, coupled with the ISIS charged-particle detector to provide selectivity on evaporation channels. Additional recoil selectivity was achieved through six neutron detectors positioned at forward angles. The hardware trigger required one Ge detector plus one BGO and one neutron detector, or two Ge detectors plus

one BGO. Although γ events with single multiplicity were recorded if a coincident signal was measured in the neutron detectors, offline analysis was carried out using $\gamma\gamma$ and $\gamma\gamma\gamma$ coincidence techniques. Spin and parity assignments were deduced from consideration of angular distribution ratios and directional correlations of oriented states (DCOs) [71]. A spherical shell model calculation in $pf_{5/2}g_{9/2}$ space was carried out, assuming a ^{56}Ni closed core, providing predictions of branching ratios corresponding to different spin-parity assignments for several low-lying non-yrast states in ^{62}Ga that have not been unambiguously identified. Branches from the T = 1 and T = 0 2^+ states expected to be at $\sim$ 1 MeV were predicted, as well as branches from a previously unobserved low-lying non-yrast 3^+ state and several higher-lying states.

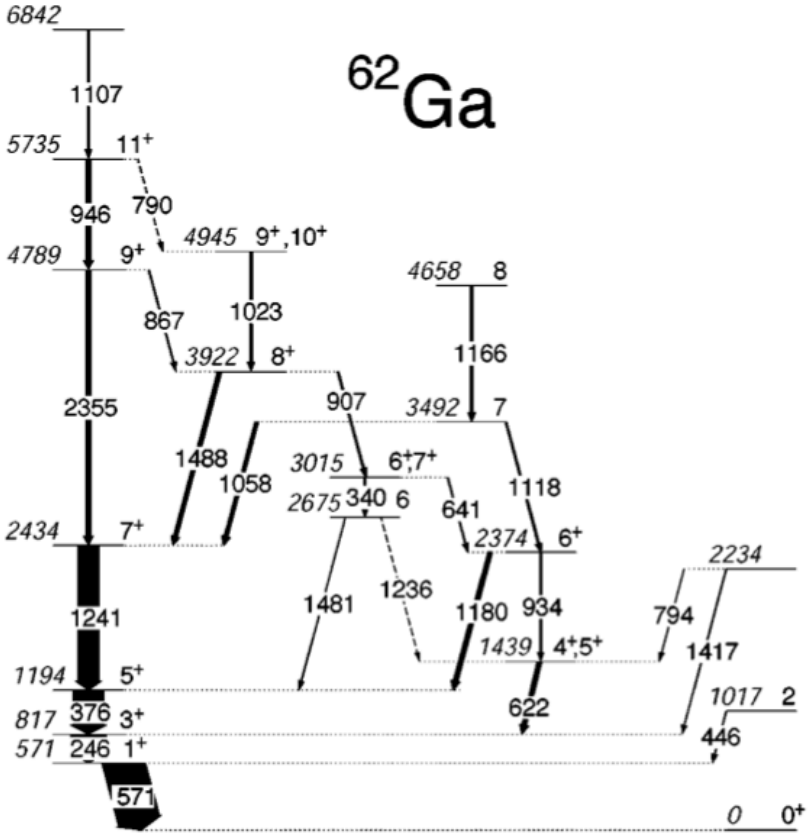

Figure 3.3 Level scheme proposed by Rudolph *et al.* [31]. Candidates for the T = 1 isobaric analogue states of the 2^+ and 4^+ states in ^{62}Zn are shown on the right.

Candidates for the T = 1 2^+ and 4^+ isobaric analogue states were proposed at excitation energies of 1017 and 2234 keV, respectively. As the 2^+ and 4^+ states in ^{62}Zn have been observed at 954 and 2186 keV [72], the proposed states are good candidates when considering excitation energy. Evidence supporting a state at 1017 keV state came in the form of a transition observed at 446 keV

with an anisotropy ratio consistent with $\Delta I = 1$, in coincidence with the 571 keV transition from the first excited 1^+ state to the ground state. However, it is expected that a stretched E2 transition to the T = 1 0^+ ground state from the T = 1 2^+ state should dominate M1 transitions to odd-spin yrast states, which is supported by the results of the shell model calculation [31]. An unsuccessful attempt was made to discern a 1017 keV transition to indicate an E2 transition directly to the ground state as it was found that insufficient cleanliness in particle-gated spectra could be achieved without requiring coincidence with previously identified transitions. The state at 2234 keV was identified by a 1417 keV transition that feeds the yrast 3^+ state at 817 keV, and a 794 keV transition that feeds a state at 1439 keV. Despite large uncertainties, anisotropy ratios measured for the 1417 keV and 794 keV transitions suggested a J = 4 assignment for the state at 2234 keV.

For the T = 1 2^+ state, the branching ratio calculation carried out in the Rudolph study predicted an 81 % branch directly to the 0^+ ground state and a 19 % branch to the yrast T = 0 1^+ state. Another 2^+ state was also predicted at a similar excitation energy, but with T = 0 and not T = 1, with a predicted 87 % branch to the yrast 1^+ state and a weak branch to the T = 1 2^+ isobaric analogue state. Observed branching ratios for the 2234 keV state are equally consistent with a predicted T = 0 4^+ state and the T = 1 4^+ isobaric analogue state. It was not possible in the Rudolph work to confirm whether the states at 1017 and 2234 keV are indeed the T = 1 analogue states.

3.2 β decay of ^{62}Ge

In 2009, a β-decay study of the $T_z = -1$ nucleus ^{62}Ge was carried out at GSI (Gesellschaft für Schwerionenforschung) by E. Grodner *et al.*, and the data presented in a Scientific Report [73]. The GSI heavy-ion synchrotron SIS was used to produce a ∼10 MeV beam of ^{78}Kr ions with an average intensity of 4×10^8 ions per second. ^{62}Ge ions were then produced in the fragmentation of the ^{78}Kr ions when incident on a 4.0 g/cm^2 target of ^{9}Be. Reaction products were selected using the Fragment Separator (FRS) and ancillary detectors [74], allowing mass and charge information to be determined, and were then transported to the RISING array [75–77]. The fully stripped ^{62}Ge ions were stopped in an implantation setup consisting of six 1 mm thick DSSDs, and γ rays were detected using 15 Cluster detectors mounted ∼22 cm from the implantation station [76, 77].

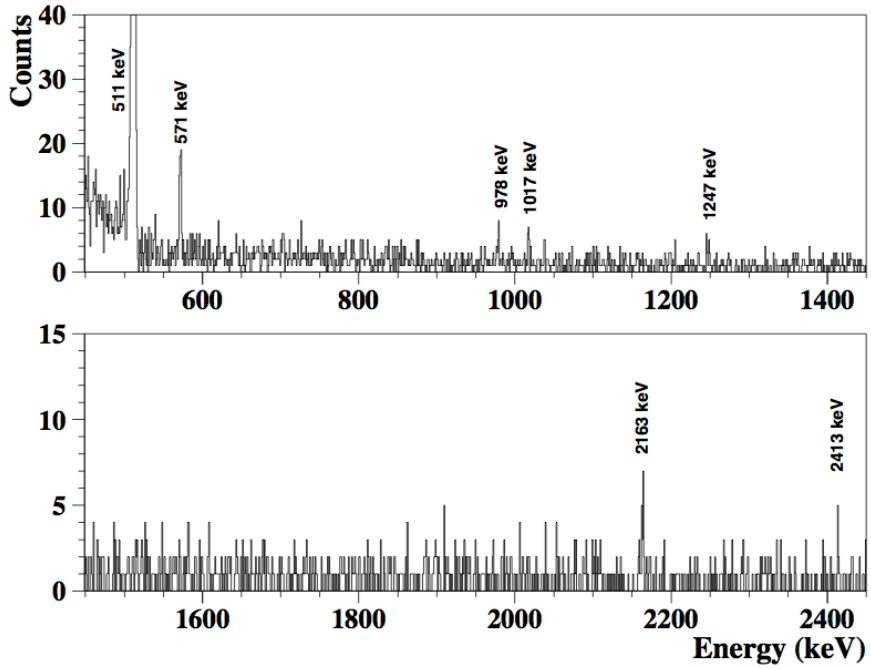

Figure 3.4 Spectrum of γ rays measured by the RISING array in coincidence with β decays following the implantation of ^{62}Ge ions [73].

A lifetime analysis for the β decay of the ^{62}Ge ions was carried out. A 'clean' decay spectrum, without contamination from the β decay of ^{62}Ga, was produced by requiring the observation of two successive decays as only ^{62}Ge exhibits this feature, enabling a lifetime of $\tau = 119.6(20)$ ms to be measured. An analysis of implant-β-γ coincidences (events where implanted reaction products were followed by the observation of a β decay and a γ ray within given time periods) was carried out. Requiring implant-β-γ coincidences enabled a spectrum of γ-ray transitions in ^{62}Ga detected immediately succeeding β decays from ^{62}Ge ions to be made, shown in Figure 3.4. As the ground states of the even-even nucleus ^{62}Ge and the odd-odd N = Z nucleus ^{62}Ga are 0^+, the dominant decay branch is the superallowed Fermi $0^+ \rightarrow 0^+$ β decay. However, allowed Gamow-Teller transitions to 1^+ excited states in ^{62}Ga are also possible with non-negligible branches. Isospin must also be taken into account, as only decays with $\Delta T = 0$ or $\Delta T = 1$ can occur in allowed Gamow-Teller decays. Note that ΔT is the difference in isospin between initial and final states involved in the β decay. Additionally, no parity change between initial and final states can occur in allowed β decays. If allowed β decays to excited states in ^{62}Ga take place, then subsequent de-excitations occur via γ-ray emission. Such de-excitations then form the spectrum shown in Figure 3.4.

A shell model calculation of Gamow-Teller strength distributions for the β decay of ^{62}Ge was carried out by Petermann *et al.* in 2007 [78]. The model space incorporated the entire pf-shell, but neglected the influence of the $g_{9/2}$ orbital.

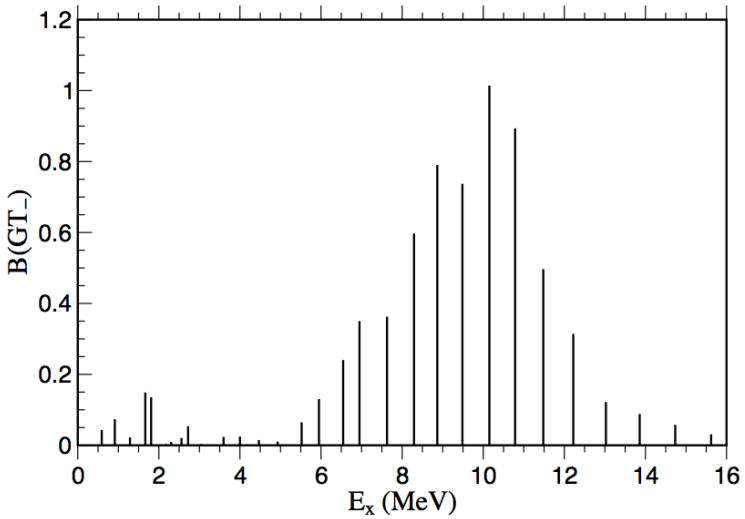

Figure 3.5 Predicted Gamow-Teller strength distribution for β decays of ^{62}Ge [78].

Figure 3.5 shows the predicted Gamow-Teller transition strength distribution for β^+ decays of ^{62}Ge. It can be seen that only a small percentage of the total strength is located in states with excitation energies less than 2 MeV. The first excited 1^+ state at 571 keV is evident, but does not dominate the strength distribution.

3.3 Theoretical calculations

Nuclei with A = 60 − 80 and N ∼ Z have been the subject of much interest for nuclear structure theoreticians over recent decades. Odd-odd nuclei with N = Z have been a particular focus, as understanding neutron-proton (np) pairing effects in such nuclei still remains a challenge. Several attempts to calculate properties of low-lying levels in the odd-odd N = Z nucleus ^{62}Ga have been carried out in the last 15 years, using a range of different nuclear structure models [32, 33, 43, 52, 59]. An overview of a selection of these models, and their theoretical foundations, is given in Section 2.1. Details of selected relevant calculations, for comparison with the experimental results presented in Chapter 6, are given in the following Sections. A compilation of the results is shown in Figure 3.6.

Shell model calculation: S. M. Vincent et al., Physics Letters B 437, 264 (1998)

Experimental results published in a 1998 study by Vincent *et al.* are shown in Section 3.1. In the same study, results of a spherical shell model (SM) calculation were presented to compare with experimental results. The model space used in the calculation consisted of an inert ^{56}Ni core, and the $pf_{5/2}g_{9/2}$ orbits. This configuration was found to produce results in better agreement with experimental results than those calculated using a ^{40}Ca core with the whole pf shell. Once an appropriate model space is chosen, an appropriate effective interaction must also be chosen. The choice of interaction then forms the Hamiltonian, which contains the single-particle energies and two-body matrix elements describing the system. For a comprehensive review of effective interactions in shell model calculations, refer to [79].

A realistic effective interaction introduced by Kuo [80] was used in the Vincent calculation, which was adjusted based on the phenomenology of previous studies of the nuclei ^{76}Ge and ^{82}Se [81]. The two-body interaction matrix elements were then found using 'G matrix' methods, based on realistic nucleon-nucleon scattering, developed by Brueckner in 1955 [82], then later developed further by Goldstone [83] and Bethe, Brandow and Petschek [84]. The results of the calculation, carried out using the shell model code ANTOINE [85, 86], are shown in Figure 3.6. The SM calculation correctly reproduces the observed T = 1 0^+ ground state and T = 0 1^+ first excited state. The energies of the yrast 1^+ and 3^+ states are lower than experimentally observed, but the higher-lying 5^+ and 7^+ energies are well reproduced. Several states with excitation energies of less than 2.5 MeV are predicted, most of which have low spins of 1^+, 2^+ or 3^+.

IBM-4 calculation: O. Juillet, P. Van Isacker and D. D. Warner, Physical Review C 63, 054312 (2001)

In 2001, Juillet *et al.* carried out calculations for the odd-odd N = Z nuclei ^{62}Ga, ^{66}As and ^{70}Br using the isospin invariant interacting boson model (IBM-4), discussed in Section 2.1.3.2, which describes pairs of valence nucleons as 'bosons'. In this formalism, one-body 'boson' energies and two-body 'boson' interactions in the Hamiltonian are determined by mapping two-nucleon states, calculated using the shell model, to boson eigenstates. In the Juillet study, a model space

consisting of a ^{56}Ni inert core and $pf_{5/2}g_{9/2}$ active orbits was used, with a modified Kuo effective interaction [81], as in the shell model calculation by Vincent *et al.* [43]. Results from the IBM-4 calculation for the nucleus ^{62}Ga, treated as a three-boson system, are given in Figure 3.6.

As with the SM calculation by Vincent *et al.*, the T = 1 0^+ ground state and T = 0 1^+ excited state are reproduced in the IBM-4 calculation. The predicted energies of the yrast 1^+ and 3^+ states match the experimental values well. States with spins of greater than 5 cannot be predicted using the IBM-4, however, due to restrictions in the calculation. Several 1^+, 2^+ and 3^+ states are predicted with excitation energies of less than 2.5 MeV.

Deformed shell model calculation: R. Sahu and V. K. B. Kota, Physical Review C 66, 024391 (2002)

As discussed in Section 2.1.3.1, variations of the deformed shell model (DSM) have been used to great effect in recent decades to describe nuclei with A $\sim$ 60 and A $\sim$ 80. In a study by Sahu and Kota in 2002, detailed predictions of the spectroscopy of ^{62}Ga and ^{66}As were presented, calculated using the DSM. The model space and effective interaction used are the same as for the shell model calculation by Vincent *et al.*: an inert ^{56}Ni core with active $2p_{3/2}$, $1f_{5/2}$, $2p_{1/2}$ and $1g_{9/2}$ orbits are assumed, and the effective interaction is a phenomenologically adjusted Kuo interaction taken from reference [81]. Low-lying deformed states were obtained using Hartree-Fock methods. Excited states are subsequently obtained by making particle-hole excitations. For full details of the calculation, refer to [87], [32] and references therein.

Unlike the SM and IBM-4 calculations discussed in earlier Sections, the DSM calculation by Sahu and Kota does not predict a T = 1 0^+ ground state, rather a 1^+ T = 0 ground state is predicted 0.22 MeV below the T = 1 0^+ level. An energy shift of 0.7 MeV is applied to all T = 0 levels, therefore, in order to reproduce the experimental values. It should be noted that the same 0.7 MeV shift applied to DSM calculations for the odd-odd N = Z nucleus ^{66}As predicts an energy of $\sim$ 1 MeV for the first T = 0 excited state, which matches the experimentally determined value of 837 keV well [39]. After the 0.7 MeV shift of T = 0 levels, the predicted yrast 1^+ and 3^+ states have lower energies than experimentally determined, although higher-lying yrast states are reproduced well. Several low-lying low-spin states are predicted.

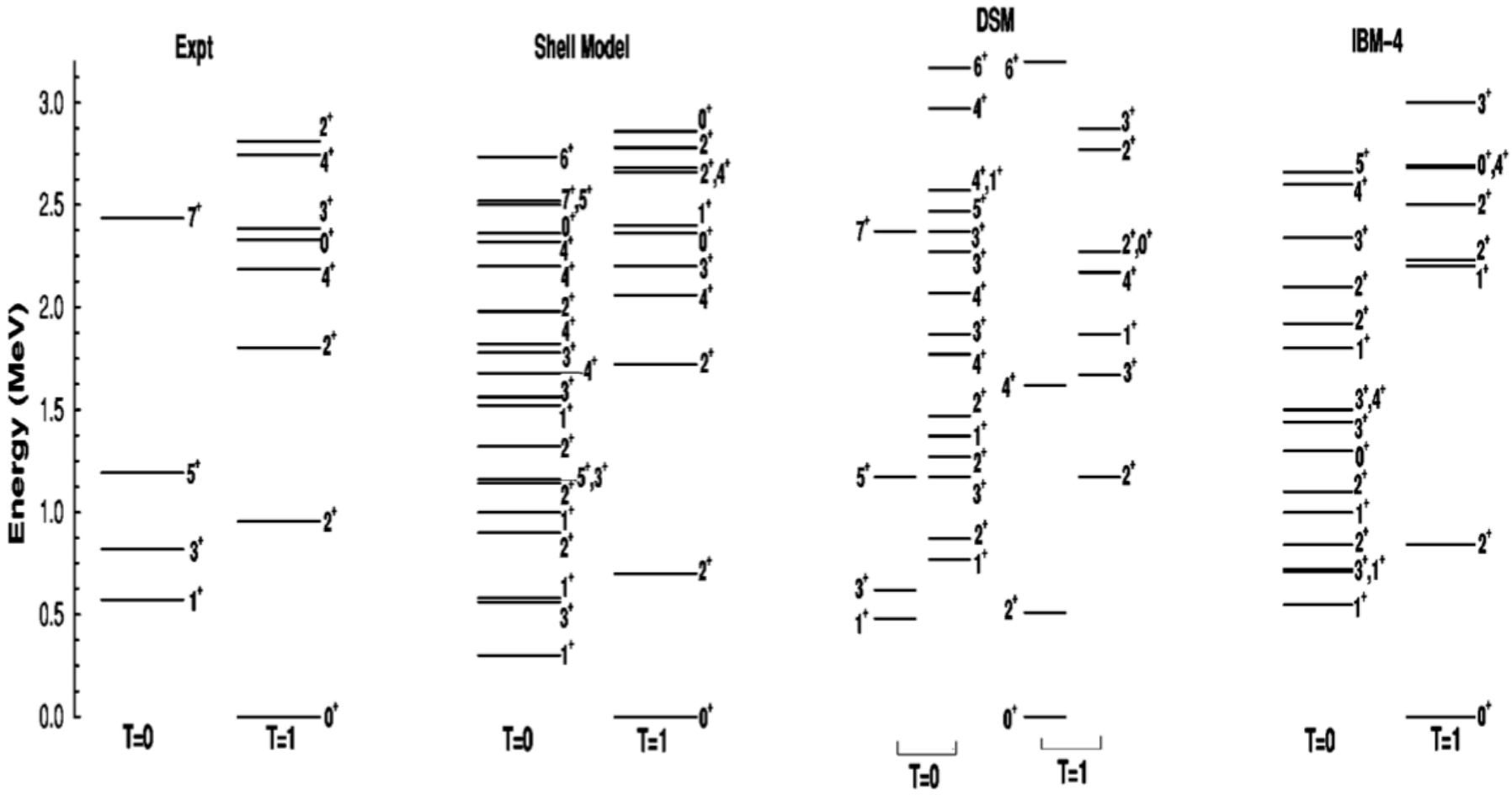

Figure 3.6 Calculated low-lying levels in ^{62}Ga, taken from [32]. Experimentally determined T = 0 levels are taken from the study by Vincent *et al.* [43], and T = 1 levels are taken from the analogue nucleus ^{62}Zn. The experimental data is compared with results from a shell model calculation [43], IBM-4 calculation [33] and a deformed shell model calculation [32].

3.4 Summary of previous experimental and theoretical work

Several in-beam γ-ray studies of the exotic nucleus ^{62}Ga have been carried out in recent decades [31, 42, 43]. The most comprehensive experimental study prior to the current work was carried out by Rudolph *et al.* in 2004, where several T=0 states with excitation energies up to 7 MeV were identified. Candidates for the T=1 isobaric analogue states to the 2^+ state at 954 keV and the 4^+ state at 2186 keV in ^{62}Zn were also proposed but could not be confirmed.

Prior to the current work, ambiguities regarding the low-lying level scheme of ^{62}Ga remained despite significant experimental progress. Additionally, theoretical calculations carried out using the shell model [43], IBM-4 model [33] and deformed shell model [32] predict the existence of many low-lying states with low spin that have not yet been experimentally observed.

Chapter 4

Development of the new method

4.1 Concept and general premise

A number of experimental challenges must be overcome for studies of exotic nuclei with N∼Z due primarily to low production cross-sections coupled with strong contamination from more stable isobaric nuclei. The development of the recoil decay tagging technique in the 1980s provided a dramatic increase in selectivity for nuclei far from stability, and paved the way for 3 decades of successful measurements. Despite this, many cases where characteristic proton, alpha or β-delayed particle decay modes are not exhibited remain a significant challenge to experimentalists. In recent years, the possibility of using β decays to increase selectivity on highly unstable nuclei near the proton drip-line has been realised at the Jyväskylä accelerator laboratory in Finland (JYFL). The technique, referred to as recoil-beta tagging (RBT), was used to identify new transitions in the odd-odd N=Z nuclei ^{78}Y and ^{74}Rb [41, 88].

This Chapter will describe in detail the experimental setup used in recent experiments at ANL where in-beam γ rays of exotic N=Z nuclei were observed using a variation on the RBT technique. The general concept is based upon a large γ-ray detector array coupled with a mass separator, where accelerated beam ions are incident on a target and heavy-ion fusion-evaporation reactions take place. Prompt γ rays are detected by the ∼100 Compton suppressed Ge detectors that constitute the Gammasphere detector array. Recoiling fusion-evaporation reaction products enter the Argonne fragment mass analyzer (FMA)

where they are dispersed by their mass-to-charge ratio (A/q) and pass through a multi-wire proportional counter (PPAC) and ionisation chamber (IC) to provide position, timing and energy loss information. The reaction residues are then implanted into a highly segmented 160×160 double-sided Silicon strip detector (DSSD), where correlations between implanted ions and subsequent β decays can be made. A basic representation of the main constituents of the setup is shown in Figure 4.1.

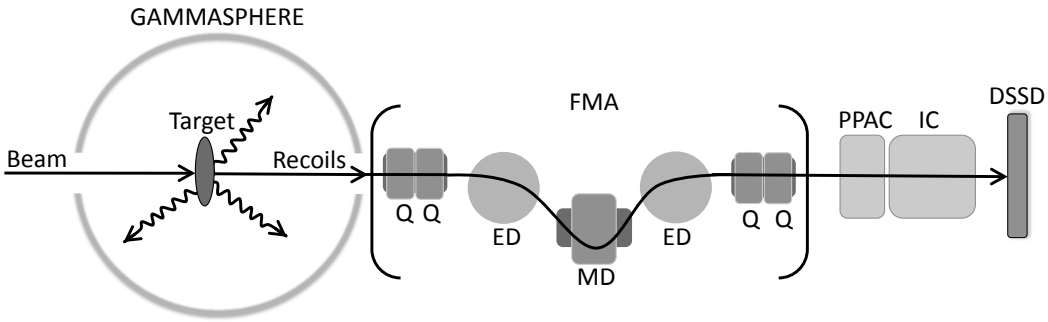

Figure 4.1 Diagram demonstrating the concept of the new system.

The new system described in this thesis work differs in several key aspects to the system developed at JYFL. There exists a fundamental difference between the types of recoil separator used in each case. RITU, the gas-filled separator used at JYFL, provides separation between recoiling reaction products and unreacted beam ions, whereas the FMA used in the current work provides mass-to-charge (A/q) selectivity on recoils. The method of tagging on the positrons themselves is also different. In the JYFL experiment, recoils were implanted into 2 700 μm thick 60 × 40 DSSDs, and a thick planar Ge detector (PGD) located behind the DSSDs was used to stop positrons as they escaped the DSSDs. Correlations between recoils and decays were made using both energy loss in the DSSD from the positrons and the requirement of large energy deposits into the PGDs. This high energy requirement was used to bias the selection towards nuclei that exhibit Fermi superallowed decays, which have characteristically high end-point energies. In the RBT variation described here, the cleanliness of the selection on fast β emitters at the focal plane comes from the very high degree of segmentation in the implantation DSSD. A greater than 5-fold increase in pixels serves to reduce the effective ("per-pixel") implantation rate, and drastically reduces the probability of incorrectly correlating a β decay with the wrong implant.

4.2 Beam and target production

The Argonne tandem-linac accelerator system (ATLAS), a $\sim$ 50 MV superconducting linac for heavy ions, was used to provide beams of ^{40}Ca with energies $94 - 103$ MeV in all of the experimental work that contributes to this thesis. ATLAS can accelerate stable isotopes of any element up to and including Uranium, with energies up to 17 MeV/u. The positive ion injector (PII) is one of two preliminary accelerators that 'inject' beams of ions for acceleration in the main ATLAS linac, and was used in the production of ^{40}Ca. The PII consists of three stages: an electron cyclotron resonance (ECR) plasma ion source, a bunching system to avoid energy spreading in the main linac, and a 12 MV 'injector' linac. In the ECR ion source, a neutral gas is fed into a magnetically confined plasma chamber that is heated by microwave radiation. A rapidly varying E-field, generated by the microwaves, causes free electrons in the chamber to gain energy when the electron gyration frequency ($\omega_g = eB/m_e$, where m_e and e are the mass and charge of an electron, respectively, and B is the magnetic field strength) is matched by the microwave frequency. As the neutral gas atoms are ionised by the energetic free electrons, an avalanche ensues due to the growing number of electrons liberated from the neutral atoms. The ions are extracted from the plasma chamber using a 350 kV platform, where 60-70 % emerge travelling at $\sim$0.009c in beam bunches $\sim$0.25 ns wide. To accelerate them further, the ions are injected into the 12 MV PII-linac, consisting of 18 resonators interspersed with 11 superconducting solenoids to act as focussing elements, where they reach speeds of $\sim$0.06c.

Ions then enter the main linac, which is composed of two sections: the 20 MV 'booster' linac and the 20 MV 'ATLAS' linac. A total of 42 split-ring resonators are used that are phased independently to allow a broad range of velocities and, consequently, beam species to be produced. The drift tubes themselves are made of niobium, an excellent superconductor, whereas the outer housings are made of a niobium-copper composite to allow cooling as niobium is a poor heat conductor. The first 12 resonators are tuned to be synchronous with the ions travelling at a speed of 0.06c as they emerge from the PII, and the remaining 30 resonators are tuned to 0.105c. In the booster and ATLAS linacs, 33 superconducting solenoids are used for focussing.

As described in Chapter 1, heavy-ion fusion-evaporation reactions are very well suited to experiments that rely on the production of proton-rich nuclei with

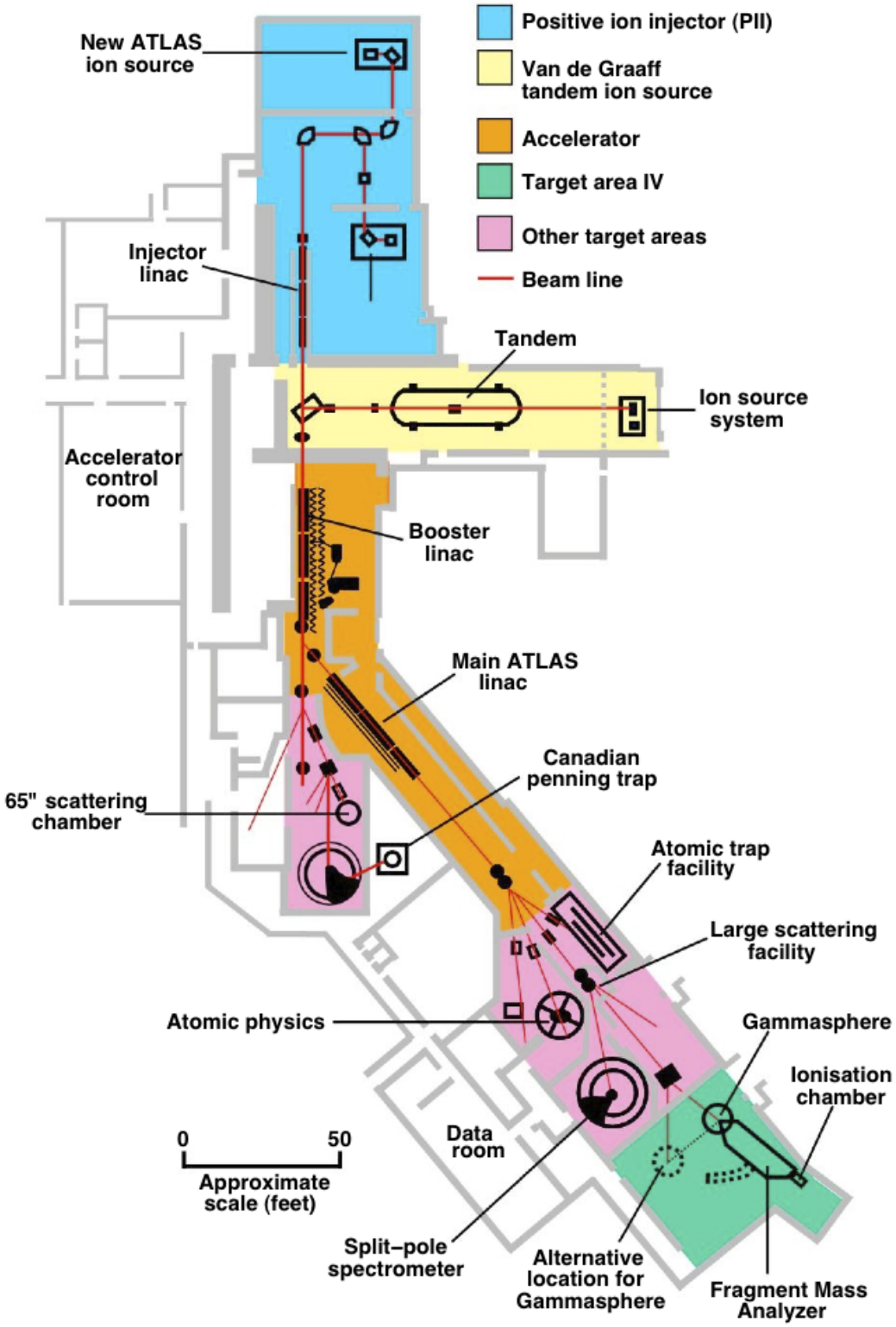

Figure 4.2 Layout of the Argonne tandem-linac accelerator system [89].

cross-sections large enough to allow feasible experimental measurements to be made, and were therefore used in all of the present studies. The choice of beam and target configurations is highly dependent on material availability and suitability. The experimental work investigating the nucleus ^{62}Ga in the present work employed the ^{40}Ca + ^{24}Mg heavy-ion fusion-evaporation reaction. Reactions using inverse kinematics, as used in the present work, maximise the transmission efficiency through the FMA, which is described in Section 4.4.1. The beam species ^{40}Ca was chosen as it is a stable, doubly-magic nucleus that can be reliably produced and accelerated by ATLAS. Suitable ^{24}Mg targets were made in the Argonne Physics Division Accelerator target laboratory, one of which is shown in Figure 4.3a).

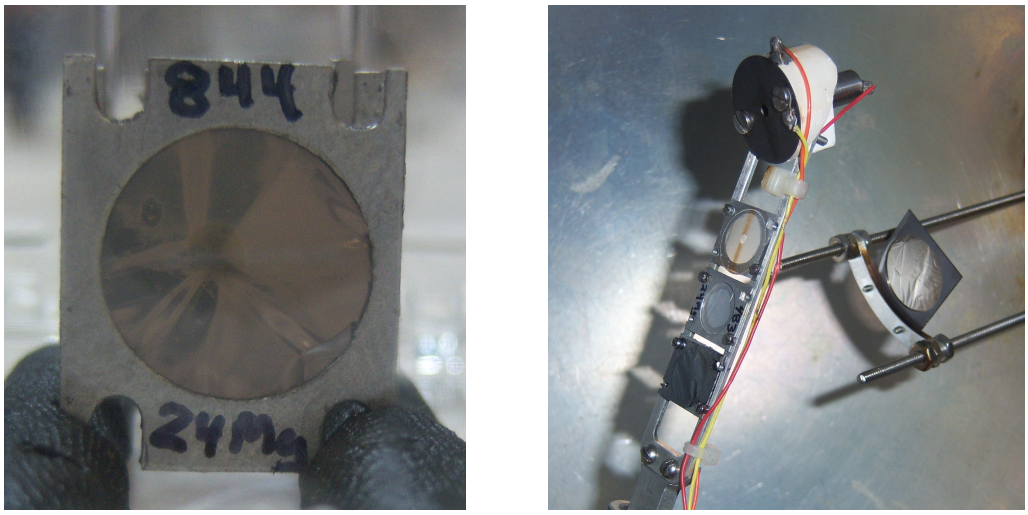

(a) An enriched ^{24}Mg foil target.

(b) Target ladder and thin carbon reset foil positioned inside the Gammasphere target chamber.

Figure 4.3 Photographs of targets.

Target thicknesses and beam energies were chosen to optimise the production of the desired isotopes in heavy-ion fusion-evaporation reactions. A delicate balance between maximising cross-sections for the nuclei of interest and minimising the production of contaminant nuclei must be struck in these considerations. An optimum beam energy should be large enough to overcome the Coulomb threshold in order for fusion to take place, but not so large as to allow too many competing reaction channels to become open. Similarly, an optimum target thickness should be such that the yield of reaction products is maximised without causing significant energy straggling. Loss of efficiency occurs if the energy difference between recoils produced at the front and the back of the target is larger than the

energy acceptance of the FMA, and if significant angular straggling takes place. The optimum target thickness also depends on the durability of the material when subjected to the desired beam intensity, and material uniformity.

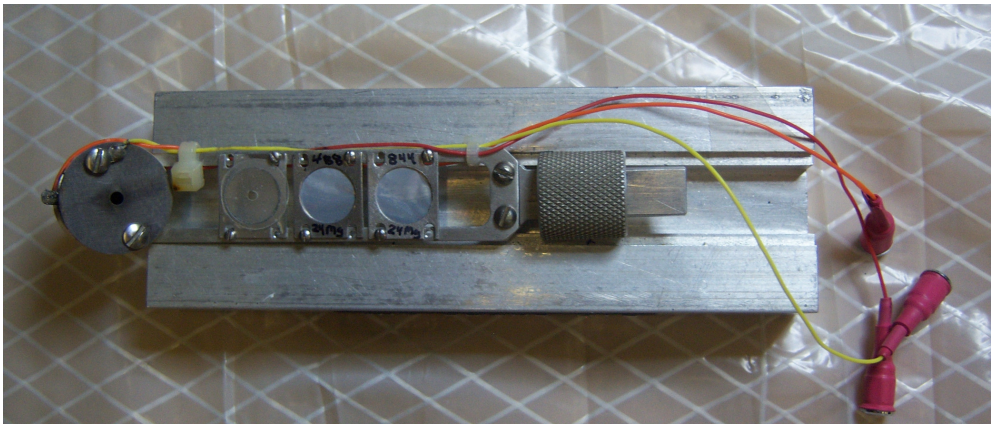

Figure 4.4 Photograph of the target ladder. Mounted from left to right: Faraday cup, plastic scintillator, ^{24}Mg target, ^{24}Mg target.

Once prepared, suitable targets were secured onto a target ladder, shown in Figure 4.4, and secured inside the Gammasphere target chamber. A Faraday cup and a plastic scintillator with a central hole were also positioned on the ladder to aim beam tuning. The target ladder could be moved up or down to allow easy transitions between different targets to be made during experiments without significant adjustment to experimental equipment. A $\sim$20 μg/cm^2 Carbon reset foil was positioned downstream of the target ladder inside the chamber as shown in Figure 4.3b) to equilibriate the charge state of the recoiling reaction products.

4.3 Gammasphere

A critical property of the experimental system is the ability to measure prompt γ rays emitted from reaction products with high efficiency and resolution. The Gammasphere detector array at ANL is a powerful device that provides the ideal environment for γ-ray spectroscopy studies of nuclei produced in fusion-evaporation reactions. The array configuration, designed to maximise solid angle coverage and provide high resolution, has the symmetry of a icosahedron, consisting of 122 polyhedral elements: 110 hexagons and 12 pentagons. Each of the 110 hexagons house a detector module that consists of a cylindrical n-type high-purity Germanium crystal (HPGe), a Bismuth Germanate (BGO) shield and

a liquid Nitrogen cooling system used to minimise thermally induced background. The module layout is shown in Figure 4.6. Each of the modules provide 0.418 % solid angle coverage, totalling 46 % when all detector modules are operational. Whereas Silicon semiconductor detectors of the type discussed in Section 4.5 are suited to charged-particle detection, the reduced mean free path of photons in higher-Z material makes Germanium detectors better suited to high-energy photon detection, particularly as very large ($\sim$ 10 cm) HPGe crystals can be manufactured. Additionally, as less energy is required to create an electron-hole pair in Germanium compared with Silicon, HPGe detectors have superior energy resolution.

The HPGe detectors are arranged into 17 rings, each with one of 9 fixed angles with respect to the beam axis due to a symmetric arrangement about 90°. The angles of each of the 17 rings are shown in Table 4.1. This arrangement accommodates angular distribution measurements and corrections for Doppler broadening effects. The 12 remaining pentagonal elements are used for support structures, input and exit pathways for beam ions or reaction products, or occasionally auxiliary detectors.

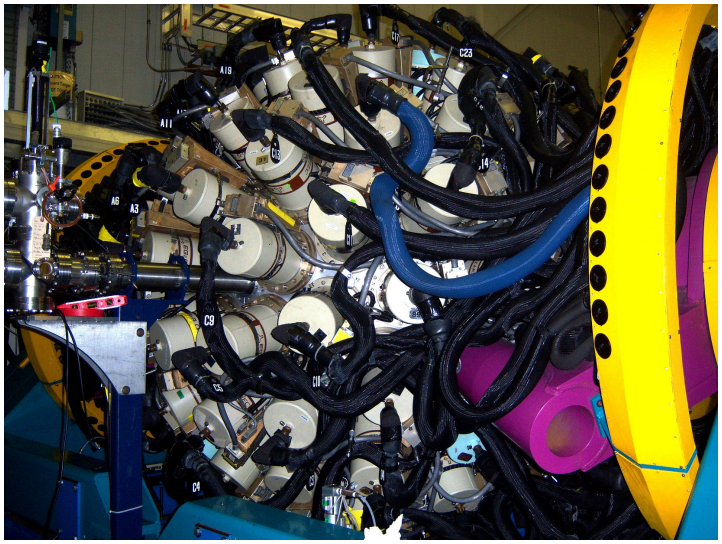

Figure 4.5 The Gammasphere detector array.

It is necessary to remove several of the detectors at the most forward angles (those with $\theta \ll 90°$ with respect to the beamline) when the Gammasphere is used in conjunction with a mass separator, as in this work. Mechanical separation of the array into two hemispheres allows access to a target chamber, which is fully enclosed at the centre of the Gammasphere when the array is in the 'closed' position.

Figure 4.6 Schematic diagram of a Gammasphere detector module [90].

Rings	Number of detectors	θ (deg)
1, 17	10	17.27
2, 16	10	31.72
3, 15	10	37.38
4, 14	20	50.07
5, 13	10	58.28
6, 12	20	69.82
7, 11	10	79.19
8, 10	10	80.71
9	10	90.00

Table 4.1 Arrangement of the 17 detector rings in the Gammasphere array. The angle shown is with respect to the beam axis.

The total energy resolution of a typical HPGe detector depends on a combination of the intrinsic resolution of the detector material and Doppler broadening effects. Although the angular spread and velocity profile of the recoils will contribute to the Doppler broadening, the dominant contribution is typically due to the finite opening angle of each detector. As the effect of the opening angle increases with larger angles relative to the beam axis, many of the detectors with $\theta > 50^\circ$ can be electronically segmented into two D-shaped halves, reducing the effective opening half-angle from 7.4° to 3.7°.

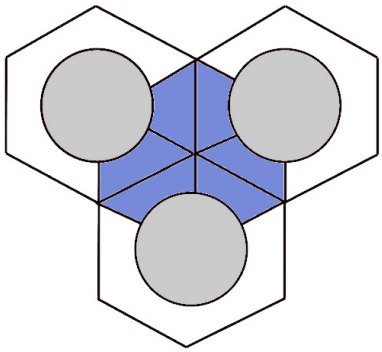

Figure 4.7 Sketch depicting the end view of three Gammasphere detector modules in honeycomb formation. The front ends of the HPGe detectors are shown in grey and the BGO suppression shield in blue.

Although HPGe detectors have excellent intrinsic resolution for γ rays, not all incident γ rays deposit all of their energy entirely within a single HPGe crystal as many will Compton scatter and deposit only a part of their total energy. This effect causes the number of full-energy events recorded compared with partial-energy events (the peak-to-total (PT) ratio) to be only ~ 25 % for a typical HPGe

detector. The PT ratio can be increased to ~ 60 % through the use of Compton suppression to reject partial-energy events.

Each HPGe crystal is surrounded by six BGO suppression elements, as shown in Figure 4.7. Events where an incident γ ray Compton scatters within an HPGe crystal and deposits some or all of its remaining energy in one of the surrounding BGO elements are vetoed. An additional BGO element is used as a back plug for each HPGe crystal to veto events where incident γ rays Compton scatter through small angles. The choice of BGO for Compton suppression shielding is ideal as, unlike with the γ-ray detectors themselves, high efficiency is more important than high resolution. The efficiency of the shielding can be increased further through electronically combining pairs of BGO elements that lie in-between adjacent HPGe detectors. Although events where γ rays from high multiplicity cascades are directly incident on the BGO shielding can cause false vetoes, this effect is minimised through the use of heavy metal ("hevimet") collimators.

4.4 Argonne Fragment Mass Analyzer and ancillary detectors

4.4.1 FMA

The Gammasphere is an extremely sensitive device that provides an ideal environment for γ-ray spectroscopy studies. However, studies of nuclei produced in weak reaction channels are often not feasible using Gammasphere alone as high levels of background from unwanted contaminants swamp the desired signals. The combination of Gammasphere with a mass separator, such as the FMA, is therefore an extremely powerful one as it provides the means for selectivity on γ rays from nuclei of interest.

The FMA is a recoil mass spectrometer designed for use in nuclear physics experiments in order to separate primary beam ions from reaction products, and to provide mass selectivity by dispersing reaction products by their mass-to-charge ratio (A/q). Consisting of two electric dipoles, a magnetic dipole and two magnetic quadruple doublets, the FMA spans 8.2 m in length. The FMA is positioned at 0° with respect to the beam axis in order to match the peak yield of reaction products and maximise transmission through the separator. Unreacted

primary beam ions, which are mixed in with the recoiling reaction products, are stopped at the earliest opportunity on the anode of the first electric dipole. The energy-to-charge dispersion of the two electric dipoles is cancelled by the central magnetic dipole, leaving only A/q dispersion at the focal plane. The dipoles are framed by two quadrupole doublets that act as focussing elements and control the A/q dispersion.

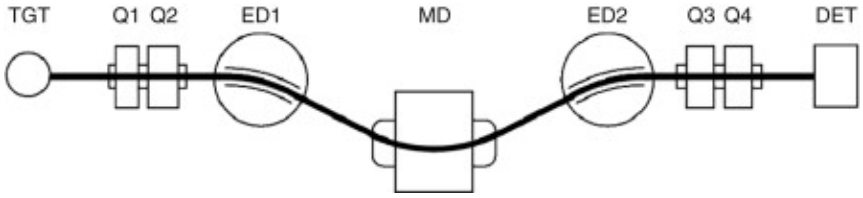

Figure 4.8 Schematic diagram of the Argonne FMA [91].

Setup of the FMA is achieved using a sophisticated control system, interfaced to the hardware, which also provides continuous monitoring of the fields and vacuum. The magnetic and electric fields are adjusted so that recoiling reaction products with inputted values of energy E_0, mass A_0 and charge q_0 are transmitted and focussed to the central point of the focal plane. One of the main benefits of the ion-optical layout is a large energy and A/q acceptance of ± 20 % and ± 4 % around the central values, respectively, as well as 8 msr solid angle coverage.

4.4.2 PPAC

As recoiling reaction products are dispersed by A/q at the focal plane of the FMA, a detector capable of providing position information is critical in order to identify mass groups. Whereas traditional proportional counters can provide energy information for ions, multiwire proportional counters (PPACs) can also give detailed position information. The PPAC consists of two mutually orthogonal wire grids ('X' and 'Y') that are positioned so that the wires in the X plane lie in the direction of dispersion at the focal plane, an anode plane and a cathode plane. The grids are held within a chamber of isobutane gas at 3 Torr between two 0.8 μm mylar windows. Charged particles passing through the chamber will ionise the gas, causing electrons from the resulting electron-ion pairs to accelerate towards the closest wire. The PPAC is a so-called 'proportional' counter as the liberated electrons have enough energy to further ionise the gas, causing an avalanche. The resultant charge collected on the wires is proportional to the energy loss of the incoming charged particle. Delay-line readouts at either end of the wires in

both X and Y provide 2-dimensional position information, whereas an energy loss signal is taken from the cathode.

4.4.3 Ionisation chamber

Unreacted beam ions that pass through the FMA can cause significant contamination problems if they cannot be distinguished from the true recoiling reaction products. An ionisation chamber (IC) adjacent to the PPAC provides Z-selectivity, allowing a clean and efficient method of removing the effect of scattered beam ions. The principle of operation is similar to that of the PPAC, where charged particles passing through a chamber of isobutane gas between two electrodes create electron-ion pairs. A voltage large enough to prevent recombination of the ion pairs is held across the electrodes in order to collect the charge, which is proportional to the energy deposited by the incident particle. The efficiency of the IC is increased by keeping the gas at a pressure of 10-50 Torr, held within two mylar windows. The IC is segmented into 3 anode sections and several sections in the beam direction to reduce pile-up and allow high count rates. A Frisch grid, parallel to the anode, reduces the rise time of the electron pulse, increasing the pulse height and therefore improving signal quality.

4.5 Double-sided Silicon strip detector

As discussed in Chapter 1, many exotic nuclei near the proton drip-line are characterised by fast β decays, with half-lives typically of the order of ~ 100 ms. When designing an experimental technique that proposes to exploit this feature, a means of correlating reaction products with subsequent β decays must be devised. Candidate detector systems must have the ability to determine sensitive position and timing information for implanted recoils and β decays, along with the ability to distinguish between them. These criteria are met through the use of a double-sided Silicon strip detector (DSSD) as an implantation detector at the focal plane of the FMA.

A highly segmented DSSD, manufactured by Micron Semiconductors Ltd to design specifications provided by the Nuclear Physics Group at the University of Edinburgh, was installed at the focal plane of the FMA. The operating principle of any semiconductor detector is based on charge collection from electron-hole

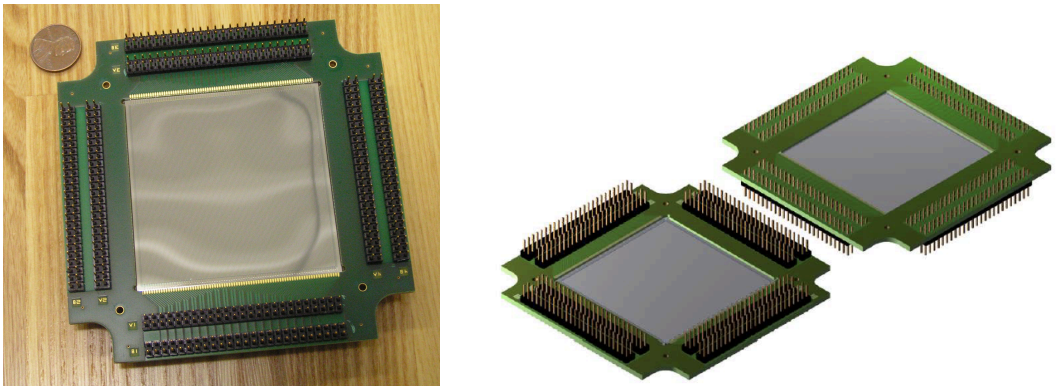

(a) **(b)**

Figure 4.9 a) Photograph of DSSD, b) Front and back layout of DSSD [92]

pairs liberated by incident ionising particles. The DSSD consists of a wafer of n-type bulk Silicon, with 160 n+ strips implanted onto the back surface, and 160 p+ strips implanted onto the front surface. Aluminium contacts coupled to all 320 strips enable electronic readout. A 1 mm thick DSSD was used to maximise the efficiency of β particle detection. This is unlike traditional decay-tagging experiments, where DSSDs are designed for the detection of α or proton radiation and are typically < 100 μm thick to minimise energy deposition from β particles.

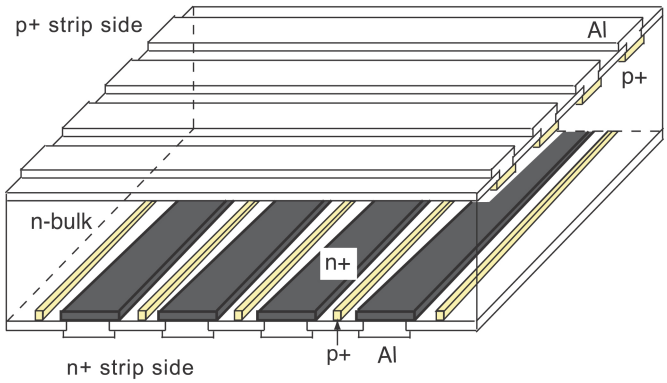

Figure 4.10 Basic DSSD design [93].

Each strip is 390 μm wide and 62 mm long, spaced 50 μm apart. The summation of 160 strips on one side results in a total active area of ~ 3900 mm^2. The strips each have a separate electronic readout, resulting in 25600 'pixels' defined uniquely by each combination of front and back strips. For optimised performance, the DSSD was biased to 50 V and cooled to $-20°$ C. Under these conditions, the leakage current was < 3 μA.

4.6 Digital electronics and data acquisition

In recent years, the Gammasphere and FMA (along with all ancillary detectors) have undergone staged transitions to new digital electronics and data acquisition systems, with full integration successfully tested in the Spring of 2012. Running experiments with digital electronics has several advantages, including up to a 100× increase in count rate, and improved trigger flexibility. Incorporating digital electronics with the DSSD also has significant advantages over analogue systems, including improved signal processing at low energies, and remote electronic control over strip parameters (such as threshold and gain) for all 320 strips. Two independent systems were developed: the digital Gammasphere (DGS) system and the digital FMA (D-FMA) system, the latter including all focal plane detectors and the DSSD. Both are based on the data acquisition and trigger system employed by the 'GRETINA' γ-ray energy tracking array. See reference [94] for detailed information.

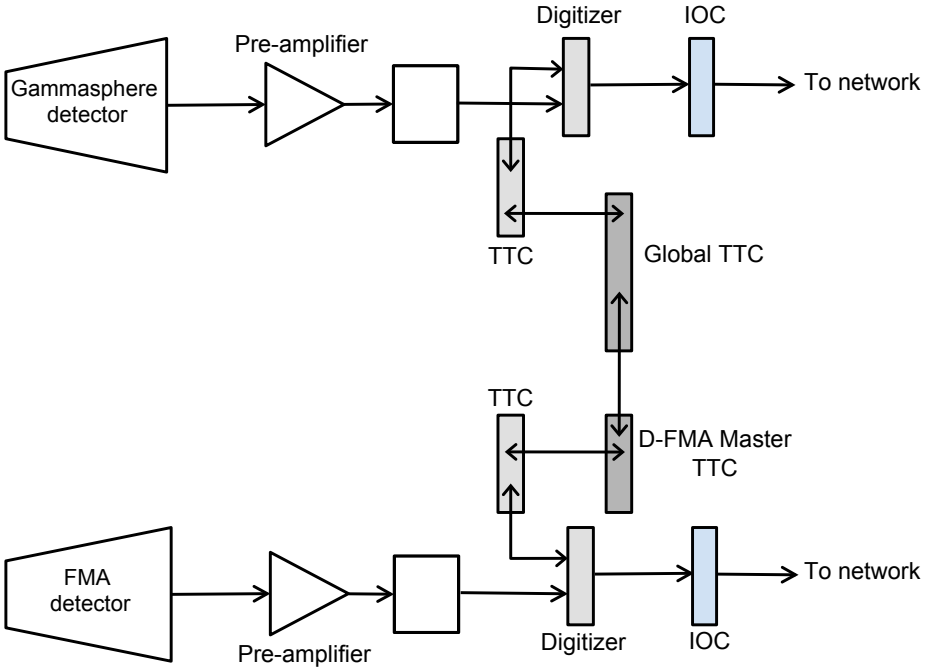

Figure 4.11 Block diagram for detector electronics.

The basic electronics sequence is demonstrated in Figure 4.11. Circuit boxes between the detector pre-amplifiers and custom designed 14-bit GRETINA 10-channel digitizer modules were used to adjust the DC levels and gains of the pre-amplifier outputs to match digitizer input parameters. For the DGS system, the circuit box also serves to convert step signals from the pre-amplifier into

exponential-type signals. The pre-amplifier signals for the DSSD are already exponential-type so conversion is not required. The digitizers then act as analogue to digital converters, each capable of analysing up to 100 Msamples/s, and digitally process the signals to determine energy and timing information. Application specific digitizer firmware replaces the requirement for discriminators, shaping amplifiers and analogue-to-digital convertors (ADCs). All recent event information is stored in buffers within the digitizers while a trigger decision is pending. The processed event information is passed from the digitizers to Trigger Timing and Control (TTC) routers, which can each receive information from up to 8 digitizers.

For the DGS system, a single 'Master' TTC collects the information from all TTC routers and makes a decision based on the pre-programmed trigger requirements whether the current event data should be read out from the digitizers or not. Once this decision has been made, a 'yes' or 'no' command is sent from the Master TTC back through to all of the individual digitizers. If the trigger requirements are met, the data are transferred from the digitizers to Input/Output Controller modules (IOCs), which can each receive data from up to 4 digitizers. Data collected by each IOC can then be written to disk through a network, with each producing an independent output file.

The D-FMA system is similar to the DGS, with one major difference. The Master TTC for the DGS acts as a 'Global' TTC for both systems, so that the D-FMA Master TTC reports to the Global TTC for a trigger decision. This architecture is designed to accommodate the possibility of creating complex triggers incorporating information from both the Gammasphere and FMA. It also provides a means for clock synchronisation, as in order to correlate events detected by the Gammasphere with events at the focal plane of the FMA it is imperative that the clocks governing the event timestamps in the two independent systems remain synchronised. Clock information is issued by the Global TTC to the D-FMA digitizers through the D-FMA Master TTC and TTC routers, as well as to the DGS digitizers through the DGS TTC routers.

For the DGS system, a total of 22 digitizers were required, each receiving inputs from 5 HPGe detector pre-amplifiers and the 5 corresponding BGO pre-amplifiers. The 22 digitizers reported to 2 TTC routers and a Master TTC. Data from the digitizers were written to disk via 11 IOCs. For the D-FMA system, a total of 33 digitizers (32 to accomodate the 320 DSSD strips and 1 additional digitizer for signals from the PPAC and IC) reported to 5 TTC routers and a Master TTC,

which in turn reported to the Global TTC. 9 IOCs collected the data from the digitizers.

Both systems were run in 'internal' triggering mode with no multiplicity requirements, so all signals that exceeded the discriminator threshold were recorded. Although running in this configuration resulted in large amounts of data written to disk, this was sustainable due to the relatively low event rate and allowed maximum flexibility in offline analysis. The 20 independent data files containing data from each of the 11 digital Gammasphere IOCs and the 9 digital FMA IOCs were 'merged' into event format as described in Section 5.1.

4.7 Test experiment

The concept described in Section 4.1 was tested during an experiment at ANL in June 2010. Data collected were analysed thoroughly in order to gain information regarding possible improvements to the system prior to full experiments. Although the information contained previously in this Chapter relate to the full experiments undertaken at ANL in June 2012, the detector hardware setup used in the test experiment was identical to that of the full experiments (with the exception of the DSSD thickness). Consequently, information contained in all Sections in this Chapter are relevant to the test experiment, other than Section 4.6 as the electronics and data acquisition system used in the test experiment were analogue. The analytical techniques implemented for data collected during the test experiment were very similar to those described in Chapter 5, with the exception of Section 5.1, which relates only to the digital acquisition system used in the full experiment.

4.7.1 Experimental details

A beam of ^{40}Ca ions, accelerated to 94 MeV by the ATLAS accelerator, was incident onto a ^{nat}Mg target of thickness 0.7 mg/cm^2. Mass A=62 nuclei were produced via 2-nucleon fusion-evaporation channels. Prompt γ rays emitted close to the target were detected by the Gammasphere detector array, and recoiling reaction products entered the FMA at 0° with respect to the beam axis. It was found through collecting data with the FMA set to transmit nuclei with a range of charge states, q, that charge state 16+ produced an optimum ratio of

A=62 nuclei to scattered beam ions. Consequently, the FMA was set to transmit nuclei with a mass-to-charge ratio of 62/16. In this configuration, nuclei with A/q=62/16 were transmitted to the centre of the focal plane, allowing physical slits to be employed at the sides of the focal plane in order to reduce the amount of unwanted contaminants. Nuclei at the focal plane of the FMA then passed through a PPAC and an ionisation chamber so that energy loss, position and timing information could be determined. Finally, the reaction products were implanted into a 300 μm thick 160×160 DSSD, where timing and 2-dimensional position information for both implanted reaction products and β particles were measured.

4.7.2 Test experiment results

The γ-ray spectrum measured by the Gammasphere in coincidence with all nuclei that were transmitted to the focal plane of the FMA is shown in Figure 4.12a). The strongest transitions in the spectrum are indicated by dashed red lines and originate from the nuclei ^{62}Zn and ^{58}Ni, produced in the strong 2p and α2p evaporation channels, respectively. Despite the FMA settings for transmission of mass 62 nuclei in charge state 16, nuclei with A=58 and q=15 have a very similar mass-to-charge ratio and were therefore also transmitted by the FMA.

The effectiveness of the new system is demonstrated in Figure 4.12b). The events shown in Figure 4.12b) have identical conditions imposed on them as with those shown in Figure 4.12a), except with the additional condition that the implants must be correlated with a β particle in the DSSD within 400 ms of implantation. The spectrum in Figure 4.12b) was made by subtracting a background γ-ray spectrum of all γ rays associated with implants that are correlated with β particles between 1 s and 1.4 s of implantation from the spectrum of γ rays associated with implants that have a decay time of less than 400 ms. See Chapter 5 for details of how the implant-decay correlations and resulting γ-ray spectra are made.

All of the features in Figure 4.12b) can be attributed to known strong transitions in the N=Z nucleus ^{62}Ga, which has a half-life of $\sim$ 100 ms, other than the starred transitions indicated at 589 and 980 keV. The blue dashed lines indicate the position of the strongest transitions at 246, 376 and 571 keV in ^{62}Ga in Figure 4.12a), where they are almost completely obscured by transitions from contaminant nuclei. Note that in Figure 4.12a) the 246 keV transition is obscured by a strong peak at 243 keV from the contaminant ^{62}Cu.

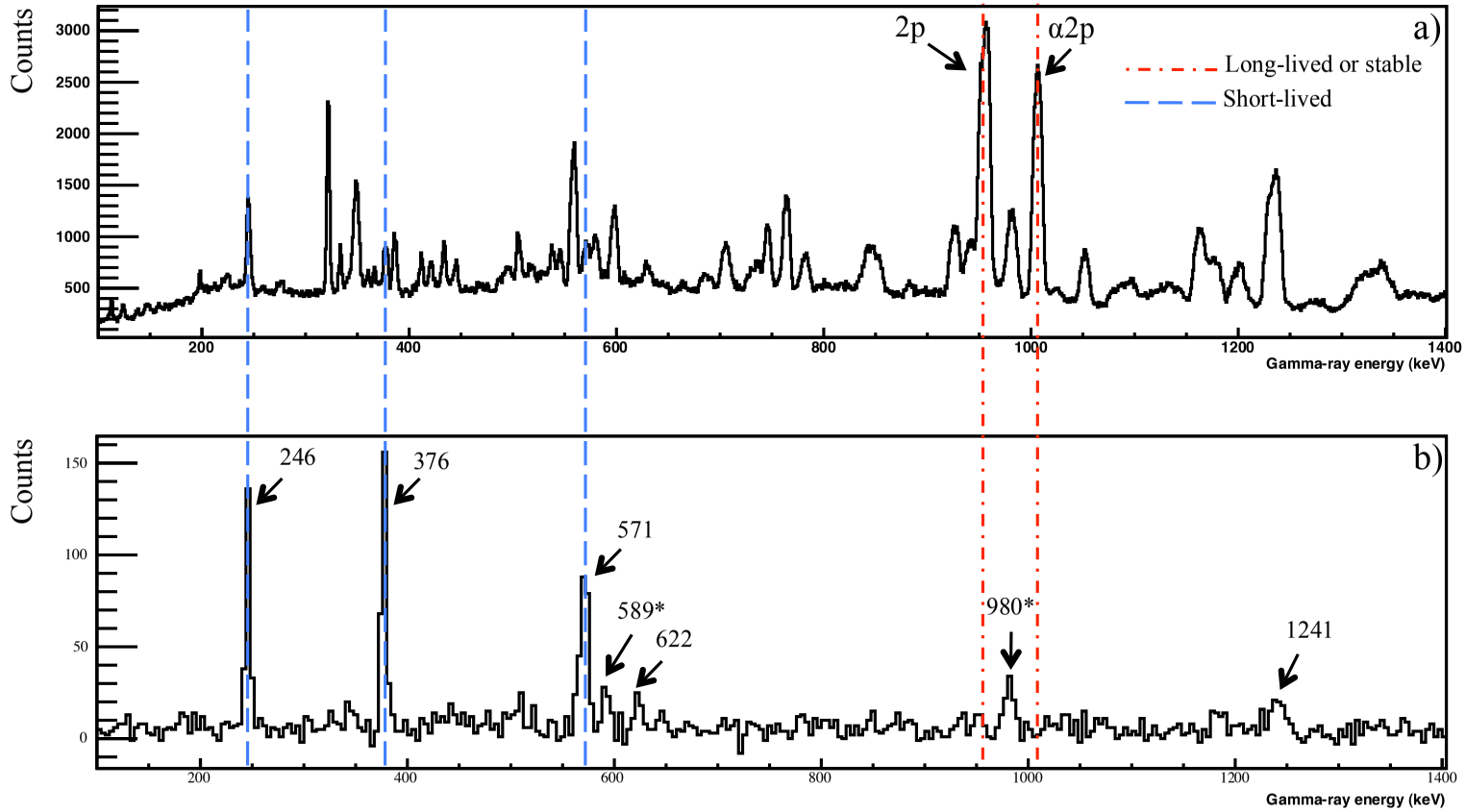

Figure 4.12 a) γ-ray spectrum measured in coincidence with all nuclei that were subsequently implanted into the DSSD. b) γ-ray spectrum measured in coincidence with implants that exhibit fast β decays in the DSSD. The main contaminant transitions emitted from nuclei produced in the α2p (^{58}Ni) and 2p (^{62}Zn) evaporation channels are indicated by dashed red lines. Strong transitions at 246, 376 and 571 keV originating from ^{62}Ga are indicated by dashed blue lines. Transitions at 622 and 1241 keV also originate from ^{62}Ga. Unknown transitions at 589 and 980 keV are starred.

The new system is extremely powerful as contamination from all long-lived or stable nuclei can be subtracted leaving only transitions from short-lived nuclei. Additionally, the timing information provided by the DSSD for the implant and decay events allows a value of the β-decay half-life associated with each γ-ray photopeak to be determined.

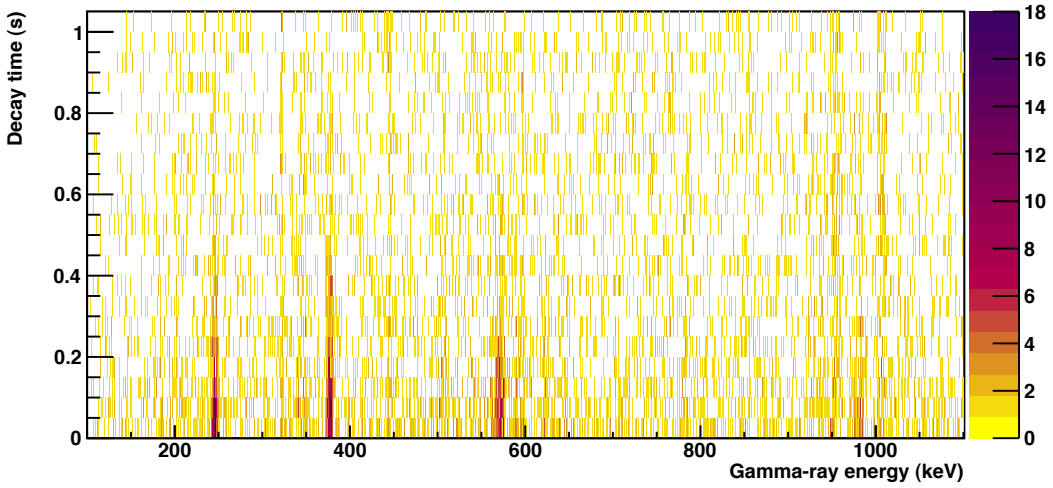

Figure 4.13 2-dimensional intensity plot of β decay time against γ-ray energy for implants that were correlated with β particles in the DSSD.

Transitions from ^{62}Ga are clearly evident in the intensity plot of β decay time versus γ-ray energy shown in Figure 4.13. Values of the 'decay time' are given by the time difference between implanted reaction products and the detection of the correlated β particles in the DSSD. Representing the results in this manner demonstrates the extremely high levels of cleanliness obtained, as background levels for all regions where there are no true short-lived photopeaks are very low.

From consideration of the data analysis procedure, it can be concluded that the starred transitions in Figure 4.12b) at 589 and 980 keV were emitted from nuclei which were transmitted by the FMA and had β-decay half-lives of $\sim$100 ms. No previously known transitions exist in any nuclei produced during the experiment that exhibit such fast β decays. Although a peak exists in Figure 4.12a) at $\sim$980 keV, this is attributed to ^{62}Cu, which has a half-life many orders of magnitude larger than the $\sim$100 ms observed.

It is expected that the exotic nucleus ^{62}Ge was also produced during the experiment. As ^{62}Ge has a half-life similar to that of ^{62}Ga, it is possible that ^{62}Ge is responsible for the 589 keV and/or 980 keV transition. As discussed in Chapter 1, the nuclei ^{62}Zn, ^{62}Ga and ^{62}Ge are isobars, and the discovery of the

isobaric analogue states (IAS) in ^{62}Ga and ^{62}Ge of the 2^+, T = 1 state in ^{62}Zn have yet to be confirmed. As the 2^+ IAS in ^{62}Zn has an energy of 954 keV and is characterised by a strong $2^+ \rightarrow 0^+$ transition to the ground state, the 980 keV transition is a prime candidate for the analogue transition in either ^{62}Ga or ^{62}Ge.

In order to investigate the origin of the new transitions, an attempt was made to perform a "double-β" analysis by requiring that 2 successive β decays were observed a short time after implantation. The nucleus ^{62}Ge is the only species produced that exhibits two successive fast β decays. The result was ambiguous due to low levels of statistics and no conclusions could be drawn. A $\gamma\gamma$-coincidence analysis was also attempted but was also unsuccessful due to low levels of statistics. It was possible, however, to verify coincidences with the strongest yrast transitions in ^{62}Ga.

4.7.3 Improvements to the system

On the basis of the promising results shown in the previous Section, a full experiment to confirm the nature of the new transitions was approved at ANL, with several improvements increasing the level of statistics. Enriched ^{24}Mg targets were decided upon for the full experiment instead of the ^{nat}Mg ones used during the test, drastically reducing the amount of ^{62}Cu produced, which is primarily produced in reactions on ^{25}Mg. A higher implantation rate through higher beam intensity and an increase in beam energy was deemed possible due to the very low levels of contamination evident in the test results. Additionally, a new 1 mm DSSD, more than 3 times thicker than used in the test experiment, was acquired in order to increase the energy deposition of β particles and therefore improve the β detection efficiency. A full experiment would also benefit from the use of the newly installed digital electronics and acquisition systems for the Gammasphere and the FMA (for details see Section 4.6).

Chapter 5

Data analysis

Details of how the raw data collected by the system described in Chapter 4 are translated into a meaningful format are given in this Chapter. Analytical techniques that enable 'implant' and 'decay' event identification are discussed, as are methods used to correlate implants with their subsequent β decays. The analysis procedure for interpreting γ-ray data collected by the Gammasphere is described, and the procedure for extracting β-decay half-lives is discussed.

5.1 Data sorting

Two independent but synchronised acquisition systems as described in Section 4.6 were used during the structure study of ^{62}Ga in the present work. This configuration allows signals measured by an individual detector, or 'sub-events', to be recorded with essentially no triggering requirements in the hardware. In order to analyse the data collected, it is necessary to organise the sub-events into an 'event' format. This is achieved using the "GTMerge" data merging program developed at ANL.

Each data file created contained sub-events relating to up to 40 individual detectors. GTMerge reads these data files simultaneously and produces a single output file containing a stream of 'events' in time order. The program reads through all the input files and locates the sub-event with the earliest timestamp, marking this as the beginning of the first event. All subsequent sub-events with timestamps that fall within a 5 μs time window from the beginning of the event

are collected together into a single object. After the 5 μs time window has elapsed, the current event is written to an output file. The next sub-event marks the start of the next event. The size of the time window is variable and can be adjusted to a size appropriate to the nature of the experiment. In this case, it was found that 5 μs was long enough to encompass all sub-events belonging to the same event, but short enough for sub-events from a given event to be distinguishable from those belonging to previous events.

Two types of event can be identified: implant events and decay events. Events are classed as implants when one or more sub-events from detectors at the focal plane of the FMA are present, indicating that a recoiling reaction product has passed through the FMA. Implant events contain all information related to the recoiling reaction product, including prompt signals measured by the Gammasphere, sub-events from all FMA detectors, and sub-events from the DSSD. Events classed as decay events must contain at least one sub-event from the DSSD, and no sub-events from detectors at the focal plane of the FMA. No Gammasphere information is associated with these events as decay events have no associated prompt γ rays. In order for the new method to successfully provide selectivity on reaction products with short β-decay half-lives, it is necessary to correlate implant events in the DSSD with decay events. Once a clean method of distinguishing between the two classes of event is established, it is possible to use both position and timing information provided by the DSSD to distinguish true short-lived β particle emitters from longer-lived nuclei.

The output file created by GTMerge is collected into meaningful time-ordered events in binary format. The data sorting program "DGSSort" can then be used to perform a preliminary sort and convert the events into "tree" format for use in the "ROOT" analysis toolkit [95].

5.2 Event selection

5.2.1 Implants

Implant events consist of a mixture of both true reaction products and scattered unreacted beam ions. Additionally, a consequence of the A/q ambiguity of the FMA is that reaction products produced in evaporation channels different to the desired evaporation channel can also be transmitted by the FMA. The detectors

at the focal plane of the FMA can be used to distinguish between nuclei with the correct mass and other unwanted contamination. The amount of energy lost by ions passing through the IC is approximately dependent on Z^2, so lower Z scattered beam ions are easily distinguishable from higher Z reaction products. A 2-dimensional plot of the time of flight between the PPAC and the DSSD against the energy loss in the IC, as shown in Figure 5.1, provides a clean way of identifying true recoil events. Reaction products with the correct mass are indicated by the red ellipse.

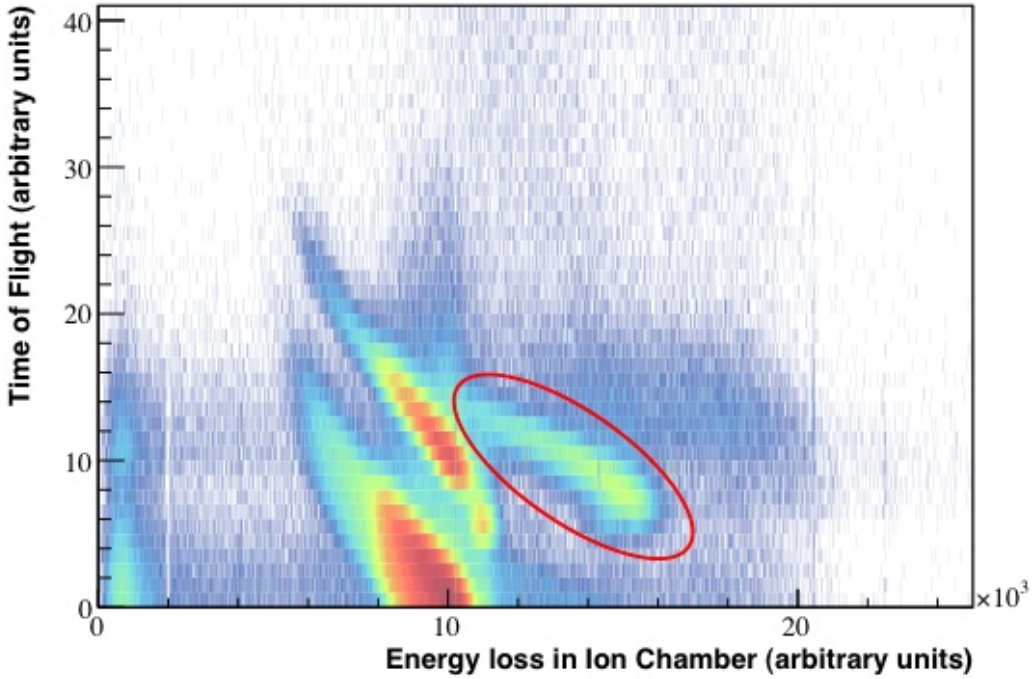

Figure 5.1 Time of flight against energy loss.

As the ability to make implant-decay correlations depends on precise 2-dimensional position information for events in the DSSD, both implant and decay events must have a strip multiplicity condition of at least 1 on both the front and back sides of the DSSD. In cases where the strip multiplicity exceeds 1 on either side of the DSSD, the strip that has measured the largest energy deposition is selected as the true position. As the strip dimensions (300 μm wide and 1 mm thick) are large compared with the average distance travelled by a reaction product in Silicon, implant events with strip multiplicities exceeding 1 are caused by charge sharing effects and are rare.

5.2.2 Decays

Decay events, despite containing only information provided by the DSSD, are considerably more complex to select than implants due to the nature of the particles emitted. As β decay is a three-body process that also involves an emitted neutrino, the β particles themselves do not have a characteristic energy, unlike in proton or alpha decay. A consequence of the energy sharing between the two emitted particles is that the β particle can have any energy between zero and the decay end-point, which is typically $\sim$10 MeV for Fermi superallowed decays, precluding the use of an energy window as a 'gate'. Additionally, the β particles have low Z and energies of up to $\sim$10 MeV, resulting in a large stopping distance relative to the strip dimensions. These factors contribute to a decay detection efficiency in the DSSD of typically $\sim$10 %, which is low relative to an implant detection efficiency of $\sim$70 %. Another contributing factor to the reduced efficiency is the isotropic nature of the decays which, as the parent isotopes are implanted close to the surface of the detector, causes $\sim$50 % of the decays to escape the DSSD entirely without depositing a measurable energy.

As the β particles only deposit a small amount of energy within a single strip in the DSSD (typically $\sim$200 keV), a large proportion of decay events have strip multiplicities exceeding 1. The strips on both sides of the DSSD with the largest amount of energy measured is recorded as the position of the decay in the same way as implant events with multiplicities greater than 1. However, unlike with implant events, having the largest amount of energy deposited within a strip is not a clear indicator of the true origin of the decay. Two major factors govern the amount of energy that the β particle deposits within a strip. Firstly, a β particle will deposit more energy in a strip the larger the distance travelled within it. Secondly, a β particle will deposit increasingly large amounts of energy as it 'slows down'. As the β particles take a random path through the DSSD as they interact with the silicon, neither of these contributing factors are uniquely found in strips where the parent isotope resides. For example, in cases where reaction products are implanted close to the edge of a strip, it is equally likely that the maximum energy deposition is measured in the same strip as the implant or the neighbouring strip. It is also possible that the β particle will deposit less energy in both the strip it originated in and its immediate neighbour, instead depositing a maximum energy 2 strips away from the parent isotope.

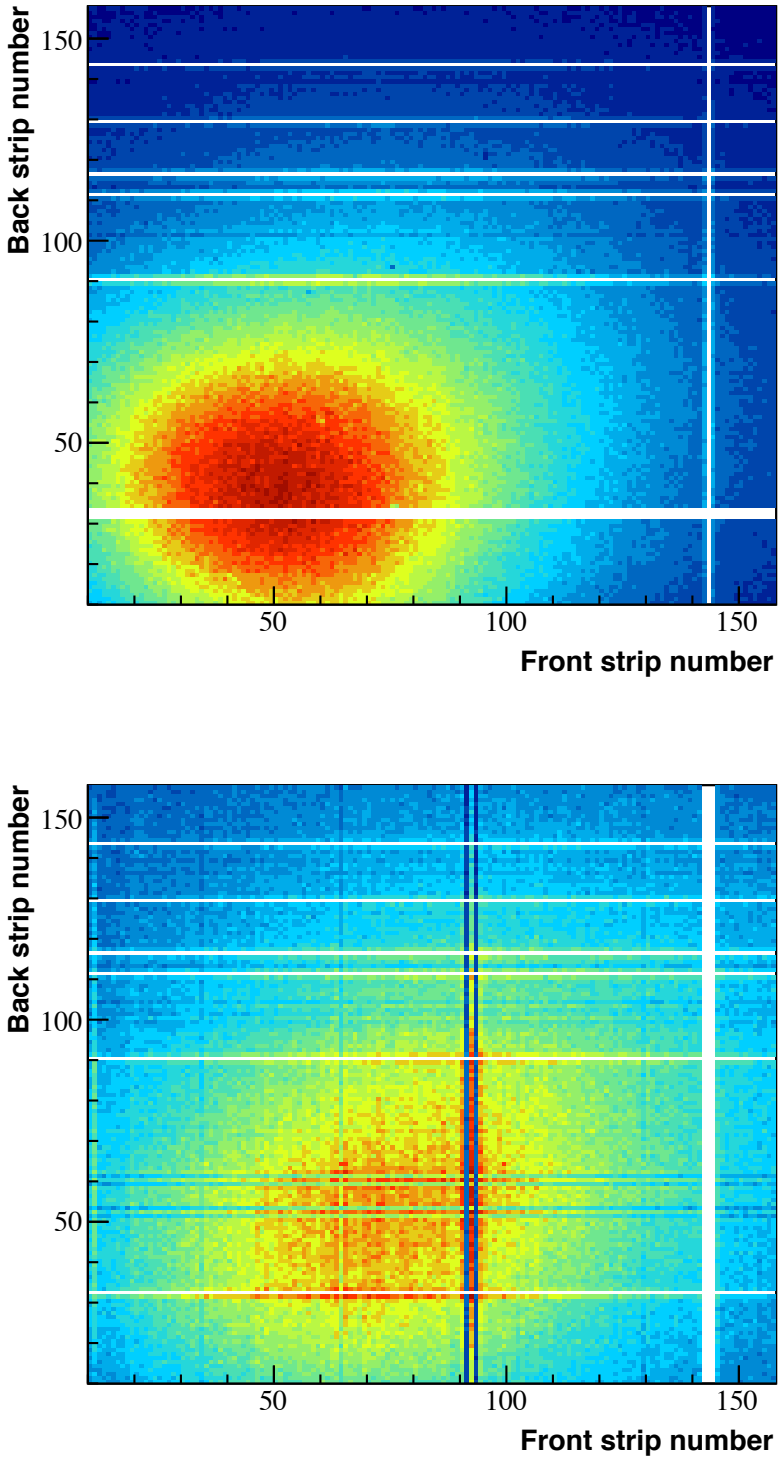

Figure 5.2 Intensity profiles for implant events (top) and decay events (bottom) in the DSSD. 'Missing' strips that were either malfunctioning or found to be noisy were removed in offline analysis and appear white.

Typical intensity profiles for implant and decay events in the DSSD are shown in Figure 5.2. In this example, the central concentration of decay events are shifted with respect to the implants. This is because implant events constitute not only nuclei that exhibit β decays, but also stable contaminant species that have a different mass and charge and therefore take a different path through the FMA and are implanted in a slightly shifted position in the DSSD.

5.2.3 DSSD calibration

Data taken after the main experiments using an alpha source in close proximity to the DSSD was used to gain-match the 320 strips of the DSSD for implant event selection. Although precise energy calibration of the DSSD is not required for implant or decay events, gain-matching maximises the number of correctly assigned implant positions. No gain matching was attempted for decay events, as this could result in a loss of efficiency as very small signals could be 'pushed' sub-threshold.

5.3 Implant-decay correlations

Once the timing and 2-dimensional position information is established for all implant and decay events in the DSSD, correlations between implanted reaction products and their subsequent β decays can be made. The aim of making such correlations is to use the decay time (the time between implanted recoils and their subsequent β decays) to select implants that exhibit fast β decays. This information can then be used to make spectra containing only γ rays emitted by short-lived isotopes.

Spatial correlations between the position of implants and decays are non-trivial, due to the complex nature of the decay events. The simplest form is a 'single pixel' correlation, where the decay must be detected in the same pixel as the preceding implant. Each decay is 'paired' with the most recent implant event that has occurred in the same pixel.

With this method, it is possible for a short-lived implant to be followed by a long-lived (or stable) implant event within the same pixel before the 'true' decay event occurs. In this scenario, which is demonstrated in Figure 5.3, the short-

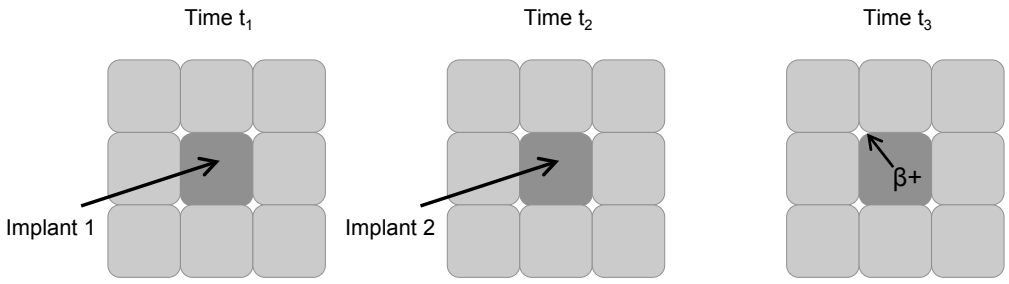

Figure 5.3 Sketch of a portion of the DSSD with three events occurring in a single pixel at times t_1, t_2 and t_3 (where $t_1 < t_2 < t_3$). Implant 1 is a short-lived isotope that undergoes β decay at time t_3, whereas implant 2 is a long-lived (or stable) contaminant. In this scenario, implant 2 is incorrectly assigned a short decay time.

lived implant would be ignored, and the second implant would be incorrectly assigned as a short-lived isotope, providing a source of background. However, the global implantation rate in the DSSD is typically ~ 50 Hz, which translates to a 'per-pixel' implantation rate of 1 every 340 s (assuming that approximately 66 % of the available 25600 pixels are illuminated by the beam spot). This is extremely long compared with the ~ 100 ms half-lives of the nuclei of interest, causing the probability of a random implant event occurring in the middle of a true correlation to be negligible.

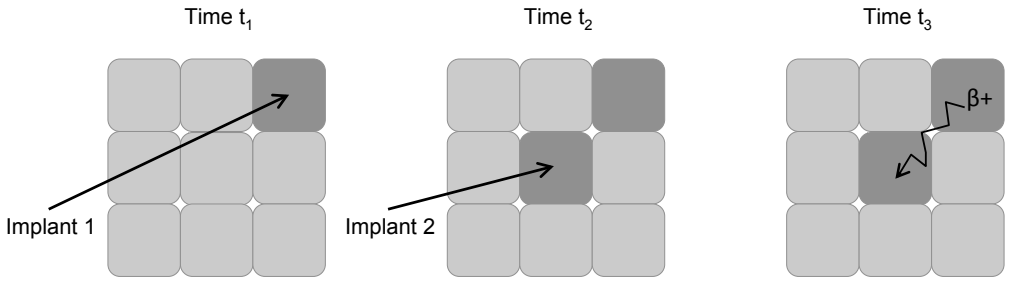

Figure 5.4 Sketch of a portion of the DSSD with three events occurring at times t_1, t_2 and t_3 (where $t_1 < t_2 < t_3$). Implant 1 is short-lived and emits a β particle at time t_3, whereas implant 2 is long-lived (or stable). The maximum energy deposition from the decay event occurs in the same pixel as implant 2, adjacent to the parent implant. Implant 2 is then incorrectly assigned a short decay time.

Another source of background, demonstrated in Figure 5.4, occurs when long-lived (or stable) implants are followed shortly by a β particle that has been emitted from a nearby pixel. As β particles can travel through several pixels, and not necessarily deposit a maximum energy in the pixel it originated from, it is possible for long-lived implants to appear short-lived and for the true short-lived implant to be missed. As the rate of decay events in the DSSD is smaller than the implant rate, this contribution to the background is also negligible.

Although the level of background contamination when using single pixel correlations is very low, this type of correlation suffers inherently from a low efficiency for correlating short-lived implants with their decays as a large proportion of the β particles emitted will not deposit a maximum energy in the pixel they originated from. 'Nearest neighbour' correlations take this effect into account and consequently have a higher efficiency. In this type of correlation, decay events are paired with implant events that may have occurred either in the same pixel as the decay, or in a neighbouring pixel.

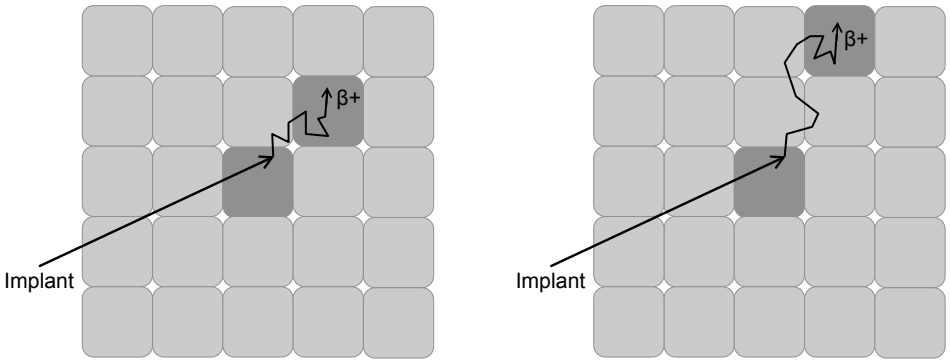

Figure 5.5 Sketch of a portion of the DSSD demonstrating 1 nearest neighbour (left) and 2 nearest neighbour (right) correlations.

The inclusion of 1 nearest neighbour events boosts the correlation efficiency from 3 % to 13 %, with 2 neighbours increasing it further to 20 %. However, there are disadvantages to using nearest neighbour correlations as widening the spatial tolerance between implant and decay events also increases the probability of random events of the types demonstrated in Figures 5.3 and 5.4. Incorporating 1 and 2 nearest neighbour correlations increases the tolerance area by a factor of 9 and 25, respectively. Although this significantly increases the level of contamination from long-lived or stable isotopes compared with single pixel correlations, the global implant and decay rates in the DSSD are sufficiently low to prevent an unacceptable signal-to-noise ratio. Levels of contamination were found to be too high for correlations incorporating 3 or more nearest neighbours.

An additional source of background in implant-decay correlations arises from the fact that not all contaminant species are stable. A small number of long-lived nuclei will undergo β decay a very short time after implantation (within 400 ms) and contribute to the background. Although the implantation rate of long-lived species is much higher than the rate of short-lived species, the overall implantation rate is sufficiently low for this effect to be considered negligible.

As all of the exotic nuclei of interest in this thesis work have β-decay half-lives $\tau_{1/2} \sim 100$ ms, implants with decay times of up to 400 ms will contain ~ 94 % of all implants of interest. Implants with decay times of more than 400 ms can be used to provide an accurate background representation that can then be subtracted. In the context of this work, "short-lived" is used to describe isotopes with half-lives of the order of 100 ms.

5.4 γ-ray analysis

Although the correlation procedure using the DSSD yields a clean method of selecting exotic reaction products of interest, it is the prompt γ rays emitted by the recoils that provide us with the structure information that is so essential to understanding exotic nuclei. The ability to make precise energy measurements using the Gammasphere relies not only on the hardware itself, but also on appropriate data analysis techniques. Details of these techniques are provided in the following Sections.

Calibration

In order to obtain energy measurements of γ rays detected by the Gammasphere, it is necessary to calibrate all of the ~ 100 HPGe detectors so that data collected by each can be summed together. Calibration and gain matching was achieved through the positioning of known γ-ray emitters in the centre of the Gammasphere array at the end of the experiment, when no beam was incident on the target. Calibration data were collected using ^{152}Eu and ^{56}Co sources as these isotopes have known γ-ray lines in the energy region of interest. A linear function relating channel number to energy for each detector was obtained through analysis of the source data.

Doppler correction

Prompt γ rays emitted by recoiling reaction products are subjected to Doppler shifts as the recoils have non-zero velocity when they de-excite. Recoils produced in fusion-evaporation reactions in inverse kinematics typically travel at a few percent of the speed of light as they move away from the target, causing the

shift to be significant. The measured γ-ray energy, E'_γ, is given by the relativistic Doppler equation,

$$E'_\gamma = E_0 \frac{\sqrt{1-\beta^2}}{1-\beta\cos\theta}, \tag{5.1}$$

where β is the ratio of the recoil velocity to the speed of light, θ is the angle of emission with respect to the recoil velocity and E_0 is the true energy of the γ ray. As only recoils moving at close to 0° with respect to the beam axis are accepted by the FMA, the angle of emission θ can be approximated as the detector angle. The detector angles of the Gammasphere are well known (see Table 4.1), allowing a correction to the Doppler shift to be applied in offline analysis. For each experiment the value of β will vary as the recoil velocity depends on experimental parameters (e.g. beam energy, reaction kinematics, evaporation channel of nuclei of interest). The value of β, deduced by plotting E'_γ as a function of detector angle, was found to be 0.0419 for the ^{40}Ca+^{24}Mg reaction used in the present work.

Timing

As the velocity distribution of the recoils is narrow, the time taken for the recoils to pass through the FMA is well defined. This information can be used to reduce background from random γ rays that are continuously detected by the Gammasphere.

Figure 5.6, showing the time difference between γ rays detected in the Gammasphere and ions passing through the PPAC, demonstrates the cleanliness gained by only considering γ rays associated with recoils that satisfy energy loss requirements in the IC. The continuum is made up of random γ rays, whereas the peak at ~ 1 μs consists of γ rays emitted from recoils that pass through the FMA. Further cleanliness can be achieved by rejecting γ rays that fall outside of the time peak.

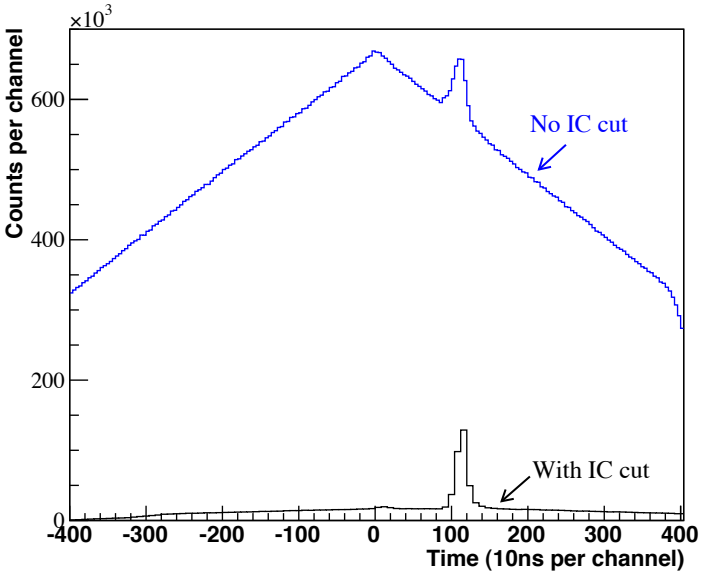

Figure 5.6 Time between Gammasphere and PPAC.

Compton suppression

The Gammasphere array features BGO shields surrounding each HPGe crystal, as described in Section 4.3, in order to provide a means to reject events where γ rays Compton scatter out of the HPGe crystals and only a portion of the full energy is deposited. This event rejection is performed in offline analysis by only including γ rays that have been detected in an HPGe detector without any energy deposition in adjacent BGO shield elements.

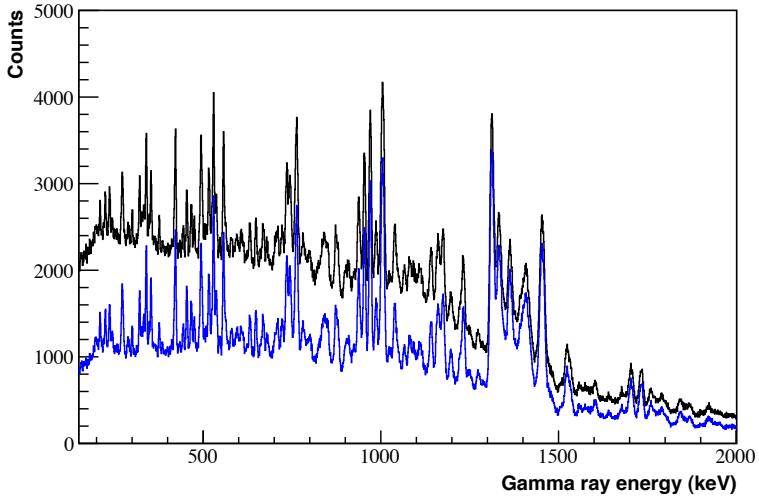

Figure 5.7 Spectrum of γ rays measured by the Gammasphere, with (blue) and without (black) Compton suppression.

Efficiency correction

The efficiency of HPGe detectors vary depending on the energy of the incident γ radiation. An understanding of this energy dependence is necessary in order to determine the relative intensities of γ-ray transitions. Information regarding the absolute efficiency of the Gammasphere is not necessary for this thesis work as only the relative intensities are of interest. A functional form of the energy dependence was determined through analysis of calibration data taken with ^{152}Eu and ^{56}Co γ-ray sources.

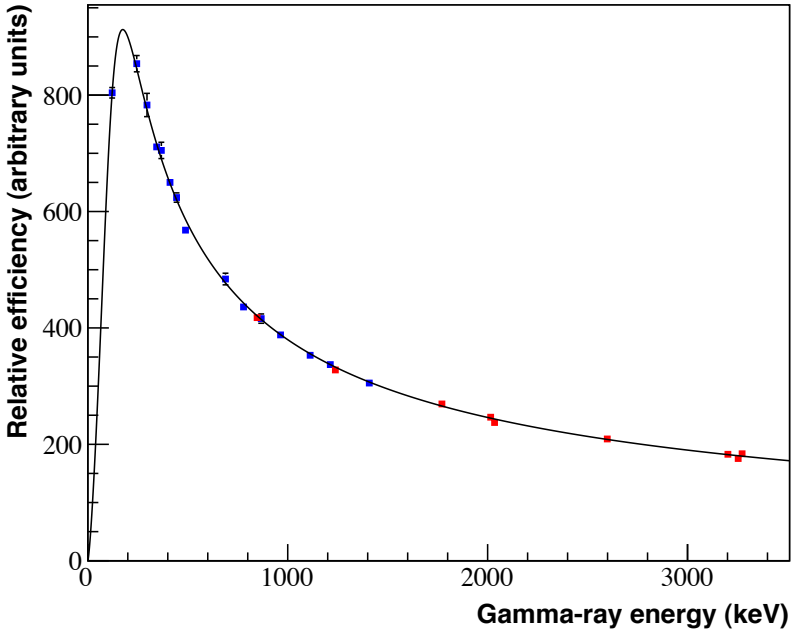

Figure 5.8 Efficiency curve for the sum of all Gammasphere detectors, obtained using ^{152}Eu (blue) and ^{56}Co (red) calibration data.

The number of counts in photopeaks with known relative intensities were established for both sets of calibration data and renormalised to allow a composite analysis. The RadWare software package 'EFFIT' [96] was used to fit a curve of the form

$$\epsilon_{rel} = exp\left\{\left[\left(A + Bx + Cx^2\right)^{-G} + \left(D + Ey + Fy^2\right)^{-G}\right]^{-\frac{1}{G}}\right\} \qquad (5.2)$$

to give the relative efficiency, ϵ_{rel}, for the detection of γ rays with energy E_γ (in keV). In this functional form, the constant parameters A, B and C characterise the low energy region (C is typically set to 0). Similarly, D, E and F characterise

the high energy region. G describes the interaction between the two energy regions, and the variables x and y are given by

$$x = ln\left(\frac{E_\gamma}{100}\right), \quad y = ln\left(\frac{E_\gamma}{1000}\right). \tag{5.3}$$

γ-ray coincidences

The event format described in Section 5.2 allows all γ rays detected by the Gammasphere in coincidence with the production of a given implant to be collected together. This enables an analysis of which specific γ-ray transitions appear in coincidence with each other by the creation of 2-dimensional $\gamma\gamma$ matrices. These matrices are made by incrementing the number of counts at position (x, y) and (y, x) for every pair of coincident γ rays, where x and y are the γ-ray energies. As such, $\gamma\gamma$ matrices are symmetric about $x = y$.

Consider 3 γ rays with energies $E_{\gamma1}$, $E_{\gamma2}$ and $E_{\gamma3}$, detected in coincidence with a single implant. The $\gamma\gamma$ matrix would then be incremented at ($E_{\gamma1}$,$E_{\gamma2}$), ($E_{\gamma2}$,$E_{\gamma1}$), ($E_{\gamma1}$,$E_{\gamma3}$), ($E_{\gamma3}$,$E_{\gamma1}$), ($E_{\gamma2}$,$E_{\gamma3}$) and ($E_{\gamma3}$,$E_{\gamma2}$). This procedure is repeated for every implant. Once all implants have been considered, it is possible to establish which γ rays are coincident by placing energy 'gates' in one of the dimensions, say x, on the completed matrix. If this gate contains a photopeak at energy E_γ, projecting the contents of the energy gate onto the y axis results in a 1-dimensional spectrum showing the number of events coincident with E_γ over all γ-ray energies.

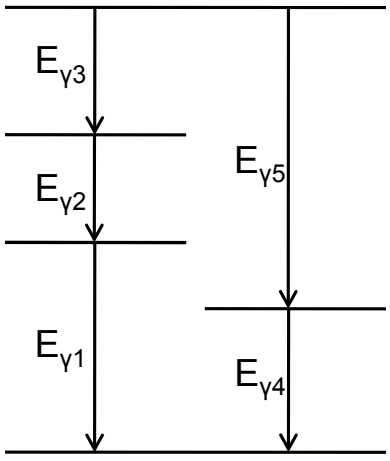

Figure 5.9 Example level scheme.

Analysis of γ-ray coincidences provides the ability to construct level schemes for implants as cascades of coincident γ rays can be determined. The relative intensity of transitions within a coincidence gate also indicates the ordering in a cascade. The example level scheme shown in Figure 5.9 illustrates the example given above, where γ rays with energy $E_{\gamma 1}$, $E_{\gamma 2}$ and $E_{\gamma 3}$ are detected in coincidence. An energy gate surrounding $E_{\gamma 1}$ in the $\gamma\gamma$ matrix for this example would result in a spectrum containing peaks at $E_{\gamma 2}$ and $E_{\gamma 3}$. Energy summing considerations can also be used in the construction of level schemes. In the example shown in Figure 5.9, the sum $E_{\gamma 1} + E_{\gamma 2} + E_{\gamma 3}$ must equal the sum $E_{\gamma 4} + E_{\gamma 5}$ within experimental error, as the initial and final energy levels for these cascades are the same. The Gammasphere has the ability to provide angular distribution information for transitions in cases where there are sufficient statistics. Conservation of angular momentum in γ decay must also be considered when constructing level schemes.

5.5 β-decay half-lives

The histogram shown in Figure 5.10 demonstrates how implant-decay correlations are used to provide γ-ray selectivity on short-lived isotopes by plotting the β decay time of each correlated implant against the energy of all prompt γ rays detected in coincidence with the production of the implant.

The β-decay tagging method described in this thesis work not only allows γ rays emitted by long-lived species to be rejected, but also provides the means to determine the β-decay half-lives of the short-lived isotopes produced. Intensity plots of the type shown in Figure 5.10 can be used to establish the decay half-life associated with specific γ-ray transitions. Placing a 'gate' that encompasses a γ-ray energy region in the histogram allows a spectrum of intensity against decay time for a given γ-ray energy to be created, as shown in Figure 5.11.

Extracting the true β-decay half-life associated with a given γ-ray transition requires further analysis once the decay profile, as in Figure 5.11b), is established. Contributions to the decay profile other than full energy γ rays that are associated with true short-lived species arise from a number of different sources and must be removed.

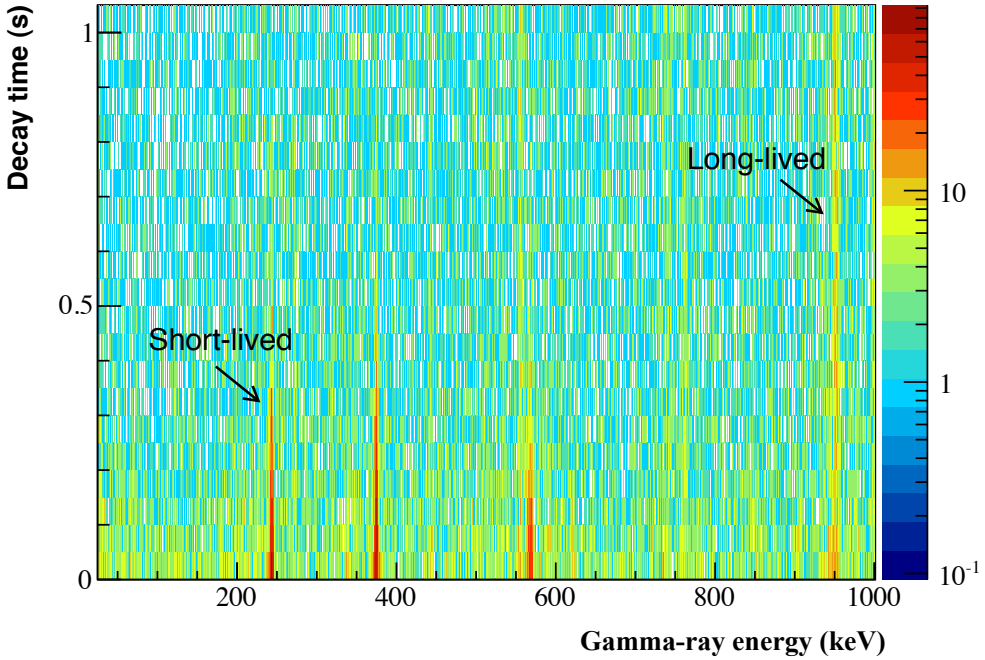

Figure 5.10 Intensity plot of decay time against γ-ray energy for correlated implants.

All contributions to the decay profile can be classified into the following 4 groups:

1. γ rays emitted from short-lived isotopes that are correctly correlated with their own β decay,
2. γ rays emitted from long-lived isotopes that are correctly correlated with their own β decay,
3. γ rays emitted from isotopes that are randomly correlated with a β particle,
4. γ rays that have Compton scattered in the detector and deposited only a fraction of their full energy.

Events arising from contribution 1 are of interest, whereas events from contributions 2, 3 and 4 must be removed. The situation is simplified for the cases described in this thesis work as the number of events arising from contribution 2 can be considered negligible. This is because all long-lived species have characteristic lifetimes that are much longer than the 'random' lifetime. In other words, the probability of a long-lived implant undergoing β decay before being correlated with a random β particle is negligible.

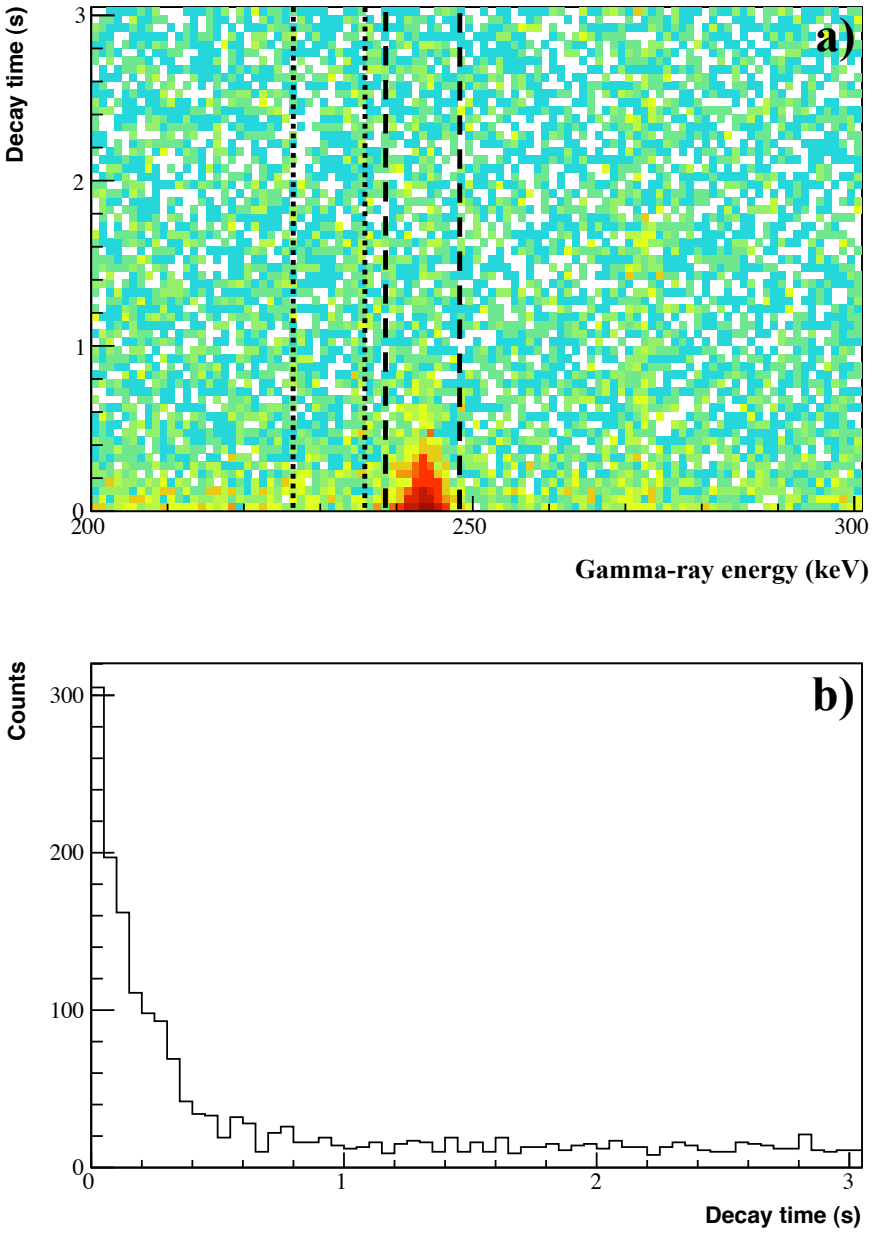

Figure 5.11 a) Intensity plot of decay time against γ-ray energy for correlated implants. b) Intensity against decay time for γ rays with energies that fall within the black dashed lines shown in a). The black dotted lines to the left of the peak in a) indicate a suitable region for determining the contribution to the decay profile due to Compton scattered events.

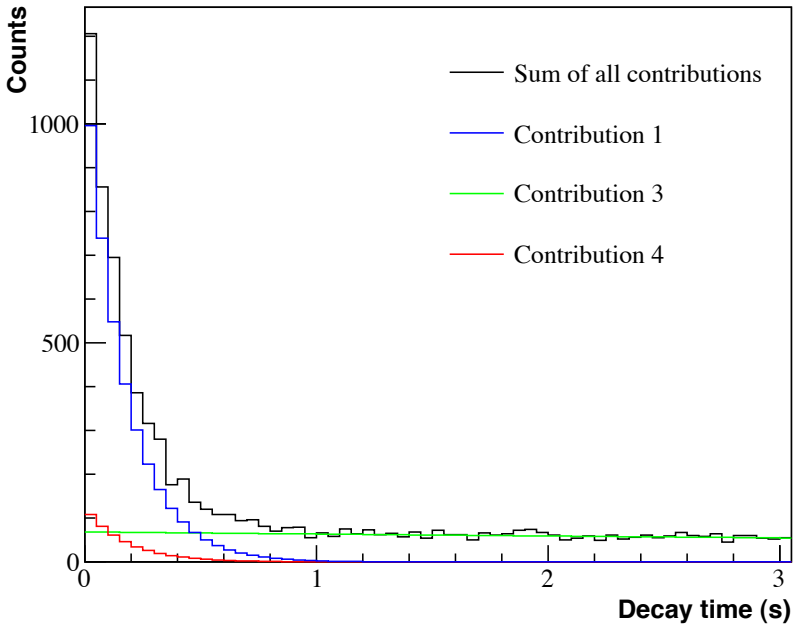

Figure 5.12 Typical decay time distribution for a γ-ray transition, showing the form of all contributions.

As contribution 2 can be neglected, only events from randomly correlated implants and Compton scattered γ rays need to be considered. The distribution of decay times for random events that form contribution 3 has the form of an exponential, given by $Ae^{(-Bt)}$, where A and B are constants and t is the decay time. The parameters A and B can be determined by fitting the decay time distribution from decay times of 1 s up to 10 s, as events arising from contributions 1 and 4 are negligible in this time region. The full functional form for all decay times can be determined through extrapolation back to 0 s.

The form of contribution 4 is determined by a similar analysis as described above for contribution 3, but applied to an energy region shifted with respect to the photopeak, where there are no events from contribution 1. An example of a suitable shifted region is indicated by the black dotted lines in Figure 5.11a). It is assumed that the decay time distribution arising from Compton scattered γ rays is uniform across small energy changes, and that the functional form is also exponential as in contribution 3. The decay profile for this shifted energy region only consists of contributions 3 and 4, thus the functional form for contribution 4 can be determined by first determining the form of contribution 3 using the same procedure as described above and then subtracting. The functional form for the remaining events, which arise only from contribution 4, can then be fitted. All fitting was carried out using the "ROOT" analysis framework [95].

Chapter 6

Results from the structure study of the N = Z nucleus ^{62}Ga

Results from the structure study of the proton-rich nucleus ^{62}Ga carried out at the Argonne National Laboratory are presented in this Chapter. A major aim of the experiment was to identify the origin of a transition previously observed at ∼980 keV, shown in Section 4.7.2, in an experiment designed to test the new experimental system. Additionally, emphasis was put into searching for several low-lying states with low spin that have been predicted in several theoretical calculations but never observed. The interplay between low-lying T = 0 and T = 1 states is of particular interest in nuclei with N = Z, as explained in Section 2.2. This Chapter also includes a discussion of the results from the present work in the context of previous experimental results and theoretical predictions.

In the present study, a 103 MeV beam of ^{40}Ca ions was used to bombard a 488 μg/cm^2 target of isotopically enriched ^{24}Mg, producing ^{62}Ga nuclei via the evaporation of one proton and one neutron in heavy-ion fusion-evaporation reactions. Prompt γ rays emitted at the target were measured by the Gammasphere detector array. Charge states of recoiling reaction products were equilibriated using a $\sim$ 20 μg/cm^2 Carbon reset foil positioned downstream of the target. Nuclei with A/q = 62/18 were transmitted to the focal plane of the FMA, where energy loss and position information was obtained using a PPAC and IC. Finally, reaction products were implanted into a 1 mm thick 160 × 160 DSSD, allowing correlations between implanted reaction residues and subsequent β decays to be made in offline analysis. A total of ∼4.5 days of data were collected. Full details

of the experimental setup and data analysis methods are provided in Chapters 4 and 5, respectively.

A summary of the results obtained in the current work is given in Table 6.1, and the associated level scheme shown in Figure 6.1. The first two columns in Table 6.1 present the level energies, E_x, and γ-ray transition energies, E_γ, reported in a previous study by Rudolph *et al.* [31]. Relative intensities of the γ-ray transitions observed in the Rudolph work, normalised with respect to the 376 keV transition, are given in the third column of Table 6.1. The remaining six columns in Table 6.1 present the results obtained in the current work. Newly observed levels are shown in bold in Table 6.1 and will be discussed in the following Sections, as will any significant differences between results obtained in the present work and previous studies.

The fourth and fifth columns of Table 6.1 indicate the excitation energies, E_x, and γ-ray energies, E_γ, for all levels and transitions observed in the current study. All peak fits were carried out using the RadWare software package 'gf3' [96], allowing energies and photopeak areas to be extracted. The 3^+ yrast state at 817 keV was found to be isomeric with a mean lifetime of 4.6(16) ns in the Vincent study [43]. It was not possible, therefore, to obtain a precise energy measurement for the 246 keV transition in the present work due to Doppler effects. A value of 570.8(3) keV was obtained for the 571 keV transition from the coincidence spectrum for the 590 keV transition shown in Figure 6.8, as the 590 keV transition feeds the 571 keV state directly thus removing any Doppler effects caused by the isomeric 3^+ state at 817 keV. Stars are in place of the excitation energies of the 571 and 817 keV levels in Table 6.1, as these values (used to calculate higher-lying states in the present work) were taken from the study by Rudolph *et al.* [31], where Doppler effects were removed by a Tantalum target backing that stopped recoiling reaction products. Although a measurement of the 571 keV transition energy was obtained in the current study, the lower level of statistics in coincidence data in the present work resulted in a less precise value than the one obtained in the Rudolph study.

Transitions in brackets in Table 6.1 were observed either in singles or coincidence spectra and could not be unambiguously placed in the level scheme on the basis of the current results, but have been tentatively placed in the scheme based on previous observations by Rudolph *et al.* Tentative transitions at 968.2(14), 847.3(13), 878.5(11) and 920.1(26) keV were also observed in singles spectra, but could not be placed within the level scheme and are therefore not shown in Table 6.1.

E_x (keV) Rudolph	E_γ (keV) Rudolph	I_{rel} (%) Rudolph	E_x (keV) Present	E_γ (keV) Present	I_{rel} (%) Present	$R_{32:90}$	J_i^π	J_f^π
571.2(1)	571.2(1)	135(5)	*	570.8(3)	135†	-	1^+	0^+
817.2(1)	246.0(1)	112(3)	*	~ 246	112†	-	3^+	1^+
			978.8(4)	978.8(4)	17(2)	0.77(25)	1^+	0^+
1016.7(3)	445.5(3)	1.9(2)	1017.1(7)	445.9(7)	4(2)‡	-	2^+	1^+
			1161.0(3)	182.8(1)	2(1)	0.76(46)	2^+	1^+
				589.5(3)	12(1)	0.72(21)	2^+	1^+
1193.5(2)	376.3(1)	100(3)	1192.9(2)	375.7(1)	100(2)	1.21(11)	5^+	3^+
1439.4(2)	622.3(1)	14.6(6)	1439.1(2)	621.9(2)	13(1)	1.26(36)	5^+	3^+
			1575.1(7)	595.9(9)	3(1)	1.12(54)	$(2, 3^+)$	1^+
				1004.4(11)	5(3)	-	$(2, 3^+)$	1^+
			2211.5(5)	1232.7(3)	7(4)‡	-	$(2, 3^+)$	1^+
2234.0(5)	794.4(5)	1.9(7)	2237.3(17)	-	-	-	-	-
	1417(1)	2.9(8)		1420.1(17)	13(4)‡	-	-	3^+
2373.6(3)	934.2(4)	4.3(4)	2373.8(4)	(935.3(4))	10(1)	-	6^+	5^+
	1180.1(3)	14.3(6)		1179.4(7)	18(3)‡	(0.60(22))	6^+	5^+
2434.3(2)	1240.7(2)	70(2)	2433.5(3)	1240.6(2)	87(3)	1.20(18)	7^+	5^+
2674.5(3)	1236(1)	1(1)	2672.4(7)	-	-	-	-	-
	1481(1)	2.0(3)		-	-	-	-	-
				1510.1(15)	7(3)	-	4^+	2^+
			2989.4(9)	1796.5(9)	10(1)	-	$(5, 6, 7^+)$	5^+
3014.8(3)	340.4(2)	3.6(8)	3012.7(7)	340.1(3)	5(1)	-	6^+	4^+
	641.2(2)	3.0(3)		(640.8(22))	4(2)‡	-	6^+	6^+
3491.8(3)			3491.4(5)	478.3(11)	2(1)‡	-	7	6^+
	1057.6(2)	12.8(6)		1057.4(5)	10(1)	-	7	7^+
	1118.2(2)	6.0(6)		(1120.3(12))	11(3)‡	-	7	6^+
			3795.7(7)	1362.2(7)	6(2)	-	(7^+)	7^+
3922.0(3)	907.3(3)	6.2(7)	3920.2(5)	907.6(5)	12(2)	1.24(76)	8^+	6^+
	1487.7(3)	13.8(7)		1486.9(5)	22(3)	-	8^+	7^+
4657.8(4)	1166.0(3)	8.5(4)	4656.4(9)	1165.5(7)	17(2)	0.93(29)	8	7
4789.1(3)	867.1(2)	4.0(3)	4789.2(7)	(866.7(10))	11(2)	-	9^+	8^+
	2354.8(5)	15.3(11)		2355.7(6)	30(2)	-	9^+	7^+
4945.2(4)	1023.1(2)	9.0(6)	4943.2(7)	1023.0(5)	13(2)	-	$9^+, 10^+$	8^+
5735.0(4)	789.5(6)	1.2(7)	5735.0(7)	-	-	-	-	-
	945.9(2)	18.0(7)		945.8(3)	35(2)	1.09(26)	11^+	9^+
6842.3(5)	1107.3(3)	6.3(8)	6841.5(8)	1106.5(4)	28(2)	1.72(61)	13^+	11^+
			8587.7(11)	1746.2(8)	18(2)	-	(15^+)	13^+
			9977.4(15)	1389.7(9)	11(6)‡	-	(17^+)	(15^+)

Table 6.1 Summary of results obtained in the current work. Energy levels newly observed in the current study are shown in bold. The excitation energies of the 571 and 817 keV levels are replaced by stars as Doppler effects caused by the isomeric 3^+ state at 817 keV prevent precise energy measurements for the 571 and 246 keV transitions in the current work. Values of the relative intensities, I_{rel}, of the 571 and 246 keV transitions, indicated by daggers (†), are estimated from the values obtained in the Rudolph work. Transitions where values of I_{rel} could not be obtained in singles spectra and were estimated using coincidence spectra are indicated by double daggers (‡).

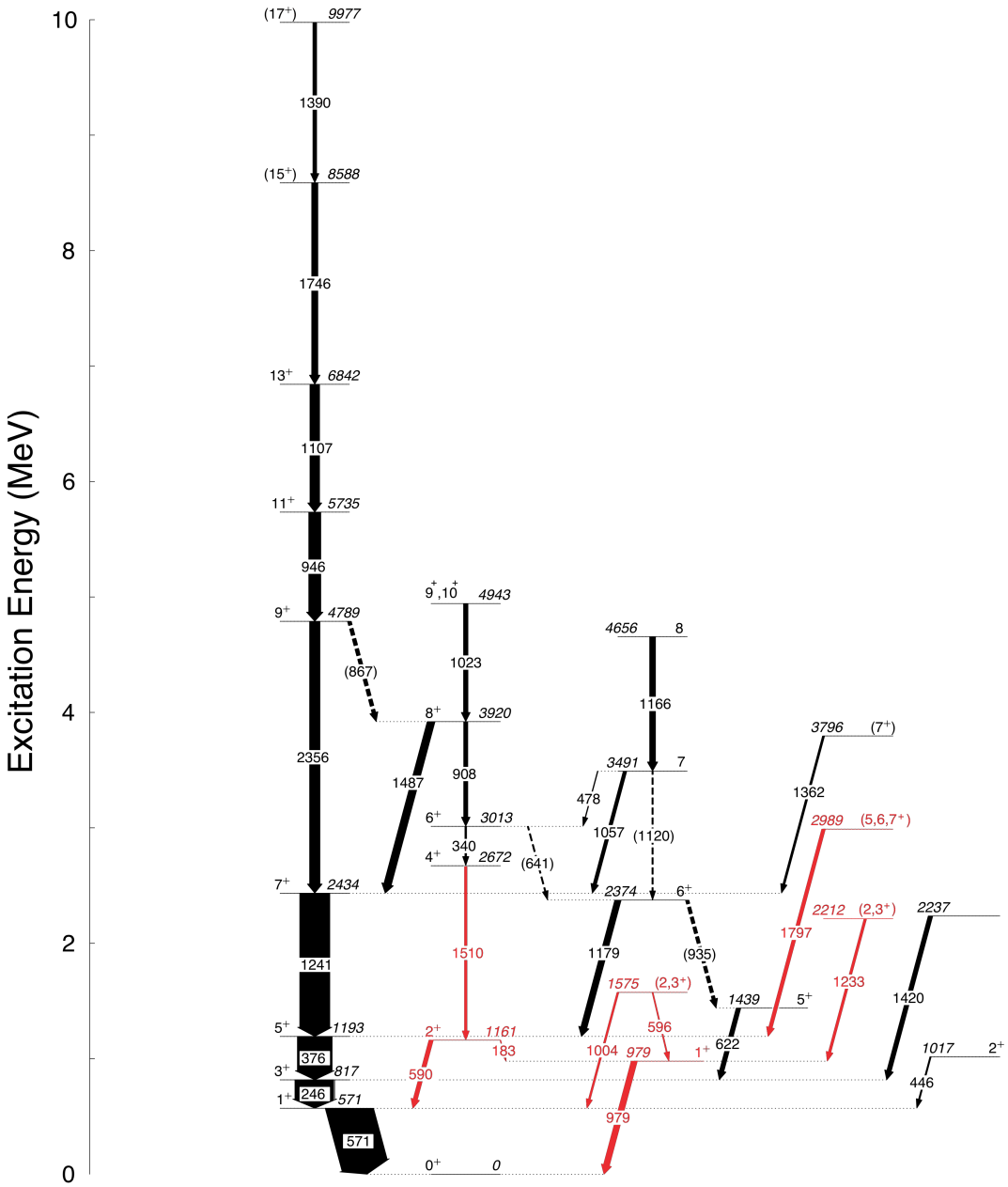

Figure 6.1 ^{62}Ga level scheme obtained in present study, made using the RadWare software package 'gls'. The width of the arrows represents the relative intensities of the transitions. Levels and transitions up to an excitation energy of 3 MeV newly observed in the current study are shown in red.

Relative intensities, I_{rel}, for transitions in cases where peak intensities could be obtained in singles γ-ray spectra are shown in Table 6.1. Estimates for relative intensities obtained for transitions observed in coincidence spectra are indicated by double-daggers (‡). The I_{rel} values are normalised with respect to the 376 keV transition, as it is the most intense transition unaffected by the isomeric 3^+ state. It was not possible to obtain precise measurements of relative intensities for the 246 and 571 keV transitions, which are affected by the isomer, as the efficiency of Gammasphere drops very rapidly for γ decays occurring > 3 cm from the target causing a loss of intensity. The values of I_{rel} listed in Table 6.1 for the 246 and 571 keV transitions, indicated by daggers (†), have therefore been estimated using relative intensities measured in the work by Rudolph.

Information regarding the anisotropy of several of the γ-ray transitions is also shown in Table 6.1. Values of $R_{32:90}$ are given by the ratio of peak intensities in the summed singles spectrum for detectors at small angles with respect to the beam direction, versus peak intensities in the summed singles spectrum for detectors at 90° with respect to the beam direction. A total of 20 detectors at angles of between 17° and 37° (with an average angle of 32°) were used, and 4 detectors at 90°. The ratio allows a clear distinction to be made between γ-ray transitions with $\Delta I = \pm 1$ and $\Delta I = \pm 2$, where ΔI is the difference between the spin of the initial state, J_i, and the spin of the final state, J_f, involved in the decay. Reference values of $R_{32:90} = 1.15(3)$ and $R_{32:90} = 0.72(4)$ were obtained for the known $\Delta I = \pm 2$ transition at 954 keV in ^{62}Zn and the known $\Delta I = \pm 1$ transition at 1197 keV in ^{62}Zn, respectively. A reference value of $R_{32:90} = 1.09(5)$ was obtained for the known $\Delta I = 0$ transition at 1161 keV in ^{58}Ni.

The last two columns in Table 6.1 indicate the spin-parity assignments of the initial and final states involved in the γ decay, denoted by J_i^π and J_f^π, respectively. The values of $R_{32:90}$ obtained in the current study were used to indicate spin assignments for states, but other possible assignments could not be ruled out because of uncertainties associated with the low statistics. Spin-parity assignments are therefore based on anisotropy values and branching information obtained in the present work, information reported in the study by Rudolph *et al.* and the general assumption that states at increasing excitation energy have increasing spin. Full discussions of the justification of spin-parity assignments for each level will be given in the following Sections.

The β-decay half-lives, $\tau_{1/2}$, associated with the γ-ray transitions listed in Table 6.1 are presented in Table A.1 in Appendix A. A value of $\tau_{1/2} = 116.5(13)$

ms for ^{62}Ga was determined in the current study. All newly observed transitions were found to be associated with half-lives consistent with ^{62}Ga, other than transitions where values of $\tau_{1/2}$ could not be obtained due to insufficient statistics.

The spectrum of γ rays measured by the Gammasphere in coincidence with recoiling reaction products that were implanted into the DSSD, shown in Figure 6.2a), is dominated by transitions from long-lived (or stable) contaminant nuclei. The main contaminant peaks are indicated by dashed red lines. The contaminant transitions at 954 and 1232 keV are the very strong $2^+ \rightarrow 0^+$ and $4^+ \rightarrow 2^+$ transitions in ^{62}Zn, respectively. The transition at 1005 keV is the strong $4^+ \rightarrow 2^+$ transition in ^{58}Ni. ^{62}Zn has a $\sim$9 hour half-life and ^{58}Ni is stable. Peaks originating from ^{58}Ni are broad as Doppler corrections are applied for nuclei with mass A = 62 and not A = 58.

Spectra containing γ-ray transitions originating from short-lived ($\tau_{1/2} \sim 100$ ms) nuclei were obtained by only accepting γ rays measured in coincidence with recoiling reaction products that were subsequently correlated with decays in the DSSD within 400 ms of implantation. A full description of the implant-decay correlation method is provided in Section 5.3. The resulting short-lived spectrum for 2NN correlations is shown in Figure 6.2c). Strong transitions at 246, 376 and 571 keV originating from the short-lived nucleus ^{62}Ga are indicated by blue dashed lines. A 'background' spectrum, containing the contribution from long-lived (or stable) contaminant species that are randomly correlated, can be obtained by accepting γ rays measured in coincidence with reaction products that were subsequently correlated with decays between 1 s and 1.4 s of implantation. The resulting background spectrum for 2NN correlations is shown in Figure 6.2b).

6.1 Singles γ-ray spectra

A powerful consequence of the nature of the new system developed at Argonne is the ability to produce sufficiently clean γ-ray spectra without the requirement of γ-ray coincidences. This inherent property has allowed transitions in the N = Z nucleus ^{62}Ga that are not strongly coincident with yrast transitions to be observed for the first time. The γ-ray transitions observed in the singles spectra obtained in the current work are presented in this Section. Figure 6.3 shows the 'clean' singles γ-ray spectrum for short-lived isotopes, which is the resultant spectrum when the background spectrum shown in Figure 6.2b) is subtracted from the 'short-lived'

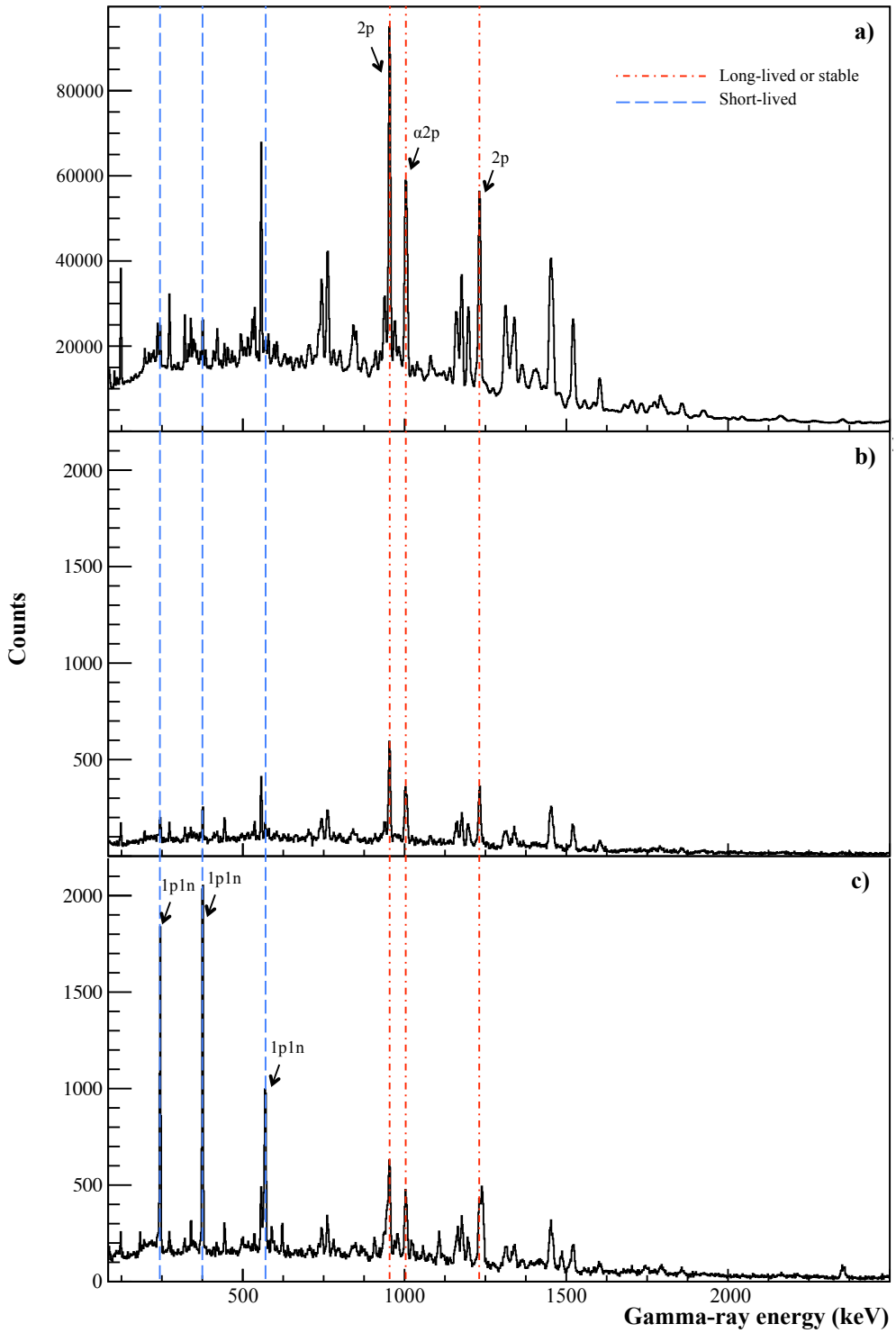

Figure 6.2 Prompt γ rays measured by the Gammasphere in coincidence with recoils that were: a) implanted into the DSSD, b) implanted into the DSSD and correlated with a decay between 1 s and 1.4 s of implantation, c) implanted into the DSSD and correlated with a decay within 400 ms of implantation. Main contaminant peaks from nuclei produced in the 2p and α2p reaction channels are indicated by dashed red lines. Strong transitions emitted from ^{62}Ga nuclei, produced in the 1p1n evaporation channel, are indicated by dashed blue lines. See text for details.

spectrum shown in Figure 6.2c). The singles spectrum is extremely clean, with no peaks originating from contaminants; all visible peaks are attributed to ^{62}Ga. An increase in the yield of ^{62}Ga nuclei in the full experiment compared with the test experiment resulted in the observation of many more transitions, as can be seen by comparing Figures 4.12b) and 6.3. Transitions in Figure 6.3 at $\sim$ 246, 375.7(1), $\sim$ 571, 945.8(3), 1106.5(4), 1240.6(2) and 2355.7(6) keV have also been observed in all previous in-beam studies of ^{62}Ga [31, 42, 43]. It should be noted that precise energy measurements for the 246 and 571 keV transition are not possible in the current work due to the isomeric nature of the 817 keV state.

Figure 6.4a) shows the low energy portion of the singles spectrum presented in Figure 6.3. Transitions at 340.1(3) and 621.9(2) keV are labelled, in agreement with transitions observed at 340.4(2) and 622.3(1) keV in the study by Rudolph *et al.* Three newly observed transitions at 182.8(1), 589.5(3) and 595.9(9) keV are also labelled in Figure 6.4a). A detailed view of the 590, 596 and 622 keV peaks is presented in the inset.

A higher energy singles spectrum is shown in Figure 6.4b). It was found that correlations incorporating two nearest neighbours produced significantly increased levels of background between 800 and 1300 keV compared with correlations incorporating a single neighbouring pixel, as the concentration of transitions from contaminant nuclei is higher in this energy region. Although peaks originating from long-lived contaminants can be removed by carrying out a background subtraction, the effect of subtracting stronger peaks when using 2NN correlations compared with 1NN correlations results in larger fluctuations in the subtracted spectrum. Transitions in Figure 6.4b) at 946, 1107 and 1241 keV are labelled. Additional transitions at 907.6(5), 1023.0(5), 1057.4(5) and 1165.5(7) keV are indicated, in agreement with transitions observed at 907.3(3), 1023.1(2), 1057.6(2) and 1166.0(3) keV in the Rudolph study. Transitions in Figure 6.4b) at 1004.4(11) and 978.8(4) keV are newly observed in the current work.

There is an apparent increase in peak width for the peak at $\sim$ 1180 keV compared with neighbouring transitions, indicating more than one transition at similar energy. However, it has not been possible to disentangle the $\sim$ 1180 keV peak into two or more distinct transitions as the $\sim$ 1180 keV coincidence spectrum is heavily contaminated by a strong transition at 1177 keV in ^{62}Zn. The energy for the 1179.4(7) keV transition was therefore taken from the 376 keV coincidence spectrum, shown in Figure 6.18, which is in agreement with the energy of a transition at 1180.1(3) keV reported in the Rudolph study.

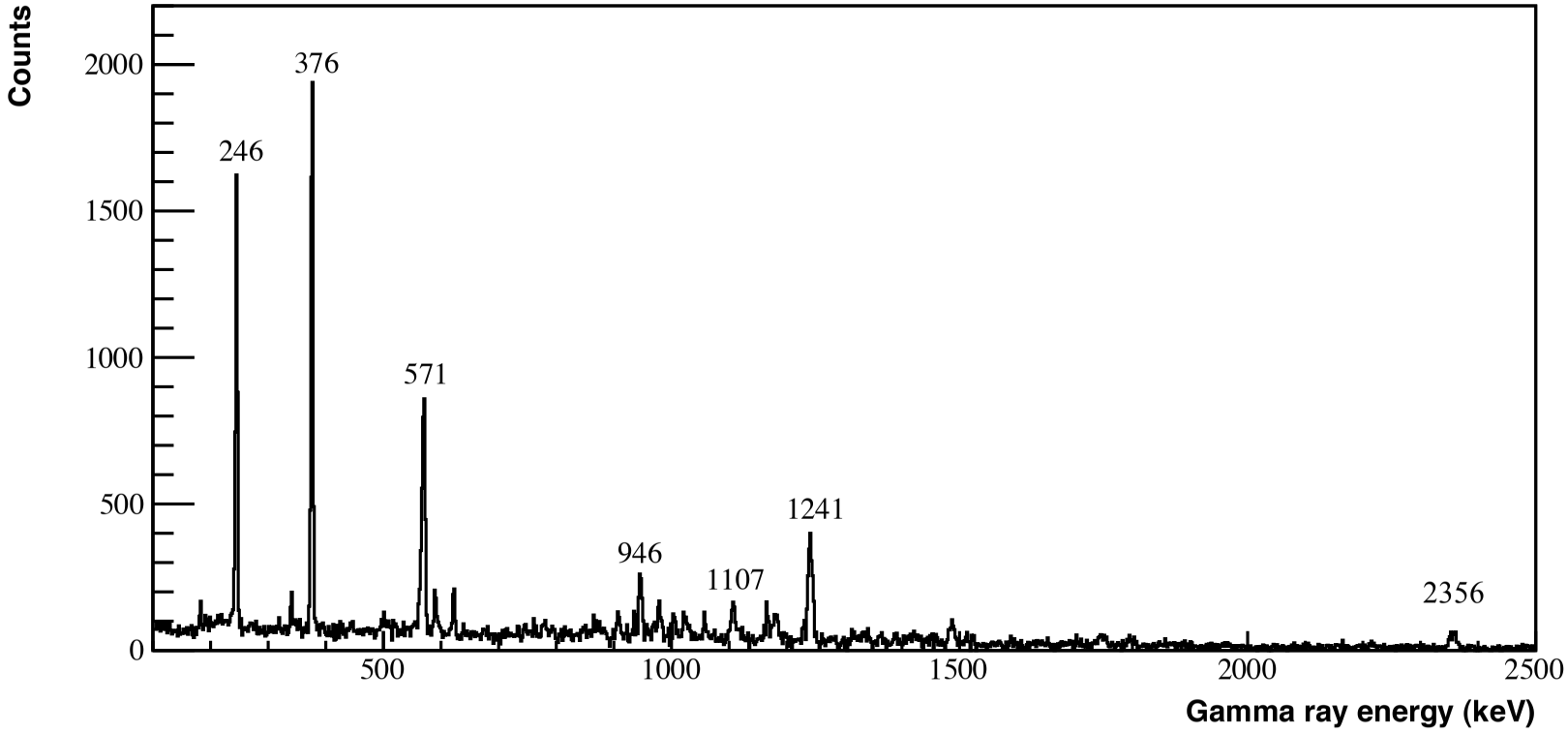

Figure 6.3 Background subtracted singles γ-ray spectrum measured in coincidence with 'short-lived' recoils, using 2NN correlations.

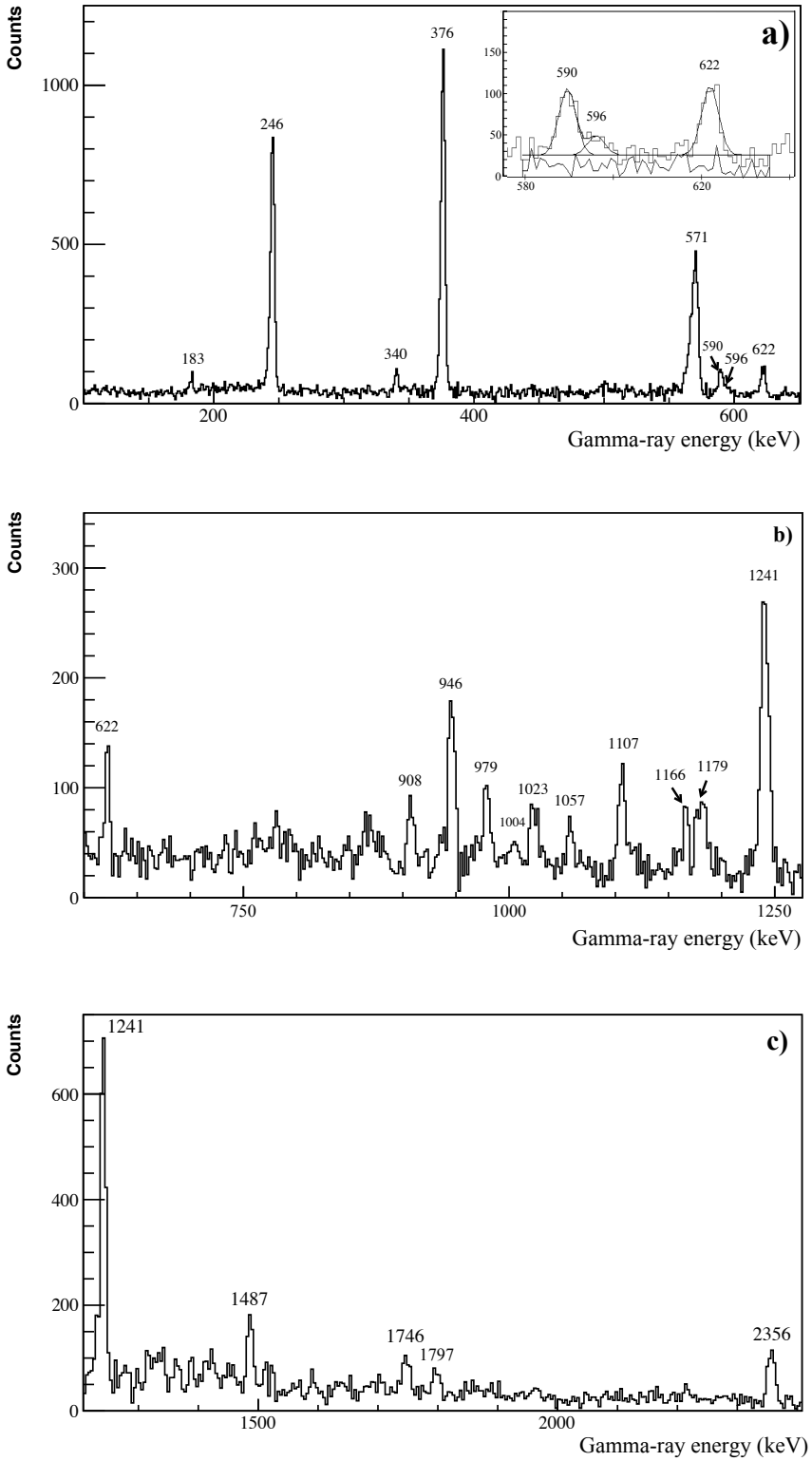

Figure 6.4 a) Background subtracted 'short-lived' singles spectrum made using 2NN correlations. Peak fits for the 590, 596 and 622 keV transitions are shown in the inset, carried out using the RadWare software package 'gf3'. b) Background subtracted 'short-lived' singles spectrum made using 1NN correlations. c) Background subtracted 'short-lived' singles spectrum made using 2NN correlations.

Levels of contamination in the 1300 to 3000 keV energy region are low enough to use two nearest neighbour correlations in the DSSD. The singles spectrum for this energy region is shown in Figure 6.4c). Transitions at 1486.9(5) and 2355.7(6) keV are indicated, in agreement with transitions at 1487.7(3) and 2354.8(5) keV reported in the Rudolph work. A transition at 1746.2(8) keV is also present in Figure 6.4c), which agrees with a 1747 keV γ ray that was previously reported in unpublished thesis work by T. Steinhardt [97]. The peak at 1796.5(9) keV is newly observed in the current study.

6.2 The level structure of the $\mathrm{N} = \mathrm{Z}$ nucleus ^{62}Ga

The following Sections discuss the level structure of ^{62}Ga deduced from the current work. In general, the levels will be discussed in order of increasing excitation energy, except in cases where it is more appropriate to discuss groups of states that form cascades. Yrast levels will be discussed first to provide a strong foundation upon which to build the level scheme, as the yrast band in ^{62}Ga is well established from previous γ-ray studies.

To identify the placement of the γ-ray transitions observed in the singles spectra within a level scheme, a γ-ray coincidence matrix, as described in Section 5.4, was constructed for γ rays measured by the Gammasphere in coincidence with recoils that were correlated within 2 neighbouring pixels in the DSSD with a β particle within 400 ms of implantation. A similar matrix for correlations made using 1 neighbouring pixel was also constructed. Coincidence spectra for 'background' events using projections of energy regions containing no γ-ray transitions close to the region of interest were subtracted from the true coincidence spectra. A parallel coincidence analysis was carried out using the RadWare software package 'escl8r' [96] to confirm all γ-ray coincidences presented in the following Sections. All coincidences were verified using 'backwards' gates. For example, a real coincidence between two γ rays with energies E_1 and E_2 requires the presence of E_1 in the spectrum gated on E_2 and E_2 in the spectrum gated on E_1.

6.2.1 Yrast levels

Transitions at 1107, 946, 2356, 1241, 376, 246 and 571 keV were observed in all previous in-beam studies of ^{62}Ga, and attributed to transitions originating from

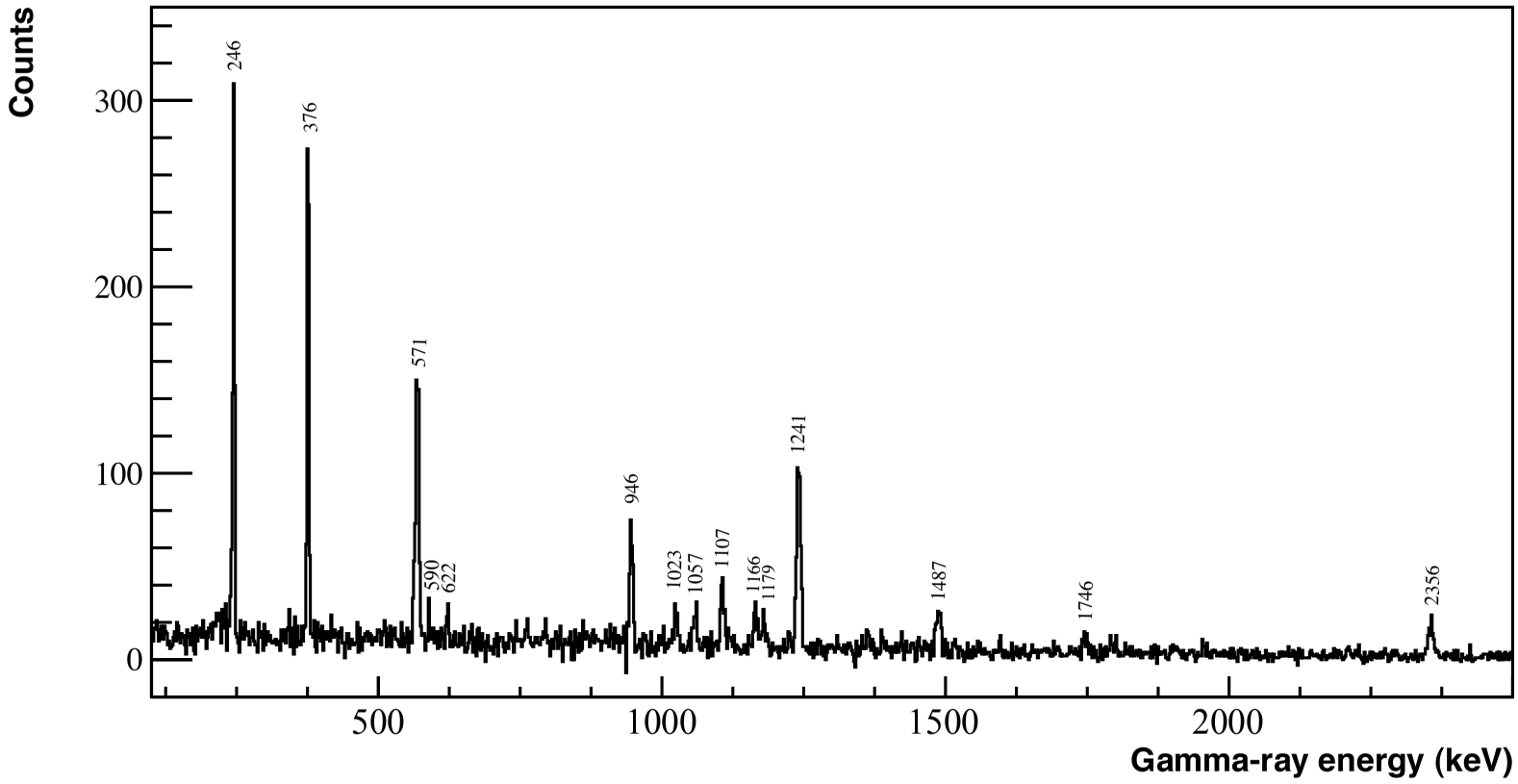

Figure 6.5 Yrast coincidence spectrum: sum of the coincidence spectra gated on the 571, 246, 376, 1241 and 2356 keV transitions, using 2NN correlations.

odd-spin yrast levels in ^{62}Ga in studies by Vincent *et al.* and Rudolph *et al.* The 1107-946-2356-1241-376-246-571 keV ordering of the odd-spin yrast cascade observed in the current work, deduced through analysis of relative intensities of yrast transitions in γ-ray coincidence spectra, is in agreement with the level schemes proposed in all previous studies.

The relative intensities measured for transitions belonging to the 1107-946-2356-1241-376 keV yrast cascade are given in Table 6.1. Although differences in relative intensity between this study and a previous study by Rudolph *et al.* [31] are expected due to a slightly lower excitation energy in the Rudolph experiment compared with this work, the relative values of 6.3(8)-18.0(7)-15.3(11)-70(2)-100(3) % reported in the Rudolph work are broadly consistent with the values of 28(2)-35(2)-30(2)-87(3)-100(2) % measured in the current study. In the present work, an anisotropy ratio, $R_{32:90}$, of 1.21(11) was obtained for the 376 keV transition that, compared with the reference value for $\Delta I = \pm 2$ of 1.15(3), confirms the $5^+ \rightarrow 3^+$ nature of the 376 keV transition. Values of $R_{32:90}$ of 1.20(18) and 1.09(26) were obtained for the 1241 and 946 keV transitions, respectively, that are consistent with the $\Delta I = \pm 2$ character reported in previous work for both transitions [31]. A ratio of 1.72(61) for the 1107 keV transition allows a J^π of 13^+ to be assigned to the 6841.5(8) keV state.

The sum of the 571, 246, 376, 1241 and 2356 keV background subtracted coincidence spectra made using the 2NN coincidence matrix is shown in Figure 6.5. Coincidences between yrast transitions and transitions at 622, 1023, 1057, 1166, 1179 and 1487 keV are clearly visible in Figure 6.5, in agreement with the level scheme constructed by Rudolph *et al.* The newly observed transitions at 590 and 1746 keV are also apparent in the yrast coincidence spectrum, indicating that these transition feed (or are fed by) yrast states. The background subtracted coincidence spectrum for the 2356 keV $9^+ \rightarrow 7^+$ yrast transition is shown in Figure 6.6a). The 246, 376, 571, 946, 1107 and 1241 keV yrast transitions are present, as expected. A 2356-1746 keV coincidence is also evident.

The background subtracted coincidence spectrum for the 1746 keV transition is shown in Figure 6.6b), with a high energy portion shown in the inset. Strong coincidences with yrast transitions at 246, 376, 571, 946, 1107, 1241 and 2356 keV, with a lack of any strong non-yrast coincidences, indicates that the 1746.2(8) keV transition is also yrast. The very strong 1746-1107 keV coincidence (after efficiency corrections) indicates that the 1746 keV transition originates from an yrast state at 8587.7(11) keV, directly feeding the 6841.5(8) keV 13^+ state.

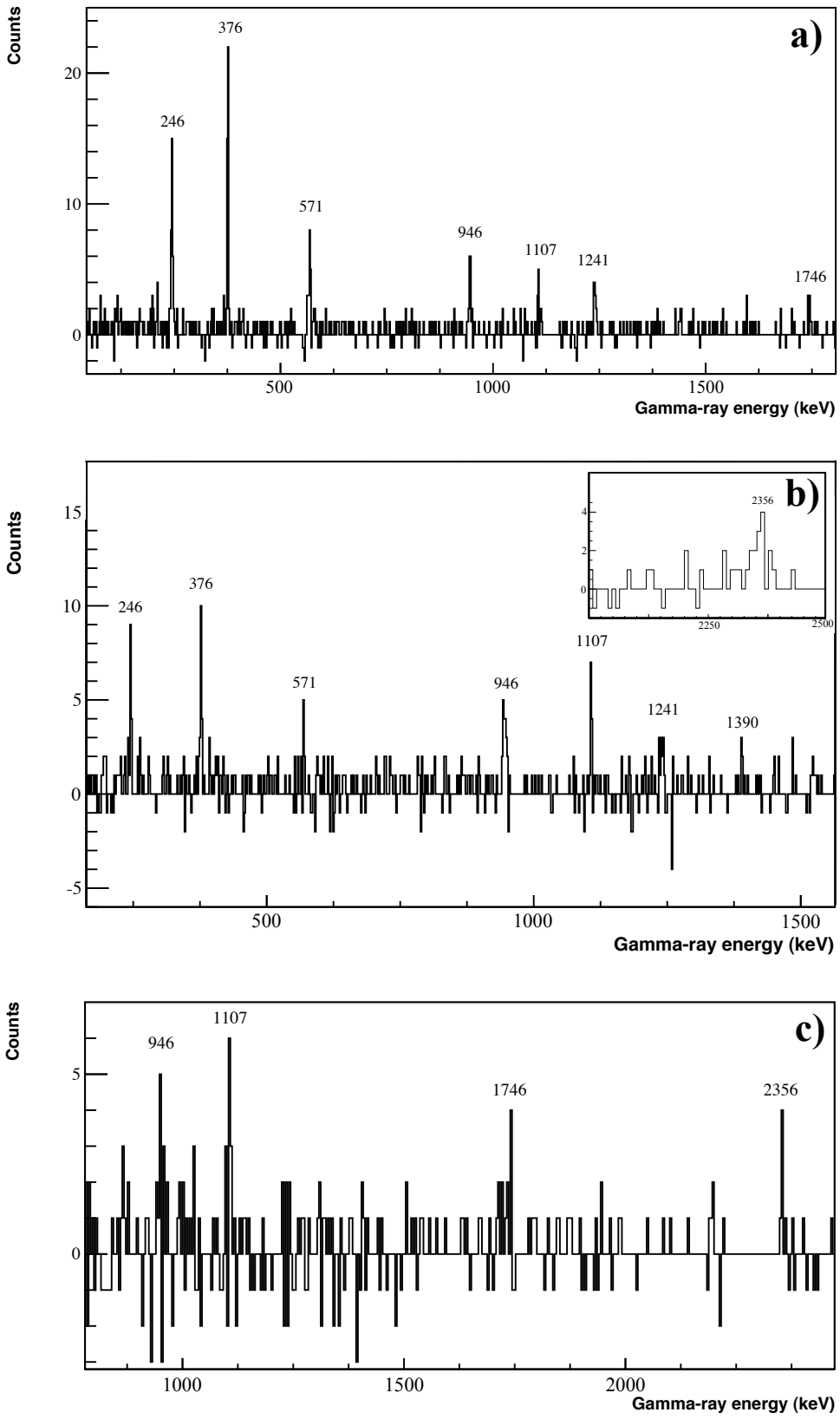

Figure 6.6 Background subtracted coincidence γ-ray spectrum for: a) the 2356 keV transition, using 1NN correlations, b) the 1746 keV transition, using 1NN correlations, c) the 1390 keV transition, using 2NN correlations

The observation in the current study of an yrast level at 8588 keV is in agreement with an extension to the yrast band by a 1747 keV transition reported in thesis work by T. Steinhardt [97]. The stretched E2 nature of the 1747 keV transition reported in the Steinhardt work allows a tentative J^{π} of 15^{+} to be assigned to the state at 8588 keV. A further extension of the yrast band via a 1387 keV transition was also reported in the thesis work by T. Steinhardt [97]. A transition at 1389.7(9) keV in coincidence with the 1746 keV transition is indeed visible in Figure 6.6b). The strong presence of the 1746 keV transition in the coincidence spectrum for the 1390 keV transition, shown in Figure 6.6c), indicates a state at 9977.4(15) keV that feeds the (15^{+}) state at 8588 keV. Similarly to the 1747 keV transition, the 1387 keV transition observed in the Steinhardt work was reported to be a stretched E2, allowing a tentative 17^{+} assignment to be made for the 9977 keV state.

6.2.2 Newly observed levels at 979 and 1161 keV

In an experiment designed to test the new experimental system at Argonne, described in full detail in Section 4.7.2, an unknown transition at 980 keV was observed. As the nature of the new system allows measurements of the β-decay half-life associated with γ-ray transitions to be made, it was deduced that the 980 keV transition originated from either ^{62}Ga or ^{62}Ge, which both have β-decay half-lives of the order of 100 ms. However, with insufficient statistics to carry out a γ-ray coincidence analysis, the origin of the 980 keV remained a mystery. The increased level of statistics obtained in the more extensive experiment described in this Chapter, however, has allowed a significant extension to the low-lying level scheme of ^{62}Ga, and the origin of the 980 keV transition to be established.

The 979 keV transition is clearly visible in the singles spectrum shown in Figure 6.4b). The coincidence spectra for the 979 keV transition are shown in Figure 6.7. No yrast transitions are present in Figure 6.7, and the 979 keV transition does not appear in the yrast coincidence spectrum shown in Figure 6.5. It can be deduced, therefore, that the 979 keV transition does not feed, nor is it fed by the yrast band. A pronounced peak at 183 keV is apparent in Figure 6.7. This indicates a strong coincidence between the 979 keV transition and a transition at 183 keV. The 183 keV transition, not observed in previous studies, is clearly visible in the singles spectrum shown in Figure 6.4a). As the 183 keV γ ray does not appear in coincidence with any yrast transitions, it can be inferred that the

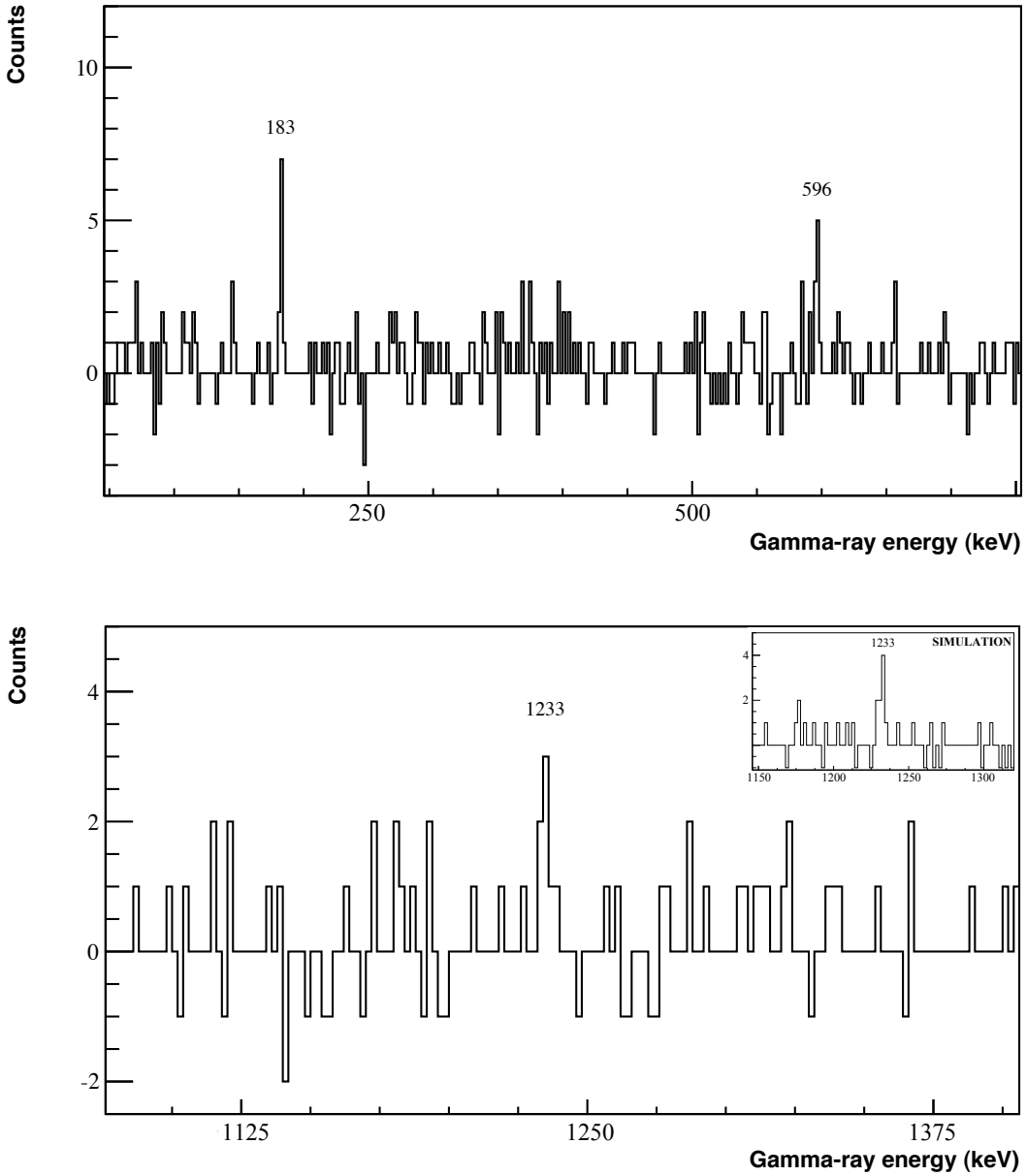

Figure 6.7 Background subtracted coincidence γ-ray spectra for the 979 keV transition, using 1NN correlations. The inset of the lower panel shows a simulated coincidence spectrum for comparison with the 1233 keV peak. See Section 6.2.7 for full details.

183 keV transition feeds the 979 keV transition directly. A reversed ordering of the 183-979 keV cascade can be ruled out due to intensity arguments, as the relative intensities of the 183 and 979 keV transitions are measured to be 2(1) % and 17(2) %, respectively.

The observation that the 979 keV transition is not in coincidence with any yrast transitions provides a strong indication that the 979 keV transition feeds the ground state directly from a newly observed state at 978.8(4) keV. In particular, all states identified in the Rudolph study feed through the $1^+ \rightarrow 0^+$ transition at 571 keV, yet no 571 keV transition appears in the 979 keV coincidence spectrum. The deduction that the 979 keV transition feeds the ground state is confirmed through the observation of a second branch from the state at 1161 keV that feeds the 979 keV via the 183 keV transition, as will be discussed in detail later in this Section. As the 979 keV transition feeds the 0^+ ground state directly, the spin of the 979 keV state is limited to a value less than 3 as transitions with $\Delta I > 2$ are inhibited and would not be observed with the level of statistics attained in the present work. A value of $R_{32:90} = 0.77(25)$ was measured for the 979 keV transition. This, compared with the reference value of $R_{32:90} = 0.72(4)$ for $\Delta I = \pm 1$, strongly indicates that the 979 keV transition has $\Delta I = \pm 1$ character. A spin assignment of 1 is therefore strongly favoured for the 979 keV state.

Although no γ-ray transition at 979 keV has been reported in any previous in-beam γ-ray studies, a transition at 978 keV was identified following the β decay of ^{62}Ge in a Scientific Report by Grodner *et al.* [73], described in Section 3.2. A full discussion of the implications of this observation will be given in Section 6.3. However, at this stage it should be noted that the observation of the 978 keV transition in the Grodner study, if it is assumed that this transition feeds the ground state from the newly observed level at 979 keV, is consistent with a 1^+ assignment for the 979 keV level, as allowed Gamow-Teller decays of ^{62}Ge populate 1^+ states in ^{62}Ga directly.

An unknown transition at 590 keV was observed in singles data from the test experiment, shown in Figure 4.12b), and again in the in-depth experiment, shown in Figure 6.4a). Although no information regarding the origin of the 590 keV transition could be obtained in the test experiment, the increased level of statistics in the second experiment allowed a γ-ray coincidence analysis to be carried out and the 590 keV transition to be attributed to originating from a newly observed level in ^{62}Ga at 1161 keV.

In the coincidence spectrum for the 590 keV transition, shown in Figure 6.8, a strong coincidence between the newly observed 590 keV transition and the $1^+ \rightarrow 0^+$ yrast transition at 571 keV can be seen. The lack of peaks at 376 and/or 246 keV in Figure 6.8 indicates that the 590 keV transition directly feeds the 571 keV state. Conversely, if the 590 keV transition were to feed a higher-lying yrast state, strong coincidences with the 376 and/or 246 keV transitions would be apparent in Figure 6.8. If the 590 keV transition were to feed a non-yrast state above the 571 keV state, a linking transition to the 571 keV state would be clearly evident in Figure 6.8 with similar intensity to the peak at 571 keV. However, only peaks at 340 and 908 keV are present, both with significantly lower intensity than the 571 keV transition.

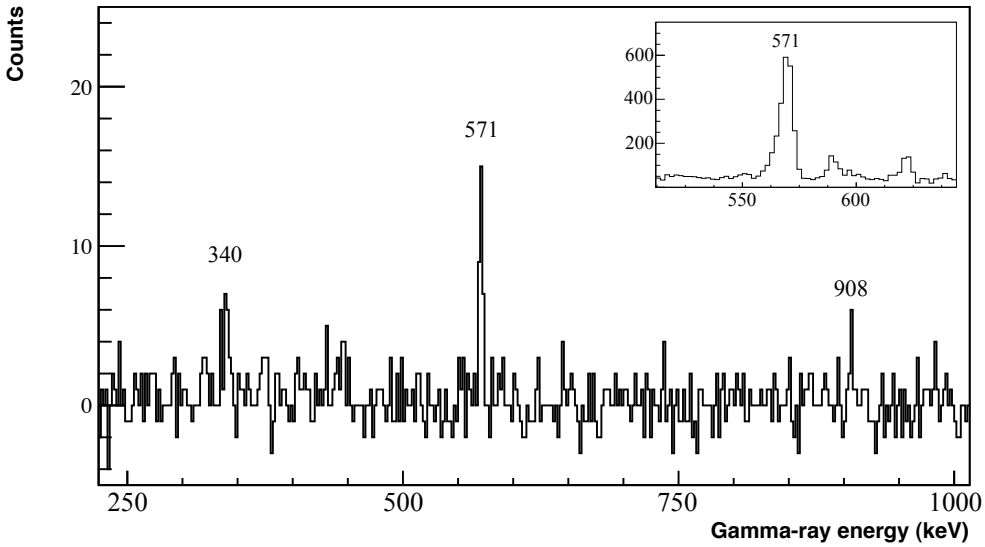

Figure 6.8 Background subtracted coincidence γ-ray spectrum for the 590 keV transition, using 2NN correlations. The inset shows the 571 keV transition in the singles spectrum.

The direct feeding of the 571 keV state by the 590 keV transition is also strongly supported by consideration of the line shape of the 571 keV peak in the 590 keV coincidence spectrum. In the singles spectrum shown in the inset of Figure 6.8, and in all coincidence spectra for transitions that feed the yrast band either at, or above, the 3^+ state at 817 keV, the 571 keV peak has a very distinctive line shape consisting of an increase in peak width and low energy tail due to Doppler effects. This line shape is characteristic of transitions fed by isomeric states. The peak at 571 keV in the 590 keV coincidence spectrum shown in Figure 6.8 does not exhibit this distinctive shape, signifying that the 571 keV γ rays are not fed by the 3^+ isomeric state, but by a non-yrast state directly. It is possible

to measure the energy of the 571 keV transition using the 590 keV coincidence spectrum shown in Figure 6.8 as no Doppler effects due to the isomeric 3^+ state are present. The measured value of 570.8(3) keV is in agreement with the value of 571.2(1) keV reported in the Rudolph study.

The proximity of the summed energies of the 183-979 keV and 590-571 keV cascades, with a low level density of low-lying states, implies that a level at 1161.0(3) keV decays via both a 183 keV transition to the newly observed level at 979 keV, and a 590 keV transition to the 1^+ yrast state at 571 keV. This confirms the presence of the 979 keV level and the deduction that the 979 keV transition feeds the ground state directly.

A value of $R_{32:90} = 0.72(21)$ was obtained for the 590 keV transition. This, in comparison with the $\Delta I = \pm 1$ reference value of 0.72(4), strongly indicates that the 590 keV transition has $\Delta I = \pm 1$ character. As the 590 keV transition feeds the 1^+ state at 571 keV, this suggests that the 1161 keV state has a spin assignment of 2. The observation of direct feeding of the 1161 keV level from a higher-lying 4^+ state at 2672 keV suggests a 2^+ assignment for the 1161 keV state, which will be discussed in detail in Section 6.2.3. The 2^+ assignment for the 1161 keV state is consistent with the observed branch from the 1161 keV level to the 979 keV level, which has a strongly favoured 1^+ assignment. A value of $R_{32:90} = 0.76(46)$ was obtained for the 183 keV transition that, despite a large error, is consistent with a $\Delta I = \pm 1$ transition feeding the 979 keV state.

6.2.3 Levels at 2672, 3013, 3920 and 4943 keV

In the present study, transitions at 907.6(5) and 340.1(3) keV were observed in the singles spectra shown in Figures 6.4b) and a), respectively. The coincidence spectrum for the 340 keV transition is shown in Figure 6.9. The very strong presence of the 908 keV transition in Figure 6.9 suggests that the 908 keV transition directly feeds the 340 keV transition. Peaks of similar intensity at 590 and 571 keV can be seen in the 340 keV coincidence spectrum, as well as a strong 1510.1(15) keV peak. The 340 and 908 keV transitions both appear in the 590 keV coincidence spectrum, shown in Figure 6.8, allowing a 908-340-1510-590-571 keV cascade to be established. The cascade originates from a level at 3920.2(5) keV, and feeds a state at 3012.7(7) keV via a 908 keV transition. The 3013 keV state then de-excites via a 340 keV transition to a state at 2672.4(7) keV. This is in agreement with a 907.3(3)-340.4(2) keV cascade reported to originate from

a state at 3922.0(3) keV in the study by Rudolph *et al.* The 1510 keV transition links the level at 2672 keV, which has been previously observed, with the newly observed level at 1161 keV.

In addition to the 908 keV transition, a transition at 1486.9(5) keV was found to originate from the 3920 keV state in both the current work and in the work by Rudolph *et al.* The coincidence spectrum for the 1487 keV transition obtained in the present study is shown in Figure 6.10. The strong coincidence between the 1487 and 1241 keV transitions, with no higher-lying yrast transition or any strong non-yrast transitions present in Figure 6.10, indicates that the 1487 keV transition feeds the 7^+ state at 2434 keV directly from the 3920 keV level.

Low intensity peaks at 478 and 622 keV can be seen in the 340 keV coincidence spectrum shown in Figure 6.9. The 622 keV transition originates from a state at 1439 keV, which will be discussed in Section 6.2.5. The observation of the 622 keV transition in Figure 6.9 suggests that the state at 2672 keV, which is fed by the 340 keV transition, feeds the level at 1439 keV, either directly or via another state. A tentative transition at 1236(1) keV feeding the 1439 keV level from the 2672 keV level was reported by Rudolph *et al.* However, no transitions linking the 2672 and 1439 keV states have been observed in the current work. In the Rudolph study, a transition at 1481 keV was found to originate from the 2672 keV state that feeds the yrast 5^+ state at 1193 keV. No 1481 keV transition was observed in the present work. The 478 keV transition indicated in Figure 6.9 feeds the level at 3013 keV from a higher-lying state at 3491 keV, which will be discussed in Section 6.2.11.

A 641 keV transition to a state at 2374 keV was found to de-populate the state at 3013 keV in the Rudolph work. Although a transition at 641 keV was not observed in the singles spectrum in the current work, a weak line at 640.8(22) keV was observed in the 376 keV coincidence spectrum, and attributed to originating from the state at 3013 keV. The 1023.0(5) keV transition, which is visible in the singles spectrum shown in Figure 6.4b), can be seen with low intensity in the 1487 keV coincidence spectrum shown in Figure 6.10. This implies a level at 4943.2(7) keV, in agreement with the observation of a level at 4945.2(4) keV that was found to de-excite to the level at 3920 keV in the Rudolph work via a 1023.1(2) keV γ ray.

A low intensity peak at 946 keV is apparent in the 1487 keV coincidence spectrum shown in Figure 6.10. A transition at 867 keV, linking the 9^+ state at 4789 keV to the state at 3920 keV, was reported in the Rudolph study and in the T. Steinhardt

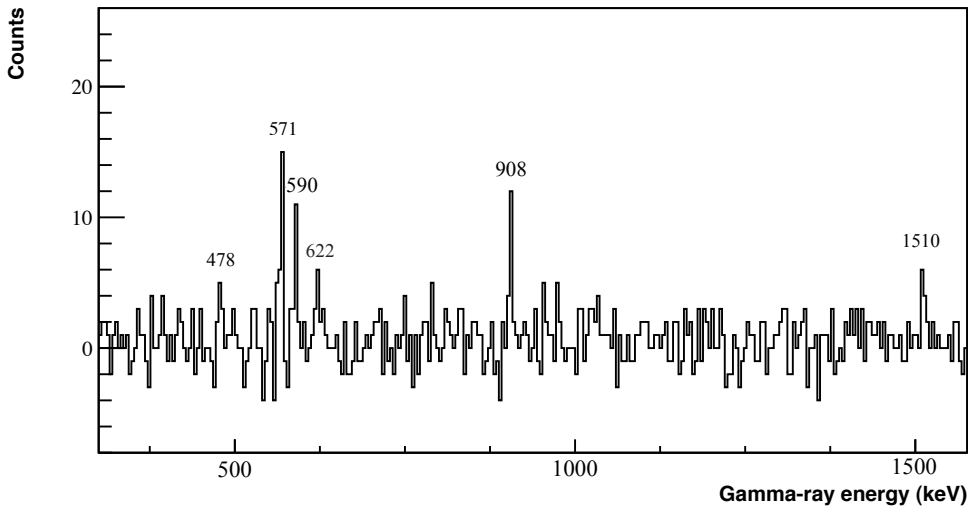

Figure 6.9 Background subtracted coincidence γ-ray spectrum for the 340 keV transition, using 2NN correlations.

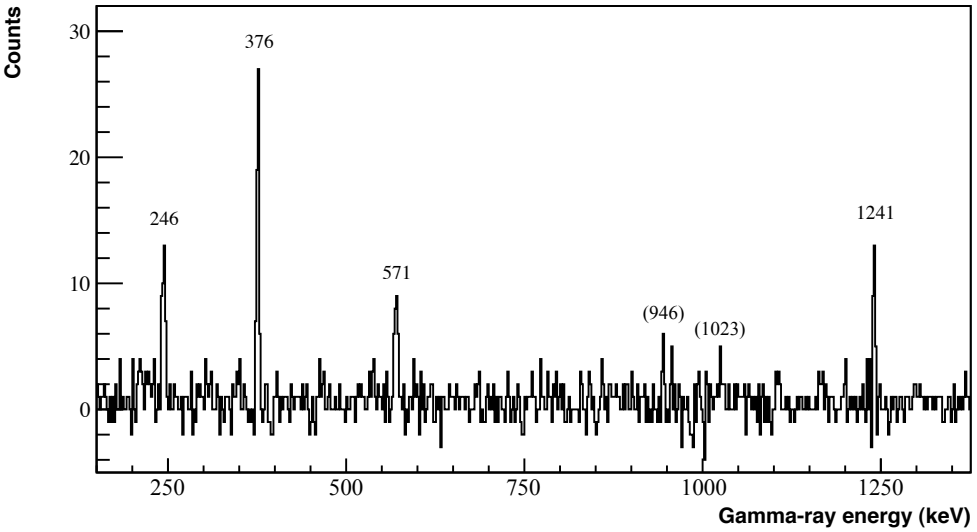

Figure 6.10 Background subtracted coincidence γ-ray spectrum for the 1487 keV transition, using 2NN correlations.

thesis work. A transition at 867 keV is not visible in the 1487 keV coincidence spectrum, but a line at 866.7(10) keV was observed in the singles spectrum, and a weak 1487-946 keV coincidence is suggestive of the 867-1487 keV bypass of the 2356 keV transition, as the 946 keV transition feeds the 9^+ yrast state.

The 3920 keV state, which feeds the yrast 7^+ level at 2434 keV and the 3013 keV level, was given a spin-parity assignment of 8^+ in the Rudolph study. It is also known from the current work that a 908-340-1510 keV cascade links the 8^+ 3920 keV state with the newly observed level at 1161 keV that, as discussed in Section 6.2.2, has a strongly favoured spin assignment of 2 based on anisotropy information for the 590 keV transition. Any spin assignment lower than 2 for the 1161 keV state can be ruled out as only three transitions link the 8^+ state at 3920 keV with the 1161 keV level, and the level of statistics attained in the current work only accommodates the observation of E1, M1 or E2 radiation. With the knowledge that three transitions link the 8^+ 3920 keV level with the J = 2 level at 1161 keV, the only possible spin-parity assignments for the intermediate levels at 3013 keV and 2672 keV are 6^+ and 4^+, respectively. The 1161 keV is therefore assigned as 2^+.

In the Rudolph study, the 2672 keV state was assigned as J = 6, based on anisotropy information for a transition at 1481(1) keV that was observed to feed the 5^+ state at 1193 keV from the 2672 keV state [31]. The J = 6 assignment disagrees with the 4^+ assignment in the current work. However, the anisotropy ratio of 0.62(11) obtained for the 1481 keV transition in the Rudolph study implies $\Delta I = \pm 1$ character, which is also consistent with a J = 4 assignment for the 2672 keV state in addition to a J = 6 assignment. The 2672 keV state is therefore assigned as 4^+. An assignment of 6^+ or 7^+ was given for the 3013 keV state in the Rudolph study, which is consistent with the 6^+ assignment in the current work.

As no anisotropy information was obtained in the present work for the 1023 keV transition, the assignment of 9^+ or 10^+ for the 4943 keV state given in the Rudolph work remains unchanged. An anisotropy ratio of 1.24(76) obtained in the current work for the 908 keV transition has an error too large to allow spin assignments based on this value. No anisotropy information could be obtained for the 340 keV transition in the current work as no excess counts above background levels were observed at this energy in the 90° summed spectrum. Although this meant a measurement of the ratio could not be taken, the lack of counts in the 90° summed spectrum is consistent with a value of $\Delta I = \pm 2$ for the 340 keV transition.

6.2.4 Level at 1017 keV

Isospin symmetry in nuclear structure is a very well-studied phenomenon, in part through detailed spectroscopy of isobaric multiplets, where isospin symmetry-breaking effects are manifested through Coloumb energy differences between isobaric analogue states. Despite the breaking of isospin symmetry, the fundamental property of the symmetry that levels with T = 1 in a member of an isobaric triplet exist in all other members of the triplet must be obeyed. All T = 1 states in the nucleus ^{62}Zn are therefore required to exist in both ^{62}Ga and ^{62}Ge. As the first excited T = 1 2^+ and 4^+ states in ^{62}Zn are known to have excitation energies of 954 and 2186 keV, respectively, the analogue 2^+ and 4^+ states must exist at similar excitation energy in ^{62}Ga. Studies of similar nuclei in the mass region close to A = 62 have shown that energy shifts between isobaric analogue states of this type are typically within tens of keV. Information regarding the feeding between these isobaric analogue states in ^{62}Ga and T = 0 states, as well as the excitation energies of the isobaric analogue states, provide key elements in developing current understanding of isospin effects.

Prior to the 2004 Rudolph study, where candidates states for the 2^+ and 4^+ T = 1 isobaric analogue states to states at 954 keV and 2186 keV in ^{62}Zn were proposed (discussed in Section 3.1), no excited T = 1 states in ^{62}Ga had been reported. Evidence for the candidate 2^+ state came in the form of a 446 keV γ ray that fed the 1^+ state at 571 keV directly from a state at 1017 keV. The 1017 keV level was assigned a spin of 2 from anisotropy information obtained for the 446 keV transition. Predictions of the branching ratios for the T = 1 2^+ state carried out in the Rudolph study indicated that the state would decay via a weak transition to the 1^+ state at 571 keV, and via a strong transition directly to the ground state. The existence of the 1017 keV level and the branch to the 1^+ yrast state have been confirmed in the present work, as will be shown in this Section.

Figure 6.11 shows the background subtracted coincidence spectrum for the 571 keV yrast $1^+ \rightarrow 0^+$ transition. Strong coincidences with the 246 keV and 376 keV transitions can be seen. The higher intensity of the 246 keV transition with respect to the 376 keV transition confirms the 376-246-571 keV ordering of the $5^+ \rightarrow 3^+ \rightarrow 1^+ \rightarrow 0^+$ cascade. A 571-622 keV coincidence is in agreement with the previous observation of a level at 1439 keV that feeds the 3^+ state at 817 keV via a 622 keV transition [31, 43], as will be discussed in Section 6.2.5.

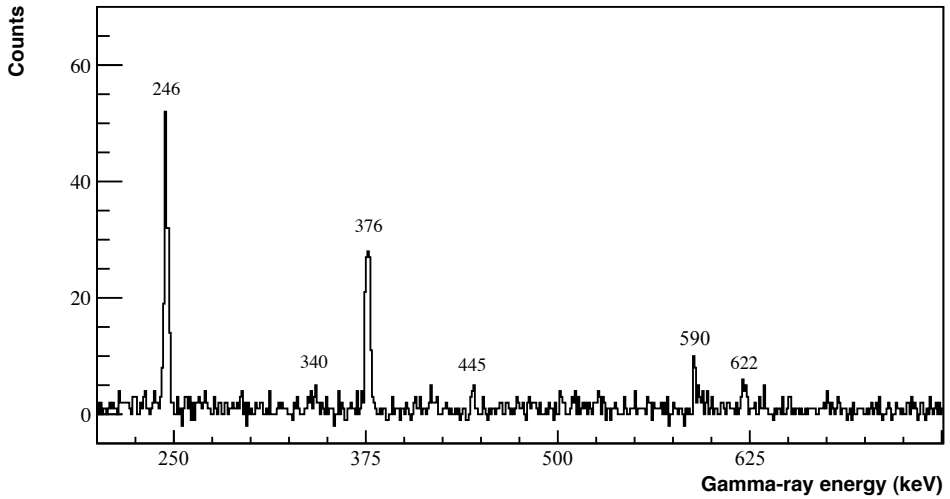

Figure 6.11 Background subtracted coincidence γ-ray spectrum for the 571 keV transition, using 2NN correlations.

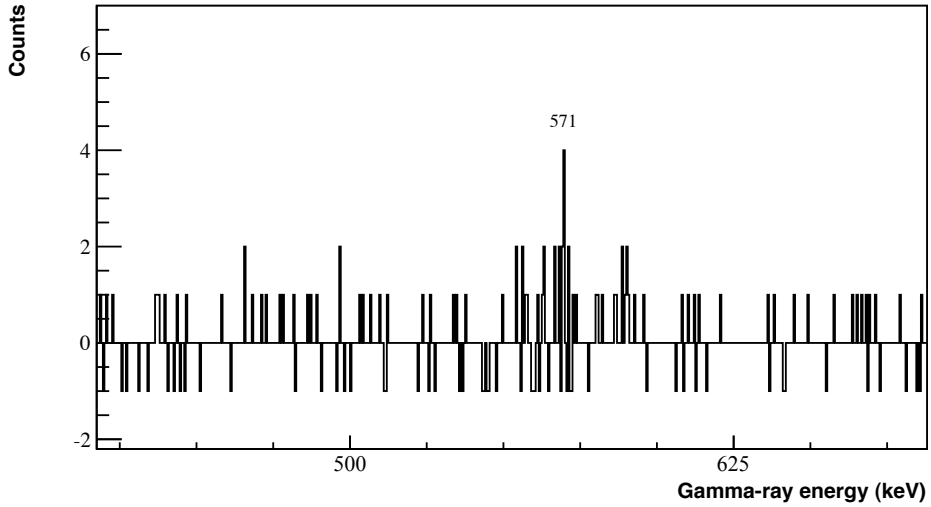

Figure 6.12 Background subtracted coincidence γ-ray spectrum for the 446 keV transition, using 2NN correlations.

A weak peak at 445.9(7) keV is visible in the 571 keV coincidence spectrum shown in Figure 6.11. No known 571-446 keV coincidences exist in any contaminant species produced in this work, and no evidence for coincidences between the 446 keV transition and any other transition has been observed. Further evidence for a 571-446 keV coincidence is given in the background subtracted coincidence spectrum for the 446 keV transition, shown in Figure 6.12. The 571-446 keV coincidence therefore indicates the existence of a state at 1017.1(7) keV that feeds the 571 keV state. The 1017 keV level observed in the current study is in agreement with the state at 1016.7(3) keV observed in the Rudolph work that, as previously discussed, was found to feed the 571 keV 1^+ state via a 445.5(3) keV transition.

A strong branch to the ground state from the T = 1 2^+ state was predicted in the shell model calculation by Rudolph *et al.*, as well as a weak branch to the 571 keV state. The proximity in energy of the 1017 keV state to the 954 keV 2^+ state in ^{62}Zn, the spin 2 assignment given in the Rudolph work, and the observation of the branch to the 1^+ state at 571 keV in both the Rudolph work and the present study support the proposed T = 1 2^+ nature of the 1017 keV state. However, the non-observation of a 1017 keV γ ray in the Rudolph study meant that the state at 1017 keV could only be tentatively assigned as the T = 1 2^+ state. No transition at 1017 keV was observed in the current study. However, in the β-decay study of ^{62}Ge by Grodner *et al.* [73] discussed in Section 3.2, a γ-ray transition at 1017 keV was observed following the β decay of ^{62}Ge, as shown in Figure 3.4. If the 1017 keV transition observed in the ^{62}Ge β-decay study is a transition directly to the ground state from the 1017 keV state, then an explanation as to how a transition from a 2^+ state would be observed following the β decay of ^{62}Ge must be given.

As discussed in Section 3.2, 1^+ states in ^{62}Ga are populated following allowed Gamow-Teller β decays of ^{62}Ge. Non-analogue Fermi decays (Fermi decays that are not superallowed) to excited states in ^{62}Ga can also compete with allowed Gamow-Teller decays if isospin and parity selection rules are obeyed (ΔT = 0 and no parity change). If allowed Gamow-Teller or non-analogue Fermi decays to excited states in ^{62}Ga take place, then subsequent de-excitations occur via γ-ray emission. No γ rays would be observed following superallowed Fermi β decays directly to the ground state of ^{62}Ga. Additionally, γ-ray transitions following first forbidden decays would be greatly inhibited compared with those following allowed decays, and are highly unlikely to appear in Figure 3.4. Therefore,

transitions labelled in Figure 3.4 either originate from 1^+ or T = 1 0^+ states in ^{62}Ga fed directly by allowed Gamow-Teller or allowed Fermi β decays of ^{62}Ge, or from states in ^{62}Ga fed in cascades originating from higher-lying 1^+ or T = 1 0^+ states.

In a recent β-decay study of ^{62}Ga, many γ-ray transitions in ^{62}Zn were observed following non-superallowed β decays [98]. In particular, the 954 keV transition directly to the 0^+ ground state from the first excited 2^+ state was the most intensely observed transition. While not directly populated in the β decay, the 954 keV 2^+ state was found to be fed by several higher-lying low-spin states. Consideration of isospin symmetry indicates that the transitions observed in ^{62}Ga following the β decay of ^{62}Ge should contain the strong transitions from T = 1 states observed in ^{62}Zn following the β decay of ^{62}Ga. Additional transitions fed by T = 0 states populated in the β decay of ^{62}Ge would also feature. As such, it would be expected that the $2^+ \rightarrow 0^+$ transition from the T = 1 isobaric analogue state in ^{62}Ga would feature strongly in the γ-ray spectrum shown in Figure 3.4. Additional supporting evidence for the T = 1 nature of the 1017 keV state comes from the non-observation of the 446 keV transition in the Grodner study, suggesting that the branch to the yrast 1^+ state from the 1017 keV state is weak compared with the branch to the ground state, in agreement with the branching ratios for the T = 1 2^+ state predicted in the Rudolph calculation [31].

In summary, the candidate T = 1 2^+ state proposed in the Rudolph work was observed in the current work. The possible observation of a transition directly to the ground state from the 1017 keV level in the β-decay study by Grodner *et al.* may indeed support the proposed T = 1 nature of the 1017 keV state. However, a full evaluation in the context of all previous experimental work, other newly observed low-lying states in the present study and theoretical predictions is necessary to provide a complete and self-consistent picture of the low-lying level scheme of ^{62}Ga, and is given in Section 6.3.

6.2.5 Level at 1439 keV

A peak at 621.9(2) keV is clearly visible in the singles spectrum shown in Figure 6.4a). The background subtracted coincidence spectrum for the 622 keV transition is shown in Figure 6.13. Strong coincidences with the 246 and 571 keV transitions are evident. This, with the lack of coincidences with any other higher-lying yrast transitions or any other non-yrast transitions, indicates that

the 621.9(2) keV transition originates from a state at 1439.1(2) keV that feeds the yrast 3^+ state at 817.2(1) keV.

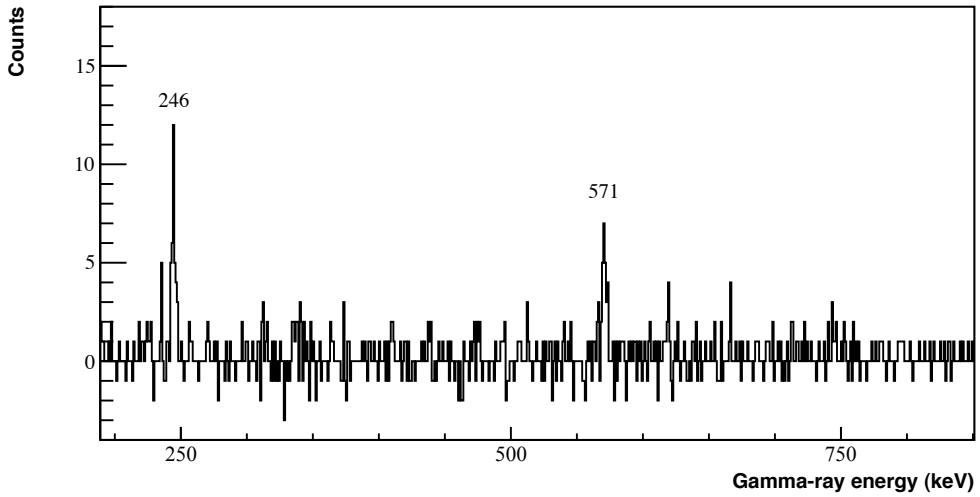

Figure 6.13 Background subtracted coincidence γ-ray spectrum for the 622 keV transition, using 2NN correlations.

The observation of a 1439.1(2) keV level that decays to the 3^+ state at 817 keV is in agreement with previous observations of a level at 1439 keV with a 621.4 keV transition to the 3^+ state in the Vincent study, and a level at 1439.4(2) keV with a 622.3(1) keV transition to the 3^+ state reported in the work by Rudolph *et al.* A value of $R_{32:90} = 1.26(36)$ was obtained in the current study for the 622 keV transition. This, compared with the reference value of $R_{32:90} = 1.15(3)$ for a $\Delta I = \pm 2$ transition, suggests that the 622 keV transition has $\Delta I = \pm 2$ character and implies a 1^+ or 5^+ assignment for the 1439 keV state. A 1^+ assignment can be ruled out as no 622 keV transition was observed in the β-decay study by Grodner *et al.*, which would be expected if the 1439 keV state was indeed 1^+.

In the Rudolph study, a 4^+ or 5^+ assignment was proposed for the level at 1439 keV. These possibilities were based on anisotropy measurements for one of the three weak transitions that were found to feed the 1439 keV state, and for the 622 keV transition depopulating the 1439 keV state. As the feeding of the 1439 keV state is distributed across three weak transitions, the non-observation of any feeding transitions in the 622 keV coincidence spectrum shown in Figure 6.13 does not conflict with the Rudolph results. A ratio using Directional Correlations of Oriented states (DCOs), R_{DCO}, was obtained for the 622 keV transition in the Rudolph work. See Section 2.3.2 for more information on DCOs. The value of

$R_{DCO} = 1.06(16)$ obtained for the 622 keV transition, compared with the reference value of $R_{DCO} = 1.0$ for E2 transitions, strongly indicated E2 character. A second anisotropy ratio was also obtained in the Rudolph work for the 622 keV transition (calculated using peak areas in summed spectra at $\sim 35°$ and $90°$ with respect to the beam direction) of $R_{35:90} = 1.37(10)$ also strongly indicated E2 character, as a known E2 transition was found to have a value of $R_{35:90} = 1.30(3)$. The possible 4^+ assignment was proposed for the 1439 keV state as a 934 keV transition, which feeds the 1439 keV transition from a 6^+ level at 2374 keV, was found to have an anisotropy ratio of $R_{35:90} = 1.22(28)$, suggesting E2 character. An explanation for this inconsistency given in the Rudolph work was a very strongly mixed $\Delta I = \pm 1$ 622 keV transition. However, the maximum value the anisotropy ratios of $R_{35:90}$ in the Rudolph work and $R_{32:90}$ in the present work would be 1.0 for a $\Delta I = \pm 1$ transition that is entirely dominated by the E2 component, which is not in agreement with this explanation. The state at 1439 keV is therefore assigned as 5^+.

6.2.6 Newly observed level at 1575 keV

As well as the 183 keV transition, which feeds the newly observed level at 979 keV, a second peak at 596 keV can be seen in coincidence with the 979 keV transition in Figure 6.7. The strong 596-979 keV coincidence is confirmed by the strong presence of a peak at 979 keV in the 596 keV coincidence spectrum shown in Figure 6.14. A known 597-980 keV coincidence exists in the isobaric nucleus ^{62}Cu [99]. However, the transition at 980 keV in ^{62}Cu directly feeds a very strong transition at 349 keV, whereas the 597 keV transition feeds the 980 keV transition indirectly from a higher-lying state. As there are no counts above background levels in the 979 keV coincidence spectrum at 349 keV in Figure 6.7, the peak at 596 keV cannot be attributed to ^{62}Cu.

Additionally, as shown in Appendix A, the peaks at 979 and 596 keV in the singles spectra are associated with β-decay half-lives of 133(17) ms and 113(47) ms, respectively, which are both consistent with the 116 ms half-life of ^{62}Ga and cannot originate from long-lived or stable isotopes. Due to the strong presence of the 979 keV transition in the 596 keV coincidence spectrum with no yrast transitions apparent, and the lack of the 596 keV transition in the summed yrast spectrum shown in Figure 6.5, it can be deduced that a state exists at 1575.1(7) keV, which feeds the state at 979 keV via a 595.9(9) keV transition.

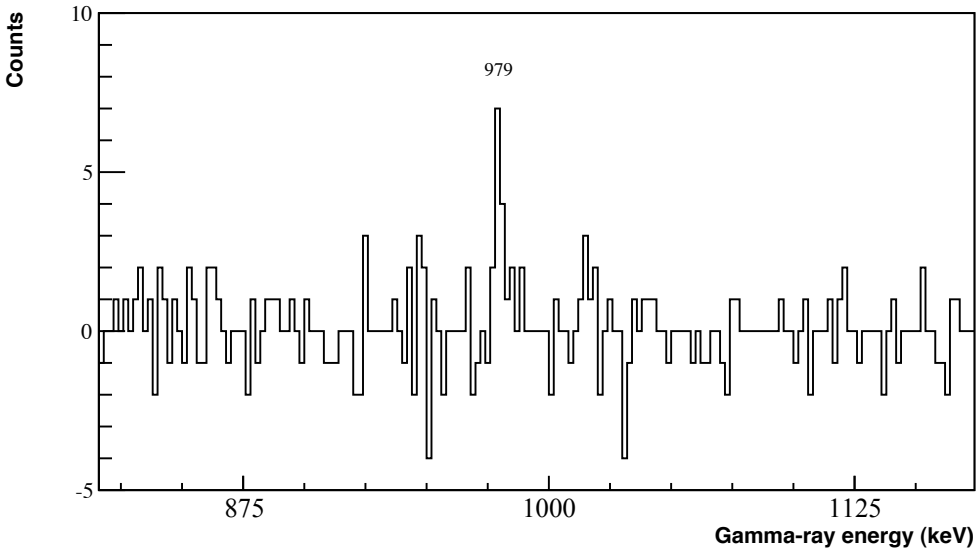

Figure 6.14 Background subtracted coincidence γ-ray spectrum for the 596 keV transition using 2NN correlations.

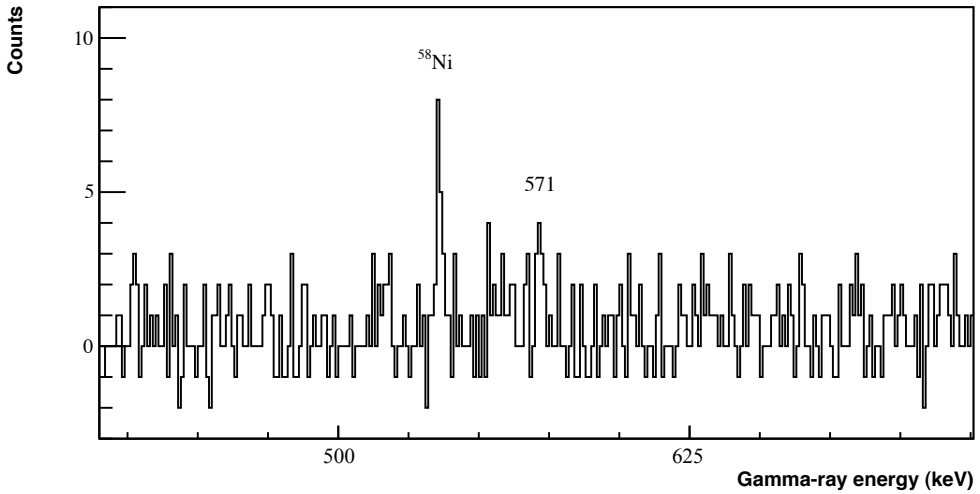

Figure 6.15 Background subtracted coincidence γ-ray spectrum for the 1004 keV transition using 2NN correlations.

Supporting evidence for a state at 1575 keV comes from a hint of a 1004-571 keV coincidence, evident in the background subtracted coincidence spectrum for the 1004 keV transition, shown in Figure 6.15. The 1004 keV transition can be seen in the singles spectrum shown in Figure 6.4b). The coincidence at 537 keV shown in Figure 6.15 originates from the contaminant isotope ^{58}Ni [100], as a strong ^{58}Ni peak at 1005 keV contaminates the 1004 keV coincidence gate. However, no known 1005-571 keV coincidence exists in ^{58}Ni. Although an indirect 1002-571 keV coincidence does exist in ^{62}Cu, the 1002 keV transition is also coincident with the very strong 349 keV transition, which is absent from the 1004 keV coincidence spectrum. The transition at 1004 keV therefore originates from the 1575 keV state, feeding the 1^+ state at 571 keV.

An anisotropy ratio of $R_{32:90} = 1.12(54)$ was obtained for the 596 keV transition, which has an error too large for an assignment to be made. The branches from the 1575 keV transition to the 1^+ state at 571 keV and the 979 keV state allows a tentative assignment of $(2, 3^+)$ for the 1575 keV state. A 3^- assignment can be ruled out as M2 radiation would not be detected in the current work. A 1^+ assignment for the 1575 keV state is very unlikely as no transitions at 596 keV or 1004 keV were observed in the study by Grodner *et al.*, which would be expected if the 1575 keV state was a 1^+ state.

6.2.7 Newly observed level at 2212 keV

As well as the transitions at 183 keV and 596 keV, a third transition at 1233 keV is visible in the high energy portion of the 979 keV coincidence spectrum shown in Figure 6.7. A simulated coincidence spectrum is shown in the inset of the lower panel of Figure 6.7 for comparison with the real data, carried out in the ROOT analysis framework [95]. Events in the simulated peak consist of random numbers generated from a Gaussian distribution with a full width at half maximum (FWHM) of 8 keV chosen to match the peak width of the 1241 keV peak in the singles data. The number of events in the peak was chosen to match the 7 % relative intensity estimated for the 1233 keV peak measured in the real experimental data. The background is assumed to be uniformly distributed in the energy region of interest, with 0.2 counts per channel to match the levels observed in the real data. It can be seen by comparing the simulated spectrum in the inset and experimentally measured spectrum that the 1233 keV peak has a width and shape consistent with expectations based on the simulation.

It should be noted that, despite the near degeneracy of the 1233 keV transition and the strong $4^+ \rightarrow 2^+$ 1232 keV transition in ^{62}Zn, the difference in energy between the 979 keV transition and the $2^+ \rightarrow 0^+$ transition at 954 keV in ^{62}Zn is large enough to prevent any contamination of the 979 keV coincidence spectrum. A weak 983-1232 keV coincidence does exist in ^{62}Zn. However, a strong peak at 1057 keV would be visible in the coincidence spectrum if the 1233 keV peak is due to contamination from ^{62}Zn, as the 983 keV transition in ^{62}Zn feeds a 1057 keV transition directly. No counts at 1057 keV appear in the 979 keV coincidence spectrum, confirming that the 1233-979 keV coincidence originates from ^{62}Ga.

A transition at 1233 keV does not appear in any other coincidence spectra for transitions in ^{62}Ga, nor does a transition at 1233 keV appear in the yrast summed spectrum shown in Figure 6.5, suggesting that the 1233 keV transition directly feeds the 979 keV state. This implies that a new level at 2211.5(5) keV has been observed, which feeds the 979 keV state via a 1232.7(3) keV γ ray. As no anisotropy information could be obtained for the 1233 keV transition, only limits on the spin of the 2212 keV state can be made due to the branch to the 979 keV state, which has a strongly favoured 1^+ assignment. With the assumption that states with increasing excitation energy have increasing spin, the 2212 keV state is therefore tentatively assigned as $(2, 3^+)$.

6.2.8 Level at 2237 keV

A level at 2234.0(5) keV was proposed as a candidate for the T = 1 4^+ isobaric analogue state in the study by Rudolph *et al.* due to its close proximity to the 4^+ state in ^{62}Zn at 2186 keV. The 2234 keV state was reported to decay to the yrast 3^+ level at 817 keV and to the 5^+ level at 1439 keV via transitions at 1417(1) and 794.4(5) keV, respectively. In the Rudolph study, anisotropy information for the 1417(1) keV transition feeding the 3^+ yrast state that indicated ΔI = $\pm$1 character provided a possible J = 4 assignment for the 2234 keV state, supporting the possibility that the 2234 keV level is the 4^+ isobaric analogue state. This Section reports the observation of the T = 1 4^+ candidate state in the present study, identified through direct feeding of the yrast 3^+ level at 817 keV. A hint of a peak at 1420.1(17) keV is apparent in the coincidence spectrum for the 246 keV transition, shown in Figure 6.16. The 246-1420 keV coincidence is confirmed by the strong presence of the 246 keV transition in the 1420 keV coincidence spectrum, shown in Figure 6.17. An indirect 243-1418 keV coincidence exists in

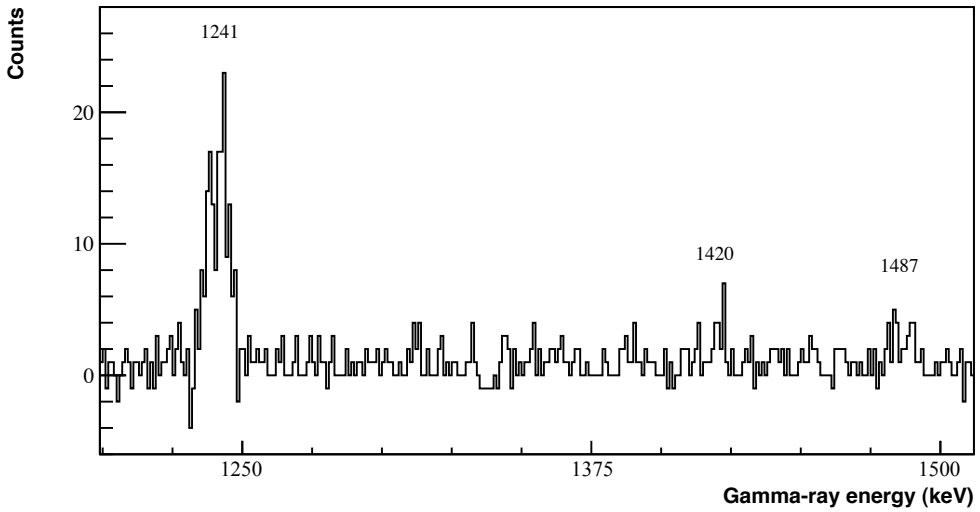

Figure 6.16 Background subtracted coincidence γ-ray spectrum for the 246 keV transition, using 2NN correlations.

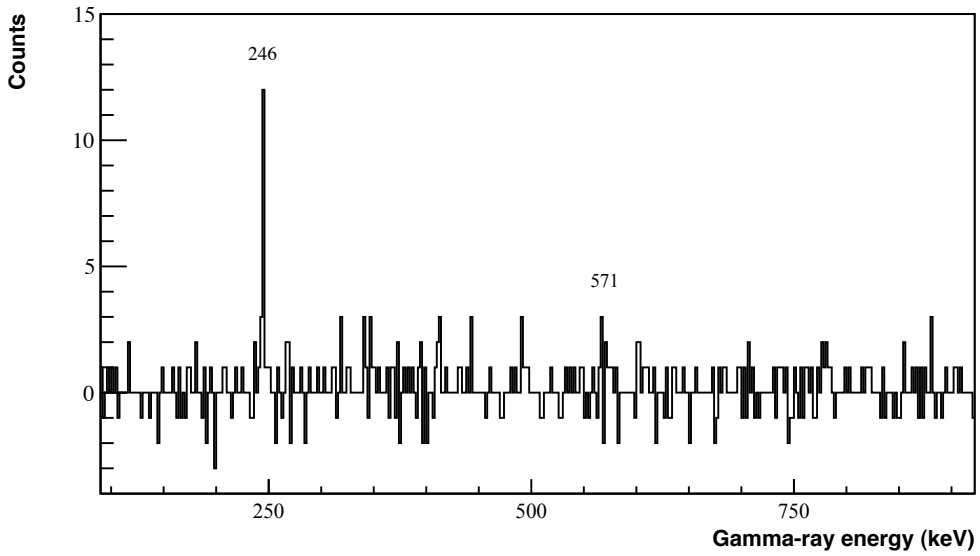

Figure 6.17 Background subtracted coincidence γ-ray spectrum for the 1420 keV transition, using 2NN correlations.

the contaminant nucleus ^{62}Cu. However, several intermediate transitions linking the 1418 and 243 keV transitions in ^{62}Cu would be apparent in Figure 6.17 if the 246 keV peak is due to contamination from ^{62}Cu, which is not the case. From the lack of any strong transitions other than the 246 keV peak in the 1420 keV coincidence spectrum, it can be deduced that the 1420 keV transition directly feeds the 3^+ yrast state at 817 keV from a state at 2237.3(17) keV.

The 2237.3(17) keV state observed in the present study is in agreement with the level at 2234 keV previously reported by Rudolph *et al.*, which was found to decay to the yrast 3^+ state at 817 keV. Although the branch to the 1439 keV state from the 2237 keV level reported by Rudolph was not observed in the current work, this is consistent as the transition to the 3^+ yrast state was found to be the stronger branch in the Rudolph work. As no anisotropy information was obtained for the 1420 keV transition in the present work, no definite spin assignment can be made for the 2237 keV state. As discussed previously, however, its proximity in energy to the 2186 keV T = 1 4^+ state in ^{62}Zn makes the 2237 keV state a good candidate for the isobaric analogue state. A full discussion of the 2237 keV state in the context of theoretical predictions will be given in Section 6.3.

6.2.9 Level at 2374 keV

As described in Section 6.1, an increase in peak width for the peak visible at ∼1180 keV in the singles spectrum shown in Figure 6.4b) indicates that more than one transition exists in ^{62}Ga similar to this energy. In the 376 keV coincidence spectrum, shown in Figure 6.18, however, the peak at ∼1180 keV is of comparable width to surrounding peaks and has an energy less than the peak visible in the singles spectrum. The energy measured in the 376 keV coincidence spectrum of 1179.4(7) keV is in agreement with a transition at 1180.1(3) keV previously observed in the Rudolph study. The relative intensity of the 1179 keV transition given in Table 6.1 was therefore estimated using the peak intensity measured in the 376 keV coincidence spectrum.

The 1179 keV coincidence spectrum is shown in Figure 6.19. Contamination from transitions in ^{62}Ga at similar energy to the 1179 keV transition that contribute to the peak will be present in the coincidence spectrum. It has not been possible in the coincidence analysis to distinguish between coincidences belonging to individual transitions at ∼1180 keV. Additionally, the 1179 keV coincidence spectrum is contaminated by a strong transition at 1177 keV in ^{62}Zn. Starred

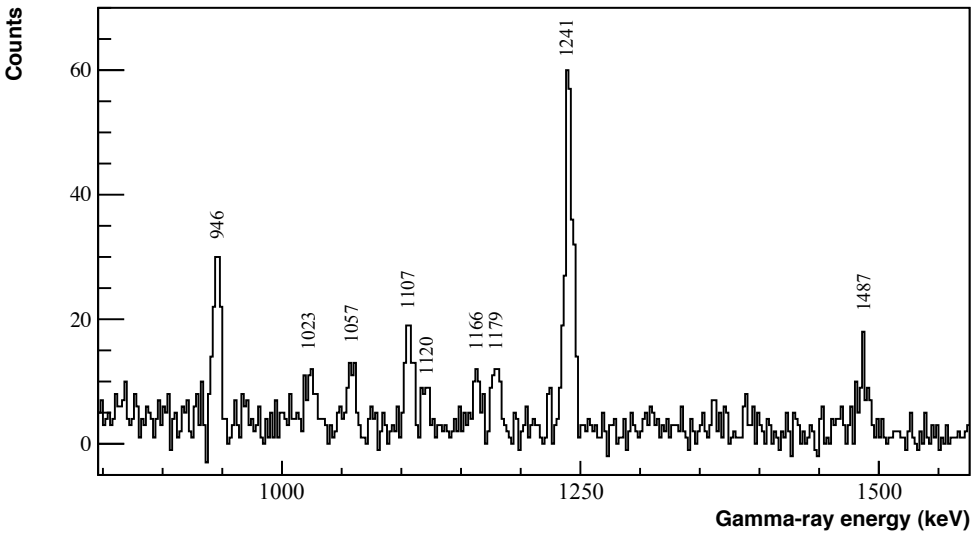

Figure 6.18 Background subtracted coincidence γ-ray spectrum for the 376 keV transition, using 2NN correlations.

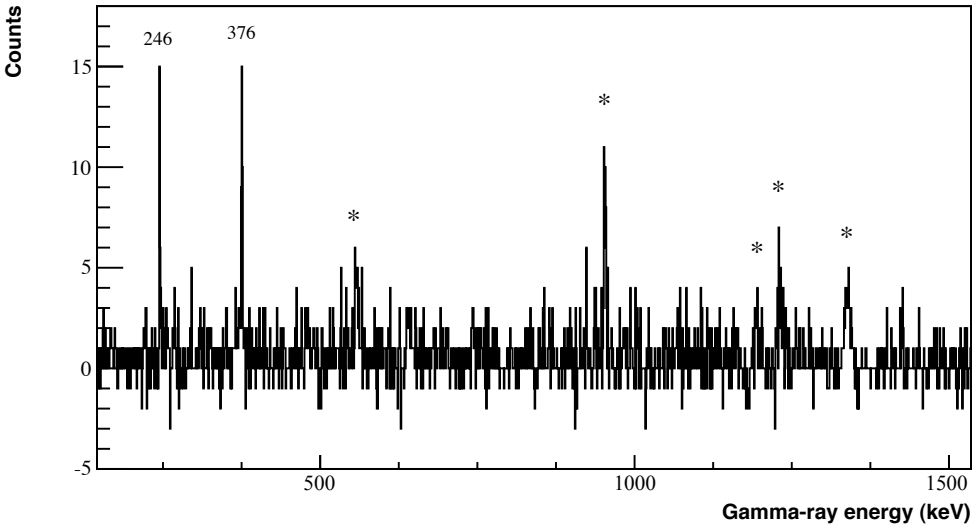

Figure 6.19 Background subtracted coincidence γ-ray spectrum for the 1179 keV transition, using 2NN correlations. Starred transitions are attributed to ^{62}Zn.

transitions in Figure 6.19 are therefore attributed to ^{62}Zn. Strong coincidences with the 246 and 376 keV transitions can nevertheless be seen in the 1179 keV coincidence spectrum. The lack of a 1241 keV peak and any strong coincidences with non-yrast transitions in Figure 6.19 indicates that the 1179.4(7) keV transition directly feeds the 5^+ yrast state at 1193 keV from a state at 2373.8(4) keV, if contamination from nearby ^{62}Ga transitions is assumed to be negligible. The observation of a state at 2374 keV that strongly feeds the 5^+ yrast state is in agreement with observations in the studies by both Vincent and Rudolph.

A transition at 934.2(4) keV, which feeds the state at 1439 keV, was reported to originate from the 2374 keV state in the Rudolph work. Although no 934 transition was observed in any coincidence spectra in the current work, a weak transition at 935.3(4) keV was observed in the singles γ-ray spectra. The 935.3(4) keV transition is therefore tentatively placed as the transition from the 2374 keV level to the 1439 keV level.

A value of $R_{32:90} = 0.60(22)$ was obtained for the 1179 keV transition in the current work. This value is in brackets in Table 6.1 because, as discussed, it is suspected that other transitions in ^{62}Ga exist at $\sim$1180 keV, therefore possibly skewing the measured anisotropy ratio. If these issues are neglected, the value of $R_{32:90}$ strongly indicates $\Delta I = \pm 1$ character for the 1179 keV transition, giving a J = 4 or 6 assignment for the 2374 keV state. This is consistent with the 6^+ assignment given to the 2374 keV state in the Rudolph work.

6.2.10 Newly observed level at 2989 keV

A transition at 1796.5(9) keV, not observed in previous studies, is clearly visible in the singles spectrum shown in Figure 6.4c). The coincidence spectrum for the 1797 keV transition is shown in Figure 6.20. The spectrum was created using the 1NN coincidence matrix to reduce contamination from transitions in both ^{58}Ni and ^{62}Zn at $\sim$ 1797 keV. A strong 376 keV transition is present in Figure 6.20.

If the 1797 keV transition were to feed a non-yrast state, a linking transition between the 1797 and 376 keV transitions would be evident in Figure 6.20. The lack of a linking transition indicates that the 1797 keV transition directly feeds the yrast band. If the 1797 keV transition were to feed an yrast state higher than the 5^+ state at 1193 keV, from which the 376 keV transition originates, then at

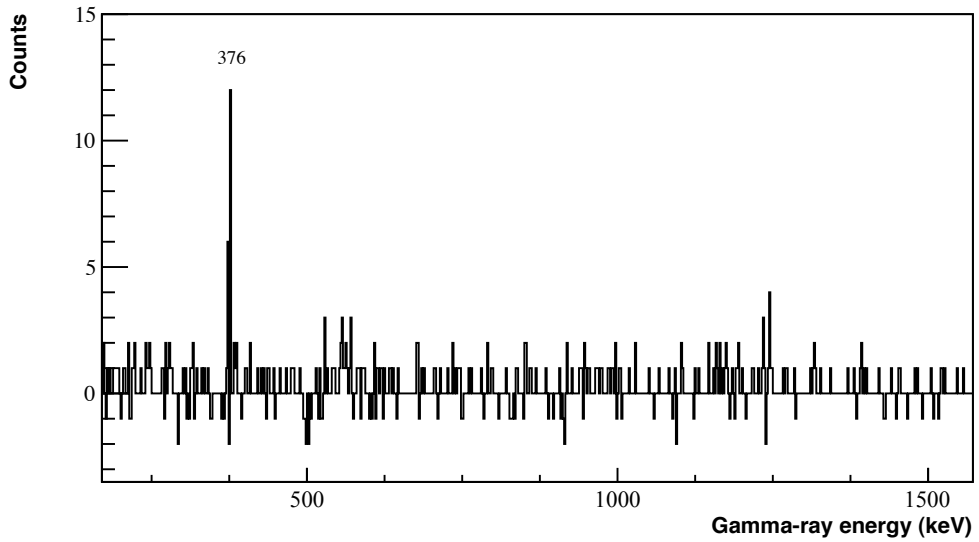

Figure 6.20 Background subtracted coincidence γ-ray spectrum for the 1797 keV transition, using 1NN correlations.

least 10 counts would be expected at 1241 keV as there are ~ 20 counts in the 376 keV peak and the γ-ray detection efficiency at ~ 1.2 MeV is half that at ~ 0.4 MeV. As only five counts appear in Figure 6.20 in the energy range containing one FWHM of the 1241 keV peak, with no counts in the bin corresponding to the centroid, it can be deduced that the 1796.5(9) keV transition feeds the 5^+ yrast state from a newly observed state at 2989.4(9) keV. No anisotropy information could be obtained for the 1797 keV transition, so the spin can only be constrained due to the branch to the 5^+ state. As no branches to lower-lying yrast states have been observed, and with the assumption of increasing spin with excitation energy, the assignment is tentatively constrained to 5, 6 or 7^+.

6.2.11 Level at 3491 keV

In the Rudolph study, a level at 3492 keV that feeds the yrast 7^+ level at 2434 keV via a 1057.6(2) keV γ ray was identified. A second branch from the 3492 keV state to the level at 2374 keV was also reported. In the current work, a transition at 1057.4(5) keV is clearly visible in the singles spectrum shown in Figure 6.4b). The coincidence spectrum for the 1057 keV transition, shown in Figure 6.21, contains yrast transitions at 1241, 376 and 246 keV. As no peak exists at 2356 keV in the 1057 keV coincidence spectrum, it can be deduced that the 1057 keV transition feeds the 7^+ yrast level at 2434 keV directly from a level

at 3491.4(5) keV, in agreement with the previous observations in the Rudolph study. Supporting evidence for the direct feeding of the 2434 keV yrast state by the 1057 keV transition is provided by the presence of the 1057 keV transition in the 1241 keV coincidence spectrum shown in Figure 6.22.

It should be noted that an unknown transition at $\sim$ 1245 keV appears in the 1241 keV coincidence spectrum, shown in Figure 6.22. Residual counts from the strong 1241 keV yrast transition in the 1241 keV coincidence gate can be ruled out as background levels in this energy region are very low. No known strong 1241-1245 keV coincidences exist in any contaminant nuclei, and no other significant contamination is observed in the 1241 keV coincidence spectrum. It can then be deduced that the $\sim$ 1245 keV transition does in fact originate from ^{62}Ga, but cannot be placed in the level scheme due to insufficient statistics.

In the Rudolph study, an additional branch from the 3491 keV state was reported to feed the 6^+ state at 2374 keV. Although no 1118 keV γ ray was observed in coincidence with the 1179 keV transition in the current work, a peak at 1120.3(12) keV was observed in coincidence with the 376 keV transition, shown in Figure 6.18, providing supporting evidence for a transition from the 3491 keV state to the 2374 keV state. The 1120.3(12) keV transition is therefore tentatively attributed to originating from the 3491 keV state, feeding the 6^+ 2374 keV level, in Table 6.1.

In addition to the 1057 keV and 1120 keV transitions, a third transition at 478 keV was also found to de-populate the 3491 keV state in the present study, feeding the 6^+ state at 3013 keV. This is evident by the appearance of a peak at 478.3(11) keV in the coincidence spectrum for the 340 keV transition, which was found to originate from the 3013 keV state.

An unknown peak at 1954 keV is visible in the 1057 keV coincidence spectrum shown in Figure 6.21. The only transition at $\sim$1954 keV that may contaminate the 1057 keV coincidence spectrum originates from ^{58}Cu, which exhibits an extremely weak coincidence between a transition at 1051 keV that feeds the ground state and a transition at 1955 keV that originates from a state at $\sim$14.5 MeV. As no other transitions from ^{58}Cu are visible in the 1057 keV coincidence spectrum, the 1057-1954 keV coincidence is attributed to ^{62}Ga. Very low levels of statistics prevent a definite placement of the 1954 keV transition in the level scheme, and so the 1954 keV γ-ray transition is not included in Table 6.1.

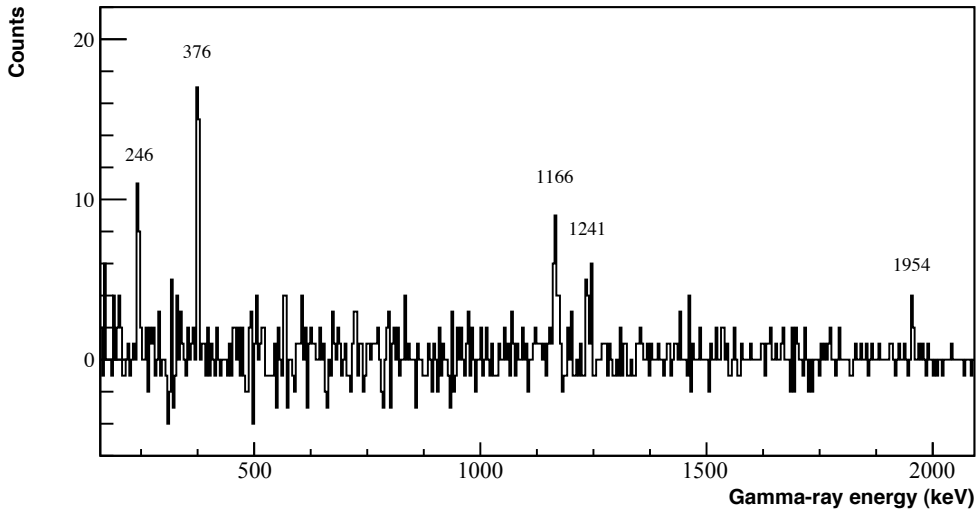

Figure 6.21 Background subtracted coincidence γ-ray spectrum for the 1057 keV transition, using 2NN correlations.

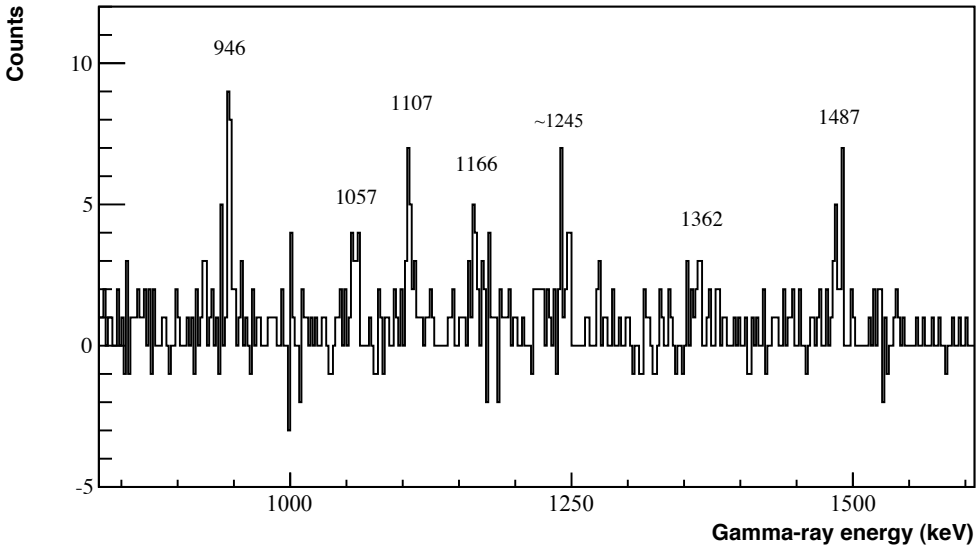

Figure 6.22 Background subtracted coincidence γ-ray spectrum for the 1241 keV transition, using 1NN correlations.

The spin of the 3491 keV state was fixed to J = 7 in the Rudolph study based on angular distribution information for the 1057 and 1118 keV transitions. As no $R_{32:90}$ values for transitions depopulating the 3491 keV level were obtained in the current work, the spin assignment of the 3491 keV state remains unchanged.

6.2.12 Confirmation of the level at 3796 keV

In the work by Rudolph *et al.*, a tentative level at 3797 keV that fed the states at 1193, 2374 and 2434 keV was proposed but could not be firmly established. In the current work, a peak at 1362.2(7) keV was observed in the singles spectrum. Coincidences with yrast transitions at 246, 376, 571 and 1241 keV are visible in the 1362 keV coincidence spectrum shown in Figure 6.23. No counts appear at 2356 keV in coincidence with the 1362 keV transition, indicating that the 1362 keV transition feeds the 7^+ yrast state at 2434 keV from a state at 3795.7(7) keV. The direct feeding of the 2434 keV state by the 1362 keV transition is supported by the presence of the 1362 keV γ ray in the 1241 keV coincidence spectrum, shown in Figure 6.22. The state at 3796 keV is in agreement with the possible level at 3797 keV reported in the Rudolph study, which was found to feed the 7^+ yrast state via a 1363 keV γ ray. Although a possible weak coincidence with a transition at $\sim$ 510 keV is also apparent in the 1362 keV coincidence spectrum in the present work, the low level of statistics means this cannot be established in the level scheme.

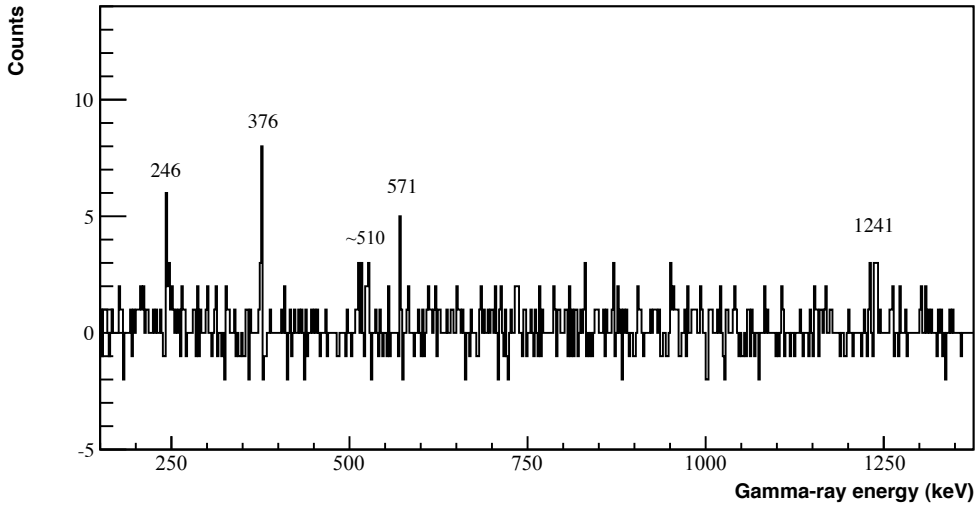

Figure 6.23 Background subtracted coincidence γ-ray spectrum for the 1362 keV transition, using 2NN correlations.

No anisotropy information was obtained in the current work for the 1362 keV transition, so it is not possible to make a definite spin assignment. However, constraints on the spin can be made due to the observed branch to the 7^+ yrast state at 2434 keV in the present work, and the tentatively observed branches to the 5^+ yrast state and the 6^+ state at 2374 keV in the Rudolph work. With the assumption that states with increasingly excitation have increasing spin, a tentative 7^+ assignment is proposed for the 3796 keV level.

6.2.13 Level at 4656 keV

In the Rudolph study, a state was observed at 4658 keV that fed the J = 7 level at 3491 keV via an 1166.0(3) keV γ ray. The observation of a strong peak at 1166 keV in the 1057 keV coincidence spectrum in the present study, shown in Figure 6.21, indicates that a level at 4656.4(9) keV feeds the 3491 keV level, in agreement with the Rudolph study.

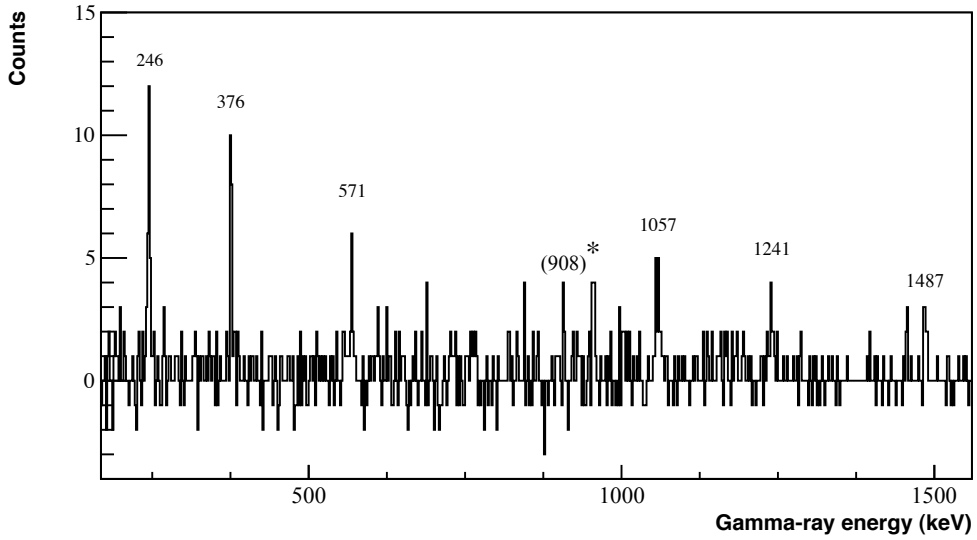

Figure 6.24 Background subtracted coincidence γ-ray spectrum for the 1166 keV transition, using 1NN correlations. The starred transition is attributed to ^{62}Zn.

Supporting evidence for the 4656 keV level is provided by the 1166 keV coincidence spectrum, shown in Figure 6.24. As the 1166 keV transition is contaminated by transitions at ∼1161 keV in both ^{62}Zn and ^{58}Ni, the coincidence spectrum for the 1166 keV transition has been made using the 1NN matrix. The starred transition at 954 keV in Figure 6.24 is attributed to contamination from

^{62}Zn. Coincidences with yrast transitions at 246, 376, 571 and 1241 keV are clear. The 1057 keV transition is the strongest in Figure 6.24, after correcting for efficiency, confirming that the 1166 keV transition feeds the 1057 keV transition directly. As no counts are visible at 2356 keV in the 1166 keV coincidence spectrum, this confirms that the 1166-1057 keV cascade feeds the 7^+ state at 2434 keV, which de-excites via the 1241 keV yrast transition.

A peak at 1487 keV and a hint of the 908 keV transition are visible in the 1166 keV coincidence spectrum in Figure 6.24. As the 1166 keV transition was found to directly feed a state lower in excitation than the 3920 keV state, from which the 908 and 1487 keV transitions originate, in both the current work and previous work by Rudolph *et al.*, the appearance of the 1487 keV peak in Figure 6.24 cannot be explained with the current level scheme. A full discussion of the 3920 keV state and the 908 keV and 1487 keV transitions is given in Section 6.2.3. No 1166-1487 keV coincidence is known in any contaminant species. It can be speculated, therefore, that two distinct transitions exists, which share a very similar energy at 1166 keV. One of these transitions feeds the 8^+ state at 3920 keV and the other feeds the J = 7 state at 3491 keV. An alternate explanation may be that the 1166 keV transition in fact feeds an unknown state at higher excitation, and feeds both the 3920 and 3491 keV states through linking transitions not currently identified.

A value of $R_{32:90} = 0.93(29)$ for the 1166 keV transition, which feeds the J = 7 state at 3491 keV, was obtained in the present study that indicates $\Delta I = \pm 1$ character, although the value is somewhat ambiguous. In the Rudolph study, the spin of the 4656 keV level was fixed to J = 8 based on an anisotropy measurement of the 1166 keV transition. Although the anisotropy ratio for the 1166 keV obtained in the present study is not conclusive, the $R_{32:90} = 0.93(29)$ value is nevertheless in agreement with the J = 8 assignment for the 4656 keV level.

6.3 Discussion of the results

This Section provides a discussion of low-lying levels observed in the present study in the context of previous experimental work and theoretical predictions. The first observation of a low-lying level at 979 keV that exhibits a 100 % branch to the ground state is reported in the current work. The 979 keV state has been assigned a spin-parity of 1^+, as will be discussed in this Section. Another newly

observed level at 1161 keV is interpreted as the lowest-lying T = 0 2^+ state, and was found to feed both the yrast 1^+ state at 571 keV and the 979 keV state. The 1161 keV state can be ruled out as a candidate for the T = 1 2^+ isobaric analogue state as the energy is more than 200 keV higher than the 2^+ state at 954 keV in ^{62}Zn and studies of similar nuclei have shown that isobaric analogue states of this type are typically within tens of keV. An excellent candidate for the isobaric analogue T = 1 2^+ state at 1017 keV, which was previously reported in a study by Rudolph *et al.* [31], has also been observed in the current work. A further low-lying state at 1575 keV that exhibits branches to the 1^+ states at 571 and 979 keV has been newly identified in the present study. Several other higher-lying states have been observed for the first time, and the odd-spin yrast band has been tentatively extended to a 17^+ state at $\sim$ 10 MeV.

A β-decay study of ^{62}Ge by Grodner *et al.* [73], described in Section 3.2, provides a great deal of information regarding the 979 and 1017 keV states. Allowed Gamow-Teller and non-superallowed Fermi β decays of ^{62}Ge populate 1^+ states and T = 1 0^+ states in ^{62}Ga, respectively. γ-ray transitions from 1^+ and T = 1 0^+ states in ^{62}Ga will therefore occur following non-superallowed β decays of ^{62}Ge. As discussed in Section 6.2.4, the $2^+ \rightarrow 0^+$ transition from the first excited T = 1 2^+ state to the T = 1 0^+ ground state is also expected to be present in the γ-ray spectrum measured following β decays of ^{62}Ge. It is known that the analogue $2^+ \rightarrow 0^+$ transition in ^{62}Ga must be close in energy to the 954 keV $2^+ \rightarrow 0^+$ transition exhibited in ^{62}Zn. Two candidate transitions close to 954 keV were reported at 978 and 1017 keV following β decays of ^{62}Ge. The 978 and 1017 keV γ rays can be interpreted as the transitions directly feeding the ground state from the levels at 979 and 1017 keV, respectively. As the 1017 keV level has a robust J = 2 assignment from the Rudolph results, and the 979 keV level has a strongly favoured J = 1 assignment in the present results, the observations reported in the Grodner study strongly support a 1^+ assignment for the 979 keV state and a T = 1 2^+ assignment for the 1017 keV state.

Theoretical predictions regarding low-lying 1^+ states in ^{62}Ga and the nature of the T = 1 2^+ isobaric analogue state are in excellent agreement with the 1^+ assignment for the 979 keV state and the T = 1 2^+ assignment for the 1017 keV state. Figure 6.25 presents the energy levels up to 2 MeV in ^{62}Ga determined experimentally in the current work compared with theoretical predictions made using the shell model [43, 78], deformed shell model [32] and IBM-4 model [33]. On the left-hand side of Figure 6.25 are the excitation energies of 1^+ states

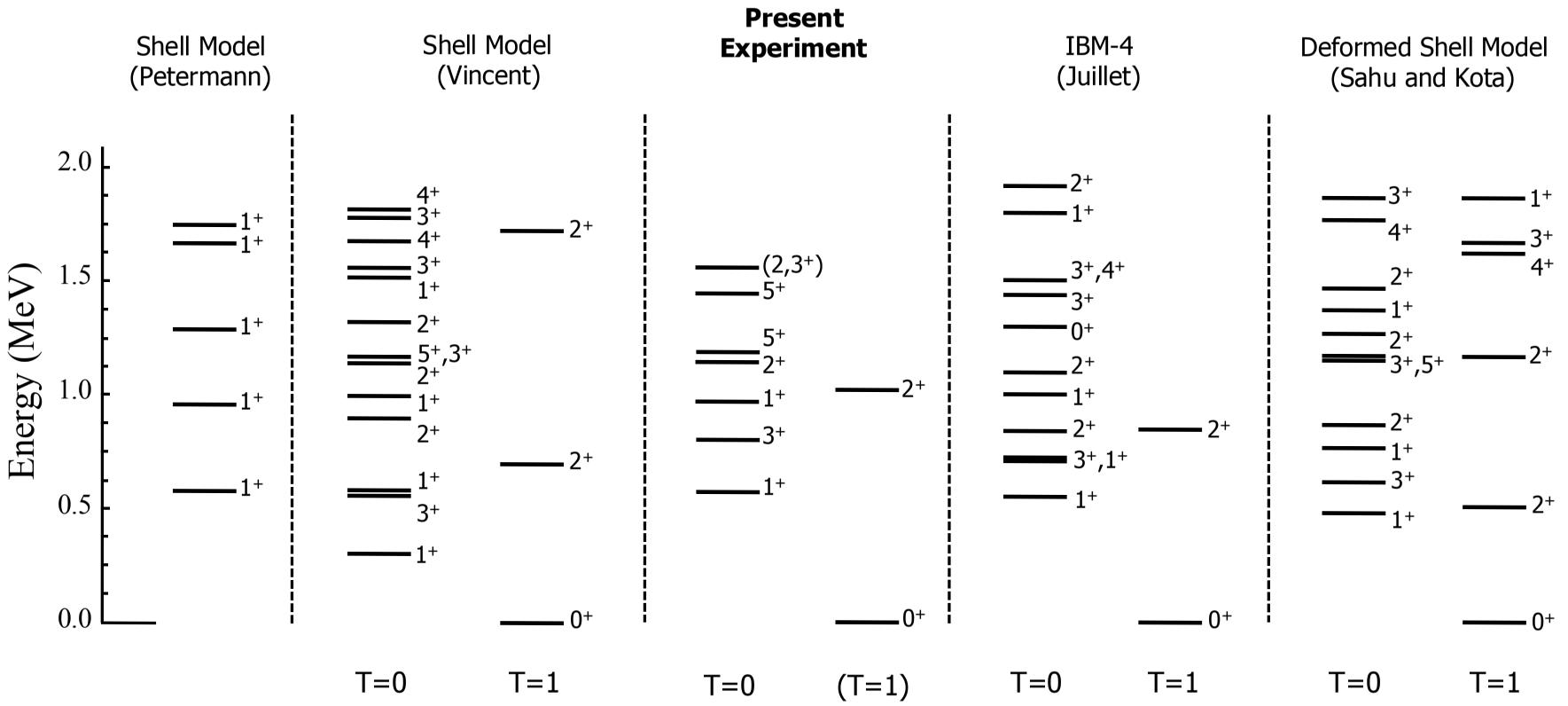

Figure 6.25 Energy levels in ^{62}Ga up to 2 MeV determined in the present study compared with theoretical predictions made using the shell model (Vincent *et al.* [43]), IBM-4 model (Juillet *et al.* [33]) and deformed shell model (Sahu and Kota [32]). Predicted excitation energies of 1^+ states calculated using the shell model in a Gamow-Teller strength study by Petermann *et al.* [78] are also shown.

calculated in a study by Petermann *et al.* that predicted Gamow-Teller β-decay strengths using the shell model [78]. It can be seen from Figure 6.25 that the predicted excitation energy of the 1^+ state at ~ 1 MeV in the Petermann study is in excellent agreement with the observed level at 979 keV. It is assumed that the energy of the first excited 1^+ state has been fixed to 571 keV in the Petermann calculation as this experimentally determined information was available at the time of the calculation.

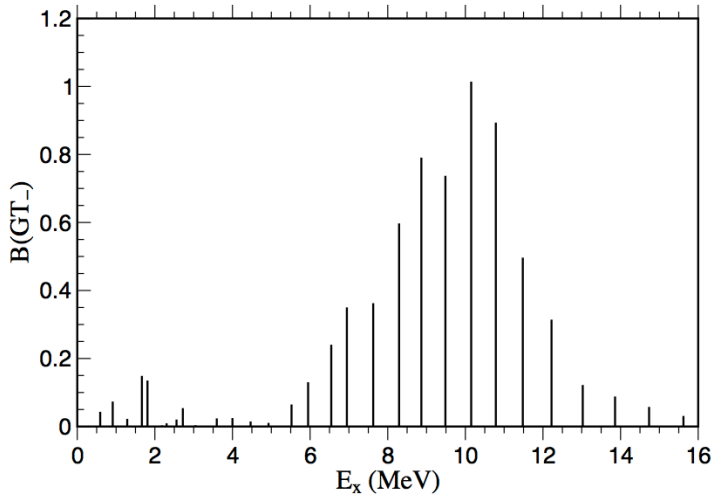

Figure 6.26 Predicted Gamow-Teller strength distribution for β decays of ^{62}Ge [78].

The calculated strengths of the Gamow-Teller β decays to the first two excited 1^+ states can be estimated using Figure 6.26 as B(GT) = 0.04 for the 571 keV state and B(GT) = 0.07 for the second excited 1^+ state. These predicted values are in agreement with the experimental values from the Grodner study of B(GT) = $0.07^{+0.017}_{-0.017}$ for the 571 keV state and B(GT) = $0.05^{+0.015}_{-0.017}$ for the 979 keV state [101]. The third excited 1^+ state is predicted to have an excitation energy of ~ 1.3 MeV in the Petermann calculation. It can be speculated that the transition observed at 1247 keV in the Grodner β-decay study is the $1^+ \rightarrow 0^+$ transition from the third excited 1^+ state at 1247 keV.

Consideration of the comparisons presented in Figure 6.25 allows a judgement of the level of agreement exhibited by the shell model (Vincent), IBM-4 model (Juillet) and deformed shell model (Sahu and Kota) with respect to the experimentally determined results to be made. It should firstly be noted that all three of the models predict a negative Coulomb energy difference (CED) for the isobaric analogue T = 1 2^+ state in ^{62}Ga to the 2^+ state at 954 keV in ^{62}Zn, where the CED = $E_x{}^{2^+}(^{62}\mathrm{Ga}) - E_x{}^{2^+}(^{62}\mathrm{Zn})$. Studies of similar nuclei in this mass

region show that CEDs are expected to be within tens of keV and positive [31]. For example, the CED for the 2^+ isobaric analogue states in ^{66}As and ^{66}Ge is known to be +7 keV [39]. If the 1017 keV level is interpreted as the T = 1 2^+ isobaric analogue state, then the CED is +63 keV. The deformed shell model prediction for the energy of the T = 1 2^+ state, which lies at $\sim$ 500 keV, is far too low. The IBM-4 calculation best reproduces the T = 1 2^+ excitation energy, although the value is still $\sim$ 150 keV too low.

Levels of agreement between predicted T = 0 levels and experimentally determined levels also vary between the shell model, IBM-4 model and deformed shell model calculations. All three of the models predict the correct ordering $(1^+, 3^+, 1^+, 2^+)$ of the first four T = 0 states. However, the shell model calculation and IBM-4 calculation both predict near degeneracy of the 3^+ and second excited 1^+ states. The observed regular spacing of the levels is only reproduced in the deformed shell model calculation. The deformed shell model is, however, the only model that does not correctly predict that the T = 1 2^+ state lies between the second excited 1^+ state and the first excited T = 0 2^+ state. A general observation is that all of the predicted states in the shell model and deformed shell model are typically at least 200 keV too low in energy. The IBM-4 calculation reproduces the absolute energies of the first excited 1^+ and 3^+ states well, but the predicted values of the second excited 1^+ state and first excited T = 0 2^+ state are too low. Although the deformed shell model is the most successful at reproducing the relative spacing of the low-lying T = 0 states, the T = 1 2^+ level energy is not reproduced well and the T = 0 levels are $\sim 100 - 200$ keV too low. In terms of overall characteristics of both T = 0 and T = 1 states, the IBM-4 model used by Juillet *et al.* exhibits the highest levels of agreement with experimental data out of the models shown in Figure 6.25.

In the 2004 Rudolph study, a calculation to predict the branching ratios for several states, including the T = 1 2^+ state and the lowest-lying T = 0 2^+ and 3^+ states, was carried out using the shell model. Although excellent agreement with experimental values of yrast states was found, no profound agreement between any predicted non-yrast states and experimentally determined levels was demonstrated, with mismatches becoming more evident at increasing excitation energies. The authors propose that "[o]ne possible explanation [for mismatches] can be the missing $1f_{7/2}$ one-hole or two-hole excitations, which could be important in this energy and spin regime" [31]. It should be noted that the branching ratio calculation was carried out with assumptions of the excitation

energies of the low-lying levels. As the transition probabilities are sensitive to the energy of the γ-ray radiation emitted, only very broad comparisons can be made between the predictions and the experimental values.

The Rudolph shell model calculation predicts an 81 % branch to the ground state from the T = 1 2^+ state, with a second 19 % branch to the yrast 1^+ state at 571 keV. The T = 0 2^+ state is expected to exhibit rather different behaviour, with no branch to the ground state predicted and a strong branch to the yrast 1^+ state at 571 keV. In the current study, and the experimental work by Rudolph *et al.*, a 100 % branch to the 1^+ state at 571 keV was observed from the state at 1017 keV, with no observed branch to the ground state. However, the observation of the 1017 keV transition in the Grodner study following β decays of ^{62}Ge suggests that a branch to the ground state from the 1017 keV state does indeed exist. As only one low-lying 2^+ state is predicted to have a branch to the ground state according to the Rudolph branching predictions, the observation of the 1017 keV transition in the Grodner study from the 1017 keV state, which has a robust J = 2 assignment, provides further supporting evidence for the T = 1 2^+ assignment for the 1017 keV state. The non-observation of the 446 keV transition in the Grodner study suggests that the branch from the 1017 keV state to the yrast 1^+ state at 571 keV is weaker than the branch to the ground state, also agreeing with the predicted branching ratios for the T = 1 2^+ state. A limit on the relative intensity of the 1017 keV transition of 2 % was estimated from the singles spectra obtained in the present work, compared with the estimated relative intensity of the 446 keV transition of 4(2) %. As neither the 446 nor 1017 keV transition were observed in the singles spectra in the current work, with the 446 keV transition only becoming apparent in the coincidence analysis, the non-observation of the 1017 keV transition in the present study is largely consistent with both the Grodner study and the branching predictions in the Rudolph work.

The newly observed 1161 keV level is interpreted as the lowest-lying T = 0 2^+ state. An 86(7) % branch to the yrast 1^+ state and a 14(7) % branch to the state at 979 keV were observed from the 1161 keV state in the current work. In comparison, branching ratios of 87 % to the yrast 1^+ state and 12 % to the T = 1 2^+ isobaric analogue state were predicted in the Rudolph study for the lowest-lying T = 0 2^+ state. The predicted strong branch from the 1161 keV state to the yrast 1^+ state at 571 keV is in excellent agreement with the experimental data. It is important to note that the lowest-lying non-yrast 1^+ state was not included in the branching predictions in the Rudolph calculation.

An assignment of 4^+ or 5^+ was reported for the state at 1439 keV in the Rudolph study. As discussed in Section 6.2.5, the anisotropy information regarding the 622 keV transition very strongly indicates E2 character in both the Rudolph work and the present study. The 1439 keV state is therefore assigned as 5^+. The existence of a 5^+ state at 1439 keV is in stark contrast to the theoretical predictions, as the lowest-lying non-yrast 5^+ state is predicted to have an excitation energy of at least 2.5 MeV. It was noted in the IBM-4 study that higher-spin (5^+ to 7^+) states are missing due to restrictions in the calculation [33]. The lack of a non-yrast 5^+ state at ~ 1.5 MeV indicates a clear deficiency with the theoretical models.

The newly observed 1575 keV state has a tentative $(2, 3^+)$ assignment. The 1575 keV level has been found to exhibit a 38(13) % branch to the 979 keV level, and a 62(29) % branch to the 1^+ 571 keV level. In comparison, the Rudolph calculation predicts a 94 % branch to the T = 1 2^+ state, and a 5 % branch to the yrast 1^+ state at 571 keV for the lowest-lying non-yrast 3^+ state. States with 2^+ and 3^+ assignments are predicted in the shell model, IBM-4 model and deformed shell model at $\sim 1.0 - 1.5$ MeV, in agreement with either the tentative J = 2 or 3^+ assignments proposed in the current study.

The candidate at 2237 keV for the T = 1 4^+ state exhibits branches that are broadly consistent with predicted branches from both the T = 1 4^+ isobaric analogue state, and a T = 0 4^+ state predicted at similar excitation energy. Both the T = 0 and T = 1 4^+ states are expected to decay to the 3^+ yrast state at 817 keV. More detailed branching information from the 2237 keV state, made possible with improved statistics, is therefore required before a definite assignment can be made.

In summary, consideration of the new results obtained in the present work, previous experimental studies and theoretical calculations allows a detailed picture of the low-lying structure of ^{62}Ga to be assembled. The 979 keV level is interpreted as the lowest-lying non-yrast 1^+ state, which has been long-predicted in theoretical calculations but never experimentally observed. The 1017 keV and 1161 keV states are interpreted as the lowest-lying T = 1 and T = 0 2^+ states, respectively. The 1^+ assignment for the 979 keV state and T = 1 2^+ assignment for the 1017 keV state are strongly supported by the results of a β-decay study of ^{62}Ge [73]. In terms of general features of both T = 0 and T = 1 states, it has been found that the IBM-4 model best reproduces the experimentally determined level scheme.

6.4 Double-β tagging and the search for transitions in ^{62}Ge

A search for transitions originating from the exotic $T_z = -1$ nucleus ^{62}Ge was carried out in the present work. In the experiments described in this thesis, ^{62}Ge, ^{62}Ga and ^{62}Zn nuclei were produced in the 2n, 1p1n and 2p heavy-ion fusion-evaporation channels, respectively. Predicted cross-sections of 9.7 mb for ^{62}Zn, 4.8 mb for ^{62}Ga and 20 μb for ^{62}Ge have been calculated using the heavy-ion fusion-evaporation code PACE4 in the LISE++ framework [102, 103]. The ratio of ^{62}Zn to ^{62}Ga cross-sections is predicted to be 2:1 and the ratio of ^{62}Ga to ^{62}Ge cross-sections is predicted to be 240:1.

^{62}Ge nuclei undergo superallowed β decays to ^{62}Ga with a half-life of 129(35) ms [47]. ^{62}Ga nuclei also undergo superallowed β decays, with a half-life of 116.121(21) ms [45]. ^{62}Zn has a $\sim$ 9 hour half-life. All of the spectra shown in Sections 6.1 and 6.2 were generated using a 'single-β tag', which selects events where a single β particle was detected in close proximity to implanted residues in the DSSD within 400 ms of implantation. As ^{62}Ge is the only reaction product that exhibits two successive superallowed β decays, a 'double-β tag' can be implemented in order to provide selectivity on ^{62}Ge nuclei. As ^{62}Zn is the mirror nucleus of ^{62}Ge, isospin symmetry dictates that the structure of the two nuclei are extremely similar. In particular, the vast majority of the γ-ray cascades in ^{62}Ge will feed the first excited 2^+ state, which then feeds the ground state directly. The $2^+ \rightarrow 0^+$ transition in ^{62}Ge is expected to be very close in energy (typically within tens of keV) to the 954 keV $2^+ \rightarrow 0^+$ transition in ^{62}Zn.

Figure 6.27a) shows the spectrum of γ rays, in the energy region of interest, measured in coincidence with reaction products that were subsequently correlated with a single β particle within two nearest neighbours in the DSSD within 400 ms of implantation. Figure 6.27b) shows the spectrum of γ rays measured in coincidence with reaction products that exhibit a 'double-β' event in the DSSD. A two nearest neighbour double-β event consists of the detection of two β particles in the DSSD, both within two nearest neighbours of the implanted reaction product, with the first β decay detected within 400 ms of the recoil implantation, and the second β decay detected within 400 ms of the first decay. The spectra shown in Figure 6.28 were produced in the same way as those presented in Figure 6.27, except that correlations were made using one nearest neighbour.

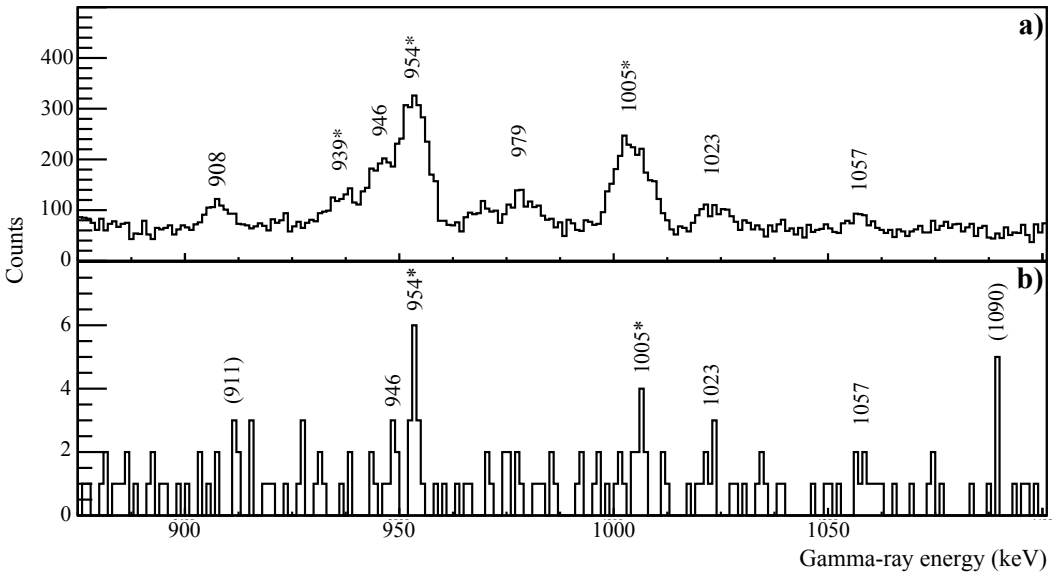

Figure 6.27 a) Single-β spectrum, using 2 nearest neighbour correlations. b) Double-β spectrum, using 2 nearest neighbour correlations. Transitions marked with a star originate from ^{62}Zn or ^{58}Ni.

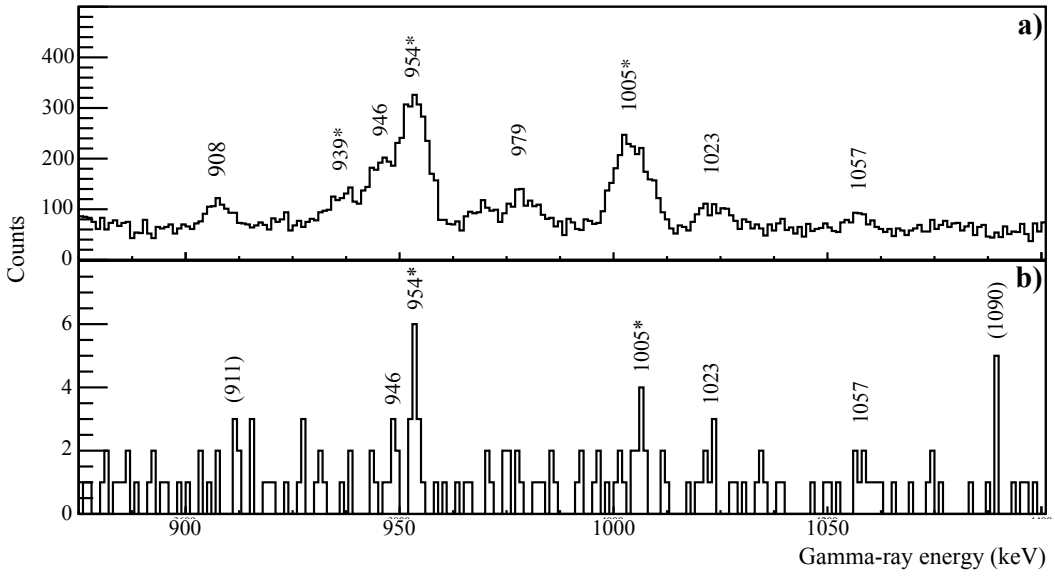

Figure 6.28 a) Single-β spectrum, using 1 nearest neighbour correlations. b) Double-β spectrum, using 1 nearest neighbour correlations. Transitions marked with a star originate from ^{62}Zn or ^{58}Ni.

Transitions marked with a star in Figures 6.27 and 6.28 originate from long-lived or stable contaminants. The 954 and 939 keV transitions originate from ^{62}Zn and the 1005 keV transition originates from ^{58}Ni. The 1005 keV peak is broad as the Doppler correction was applied for nuclei with mass 62. Transitions at 908, 946, 979, 1023 and 1057 keV originate from the short-lived nucleus ^{62}Ga. Although levels of contamination from long-lived or stable species are reduced by a factor of ~ 3 when incorporating one neighbouring pixel in implant-decay correlations compared to two neighbouring pixels, the intensity of transitions originating from true short-lived nuclei is dependant only on the β-particle detection efficiency, which is 20 % for 2NN correlations and 13 % for 1NN correlations.

Strong transitions in the 2NN single-β spectrum in Figure 6.27a) are also present in the 2NN double-β spectrum in Figure 6.27b). As ^{62}Ga emits one β particle, only one randomly correlated β particle is required for ^{62}Ga transitions to appear in the double-β spectrum, whereas long-lived species require two randomly correlated β particles to appear. Transitions originating from ^{62}Ga are therefore somewhat enhanced with respect to transitions originating from long-lived or stable contaminants in the double-β spectrum compared with the single-β spectrum. There are 4 counts at 911 keV and 5 counts at 1090 keV in the spectrum shown in Figure 6.27b), which are the only possible candidates for the $2^+ \rightarrow 0^+$ transition in ^{62}Ge and are labelled in brackets. The efficiency for detecting two successive β decays from ^{62}Ge is 4 % (20 % for each of the decays), whereas the efficiency of detecting **either** the first **or** the second β decay from ^{62}Ge is 40 %. The intensity of a transition from ^{62}Ge would therefore appear at 10 times the intensity in the single-β spectrum compared with the double-β spectrum. This implies that ~ 40 counts at 911 keV or ~ 50 counts at 1090 keV would appear in Figure 6.27a) if either of the transitions originate from ^{62}Ge, which is not the case.

The double-β spectrum shown in Figure 6.28b) is extremely clean as the probability of randomly correlating two β particles with a long-lived or stable species within only one neighbouring pixel in the DSSD is very small. The candidate transitions at 911 and 1090 keV are labelled in brackets. The β-particle detection efficiency is 13 % for 1NN correlations. The efficiency for the detection of two successive decays is therefore 1.7 %, whereas the detection efficiency for either the first or second decay is 26 %. ~ 45 counts at 911 keV or ~ 30 counts at 1090 keV would be expected to appear in the single-β spectrum in Figure 6.28a) if either of the transitions originate from ^{62}Ge, which is not the case.

Although it is very difficult to obtain precise values of absolute cross-sections in the current work, a ratio of the cross-section of ^{62}Zn to the cross-section of ^{62}Ga of 20:1 has been estimated. The yield of ^{62}Zn nuclei was estimated by assuming that 100 % of the produced ^{62}Zn nuclei emitted γ-ray cascades that fed through the $2^+ \rightarrow 0^+$ 954 keV transition. This assumption is justified as only one transition, which is weak compared with the 954 keV transition, feeds the ground state other than the 954 keV transition. The number of counts in the 954 keV peak was therefore used as an estimate of the total number of ^{62}Zn nuclei produced, after accounting for γ-ray detection efficiency and the transmission efficiency of the FMA. For the ^{62}Ga nuclei, it was assumed that 100 % of the ^{62}Ga nuclei produced emitted cascades that fed through the $1^+ \rightarrow 0^+$ 571 keV transition, which is justified as the vast majority of the transitions identified in ^{62}Ga have been found to feed through the 1^+ yrast state. The number of counts in the 571 keV peak was obtained from the β-tagged γ-ray spectrum, and multiplied by a factor of 1.5, estimated from the Rudolph work, to account for intensity loss due to the isomeric nature of the yrast 3^+ state at 817 keV. The γ-ray detection efficiency, β-particle detection efficiency and FMA transmission efficiency was then taken into account. An upper limit of $\sim$ 300 nb was estimated for the ^{62}Ge cross-section, obtained by assuming an upper limit of 5 counts in the $2^+ \rightarrow 0^+$ isobaric analogue transition to the 954 keV transition in ^{62}Zn in the 1NN double-β spectrum shown in Figure 6.28b). The 300 nb limit implies that the cross-section ratio of ^{62}Ga to ^{62}Ge is at least 80:1.

Chapter 7

Conclusions and outlook

A powerful new experimental system has been successfully developed at the ATLAS facility at the Argonne National Laboratory (ANL). The new system is designed to provide enhanced selectivity on exotic proton-rich nuclei, produced in heavy-ion fusion-evaporation reactions, that exhibit β decays on a timescale much faster than contaminant species. Prompt γ rays were detected by the Gammasphere array and recoiling reaction products were dispersed by their mass-to-charge ratio by the fragment mass analyzer (FMA) and implanted into a highly segmented 160×160 double-sided Silicon strip detector (DSSD). The very high degree of DSSD granularity allowed unstable reaction products to be correlated with their subsequent decays thereby providing a means to 'tag' species with short β-decay half-lives.

Several states in the exotic odd-odd N = Z nucleus ^{62}Ga have been newly observed in an experiment carried out using the new system. Self-conjugate nuclei are of great interest in nuclear structure physics as protons and neutrons occupy the same orbitals, amplifying shell effects and providing an ideal laboratory for studies of isospin symmetry-breaking. Proton-rich nuclei with N $\sim$ Z also lie along the path of the astrophysical rp-process and therefore critically affect the reaction path in explosive scenarios such as novae and X-ray bursts. In the present work, ^{62}Ga nuclei were produced via the evaporation of one proton and one neutron in heavy-ion fusion-evaporation reactions between accelerated ^{40}Ca ions and a ^{24}Mg target. ^{62}Ga has a half-life of 116 ms, whereas the main contaminant species produced were ^{62}Zn, which has a $\sim$ 9 hour half-life, and ^{58}Ni, which is

stable. The results presented in Chapter 6 include many low-lying transitions not observed in any previous studies despite having fewer statistics than, for example, an extensive study by Rudolph *et al.* in 2004. A sufficiently clean 'singles' γ-ray spectrum of ^{62}Ga has been produced in the current study for the first time. The new system has afforded the first observations of many weak non-yrast transitions or transitions that feed the ground state directly.

A strong transition was observed at ∼980 keV in an experiment designed to test the new experimental system. Low levels of statistics prevented the origin of the transition to be identified, although it was deduced that the transition must originate from a short-lived nucleus as the β-decay half-life associated with the γ-ray transition was $\sim$ 100 ms. The 979 keV transition was also observed in the more extensive secondary experiment, and was found to feed the 0^+ ground state directly from a newly observed 1^+ level at 979 keV in ^{62}Ga. The lowest-lying T = 0 2^+ state at 1161 keV in ^{62}Ga has been observed for the first time in the present study, and was found to exhibit branches to both the first excited yrast 1^+ state at 571 keV and to the newly identified 1^+ state at 979 keV. Several other newly observed levels at higher excitation are also reported in the current work. A state at 1017 keV, previously identified in the study by Rudolph *et al.* and proposed as a candidate for the T = 1 isobaric analogue state to the 2^+ state at 954 keV in ^{62}Zn, was also observed in the present work. The observation of γ-ray transitions at 978 and 1017 keV in a β-decay study of ^{62}Ge by Grodner *et al.* [73] provides strong supporting evidence for the 1^+ and T = 1 2^+ natures of the 979 and 1017 keV states, respectively.

The detailed implications of the newly obtained structure information regarding ^{62}Ga are beyond the scope of this thesis but are being investigated in theoretical frameworks in separate work. However, the substantial extension of the low-lying level scheme of ^{62}Ga reported in the current work allows a comparison to be made between theoretical predictions. A low-lying non-yrast 1^+ state has been long predicted by all of the models discussed in this thesis. A study by Petermann *et al.* that calculated Gamow-Teller strengths of states in ^{62}Ga reported a 1^+ state at just less than 1 MeV, in excellent agreement with the experimentally determined excitation energy of 979 keV. The predicted Gamow-Teller strengths of the first two excited 1^+ states are in agreement with the measured Gamow-Teller strengths of the 571 and 979 keV levels observed in the Grodner study [101]. Three theoretical studies that calculated excitation energies of low-lying T = 0 and T = 1 levels in ^{62}Ga using the shell model [43], IBM-4 model [33] and

deformed shell model [32] demonstrated the correct ordering of the first four T = 0 states (1^+, 3^+, 1^+, 2^+). However, the deformed shell model predicts an excitation energy rather too low for the T = 1 2^+ isobaric analogue state, which is incorrectly thought to lie between the yrast 1^+ and 3^+ states, whereas both the shell model and IBM-4 calculation correctly predict that the T = 1 2^+ state lies between the lowest-lying non-yrast 1^+ state and the lowest-lying T = 0 2^+ state. A general trend seen in all of the models discussed is that the levels are typically $\sim$ 200 keV lower in excitation than the experimentally determined values. It is determined that the IBM-4 calculation best reproduces the experimental results.

Despite the major extension to the low-lying level scheme of ^{62}Ga reported in this thesis work, the precise nature of some of the newly observed states remain tentative. Unambiguous anisotropy information for many of the transitions, made possible with an increased level of statistics, would allow definite assignments for the level at 1575 keV, which has a tentative $(2, 3^+)$ assignment, and higher-lying levels at 2212, 2989 and 3796 keV. An increased level of statistics would also allow branching information between T = 0 and T = 1 states to be obtained, and the precise nature of the candidate level at 2237 keV for the isobaric analogue state of the 4^+ level at 2186 keV in ^{62}Zn to be identified. The 1017 keV γ ray observed in the Grodner β-decay study has yet to be observed in an in-beam γ-ray experiment. The ability to produce 'singles' spectra, demonstrated with the new experimental system, would be required to observe the 1017 keV transition, as this transition would not be in coincidence with any known transitions. A ^{62}Ge β-decay study with high levels of statistics, thus enabling a γ-ray coincidence analysis of transitions in ^{62}Ga following non-analogue β decays of ^{62}Ge, would provide yet more detailed information regarding low-spin states in ^{62}Ga.

Predictions of the branching ratios of several of the low-lying states in ^{62}Ga were reported in the work by Rudolph *et al.* The calculation suggested that the E2 transition to the ground state from the T = 1 2^+ level dominates over the M1 transition to the yrast 1^+ state at 571 keV. Precise measurements of the branching ratios from the T = 1 2^+ isobaric analogue level would therefore be of significant interest. A new calculation of branching ratios of low-lying levels in ^{62}Ga, including the 1^+ 979 keV state, would be of considerable interest in light of the findings in the present study.

The experimental system described in this thesis is very well suited to studies of several other proton-rich nuclei with N $\sim$ Z as well as ^{62}Ga. Newly observed transitions have been identified in preliminary results of a study of the odd-odd

N = Z nucleus ^{66}As carried out by the Edinburgh Nuclear Physics Group using the new system developed at Argonne [104]. The system is also ideally suited to studies of nuclei in the region of the doubly-magic nucleus ^{100}Sn. As discussed in Section 6.4, the system can be used to provide extremely high levels of selectivity on nuclei that exhibit two successive fast β decays, such as the $T_z = -1$ nuclei ^{62}Ge, ^{66}Se, ^{70}Kr and ^{74}Sr. No information regarding excited states has been determined for ^{62}Ge, ^{70}Kr or ^{74}Sr, and only the $2^+ \rightarrow 0^+$ transition in ^{66}Se has been identified [28]. The technique of recoil-β tagging has been successfully developed at the Jyväskylä laboratory and used to study the N = Z nuclei ^{78}Y and ^{74}Rb [41, 88], and searches for transitions in ^{70}Kr and ^{74}Sr using 'double-β tagging' are planned to be carried out using a similar system [105]. The development of radioactive beam facilities has opened up new opportunities for studying exotic proton-rich nuclei using reactions other than heavy-ion fusion-evaporation reactions in recent years. For example, a high energy secondary beam of radioactive ^{57}Cu ions was produced using a primary beam of ^{58}Ni in a very recent experiment at the National Superconducting Cyclotron Laboratory (NSCL) that studied excited states in the $T_z = -1$ nucleus ^{58}Zn using (d, n) reactions [106]. This was made possible as the ^{57}Cu + d pickup reaction had previously been observed to be unusually strong, so this reaction mechanism is not necessarily applicable to many cases. Nevertheless, new radioactive beam facilities will certainly provide exciting opportunities to probe the structure of exotic proton-rich nuclei using a variety of reactions.

In summary, a powerful experimental system has been developed at ANL that provides high levels of selectivity on exotic proton-rich nuclei. Several low-lying levels in ^{62}Ga have been observed for the first time in an experiment carried out using the new system, and comparisons made between theoretical predictions. The system is ideal for structure studies of proton-rich nuclei that exhibit β decays on a timescale much faster than contaminant species. The development of innovative experimental techniques, such as single- and double-β tagging, and radioactive beam facilities has opened up exciting opportunities for exploring exotic nuclei at the limits of stability.

Appendix A

Half-life measurements

Full details of the method used to measure the β-decay half-lives associated with the γ-ray transitions observed in singles spectra are given in Section 5.5. Values of the β-decay half-life, $\tau_{1/2}$, associated with each γ-ray transition, E_γ, are listed in Table A.1. The excitation energy, E_x, of the energy levels from which the γ rays originate from are also given in Table A.1 for reference. Precise energies for the 571 and 817 keV states (and the energies of transitions de-populating these states) could not be obtained in the present work due to Doppler effects caused by the isomeric nature of the yrast 3^+ state at 817 keV. Transitions in brackets have been observed either in singles or coincidence spectra and could not be unambiguously placed in the level scheme on the basis of the current results, but have been tentatively placed in the scheme based on previous observations by Rudolph *et al.*

The half-life of ^{62}Ga was measured to be 116.5(13) ms in the current work, determined by taking the weighted average of the $\tau_{1/2}$ values listed in Table A.1. This value is in agreement with the world-averaged value of 116.121(21) ms.

E_x (keV)	E_γ (keV)	$\tau_{1/2}$ (ms)
~ 571	~ 571	112(3)
~ 817	~ 246	115(3)
978.8(4)	978.8(4)	133(17)
1017.1(7)	445.9(7)	-
1161.0(3)	182.8(1)	155(71)
	589.5(3)	112(13)
1192.9(2)	375.7(1)	119(2)
1439.1(2)	621.9(2)	104(14)
1575.1(7)	595.9(9)	113(47)
	1004.4(11)	154(75)
2211.5(5)	1232.7(3)	-
2237.3(17)	1420.1(17)	-
2373.8(4)	(935.3(4))	173(49)
	1179.4(7)	153(27)
2433.5(3)	1240.6(2)	116(5)
2672.4(7)	1510.1(15)	191(72)
2989.4(9)	1796.5(9)	98(29)
3012.7(7)	340.1(3)	106(24)
	(640.8(22))	-
3491.4(5)	478.3(11)	-
	1057.4(5)	133(28)
	(1120.3(12))	-
3795.7(7)	1362.2(7)	181(44)
3920.2(5)	907.6(5)	104(21)
	1486.9(5)	123(12)
4656.4(9)	1165.5(7)	121(19)
4789.2(7)	(866.7(10))	-
	2355.7(6)	118(9)
4943.2(7)	1023.0(5)	107(16)
5735.0(7)	945.8(3)	112(11)
6841.5(8)	1106.5(4)	126(12)
8587.7(11)	1746.2(8)	97(14)
9977.4(15)	1389.7(9)	151(37)

Table A.1 Inferred β-decay half-lives associated with γ-ray transitions measured in singles spectra. Precise energy measurements for the 571 and 246 keV transitions (and therefore the excitation energies of the 571 and 817 keV levels) were not possible in the current work due to Doppler effects. The weighted average of the listed $\tau_{1/2}$ values gives a determined half-life of ^{62}Ga of 116.5(13) ms.

Bibliography

[1] P. J. Woods and C. N. Davids. *Annual Review of Nuclear and Particle Science* **47**, 541 (1997).

[2] H. Sakurai *et al. Physics Letters B* **448**, 180 (1999).

[3] I. Tanihata *et al. Physical Review Letters* **55**, 2676 (1985).

[4] K. Tanaka *et al. Physical Review Letters* **104**, 062701 (2010).

[5] I. Tanihata. *Journal of Physics G: Nuclear and Particle Physics* **22**, 157 (1996).

[6] I. Tanihata, H. Savajols, and R. Kanungo. *Progress in Particle and Nuclear Physics* **68**, 215 (2013).

[7] `http://www.ornl.gov/info/ornlreview/v39_3_06/article24.shtml`.

[8] C. R. Hoffman *et al. Physics Letters B* **672**, 17 (2009).

[9] P. D. Cottle and K. W. Kemper. *Physics* **5**, 49 (2012).

[10] R. Wadsworth *et al. Acta Physica Polonica B* **40**, 3 (2009).

[11] E. Bouchez *et al. Physical Review Letters* **90**, R1175 (2003).

[12] M. Bender *et al. Physical Review C* **74**, 024312 (2006).

[13] E. Clement *et al. Physical Review C* **75**, 054313 (2007).

[14] S. M. Fischer *et al. Physical Review Letters* **84**, 4064 (2000).

[15] J. Ljungvall *et al. Physical Review Letters* **100**, 102502 (2008).

[16] K. Miernik *et al. Physical Review C* **76**, 041304(R) (2007).

[17] M. Pfützner and M. Karny. *Review of Modern Physics* **84**, April-June (2012).

[18] C. B. Hinke *et al. Nature* **486**, 351 (2012).

[19] `http://www.nscl.msu.edu/~schatz/`.

[20] M. Smith and K. E. Rehm. *Annual Review of Nuclear and Particle Science* **51**, 91 (2001).

[21] H. Schatz *et al. Nuclear Physics A* **654**, 924c (1999).

[22] R. K. Wallace and S. E. Woosley. *Astrophysical Journal Supplement Series* **45**, 389 (1981).

[23] H. Schatz *et al. Physics Reports* **294**, 167 (1998).

[24] A. Parikh, J. Josè, F. Moreno, and C. Illiadis. *New Astronomy Reviews* **52**, 409 (2008).

[25] T. Strohmayer and L. Bildsten. *Compact Stellar X-ray Sources*, Ed. W. H. G. Lewin and M. van der Klis, Cambridge Univ. Press, p. 113 (2006).

[26] `http://www.sciencedaily.com/releases/2005/07/050715070053.htm`. Credit: NASA/Dana Berry.

[27] R. Boyd. *Journal of Physics G: Nuclear and Particle Physics* **24**, 1617 (1998).

[28] A. Obertelli *et al. Physics Letters B* **701**, 417 (2011).

[29] W. Hauser and H. Feshbach. *Physical Review* **87**, 366 (1952).

[30] A. B. Garnsworthy *et al. Physical Review C* **80**, 064303 (2009).

[31] D. Rudolph *et al. Physical Review C* **69**, 034309 (2004).

[32] R. Sahu and V. K. B. Kota. *Physical Review C* **66**, 024301 (2002).

[33] O. Juillet, P. Van Isacker, and D. D. Warner. *Physical Review C* **63**, 054312 (2001).

[34] A. B. Garnsworthy *et al. Physics Letters B* **660**, 326 (2008).

[35] M. A. Bentley and S. M. Lenzi. *Progress in Particle and Nuclear Physics* **59**, 497 (2007).

[36] S. M. Lenzi *et al. Physical Review C* **60**, 021303 (1999).

[37] C. D. O'Leary *et al. Physics Letters B* **525**, Issues 1-2, p 49 (2002).

[38] D. Rudolph *et al. The European Physics Journal A* **4**, 115 (1999).

[39] G. de Angelis *et al. Physical Review C* **85**, 034320 (2012).

[40] D. G. Jenkins *et al. Physical Review C* **65**, 064307 (2002).

[41] B. S. Nara Singh *et al. Physical Review C* **75**, 061301R (2007).

[42] G. de Angelis *et al. Nuclear Physics A* **630**, 426 (1998).

[43] S. M. Vincent *et al. Physics Letters B* **437**, 264 (1998).

[44] E. S. Paul *et al. Physical Review C* **51**, 1 (1995).

[45] G. Grinyer *et al. Physical Review C* **77**, 015501 (2008).

[46] I. S. Towner and J. C. Hardy. *Physical Review C* **77**, 025501 (2008).

[47] M. J. Lòpez Jimènez. *Physical Review C* **66**, 025803 (2002).

[48] J. Erler *et al. Nature* **486**, 509 (2012).

[49] `http://noblegas.berkeley.edu/~noblegas/courses.html`.

[50] `http://cnx.org/content/m42640/1.5/`.

[51] B. Alex Brown. *Lecture notes in Nuclear Structure Physics*. NSCL (2005).

[52] A. Juodagalvis and S. Åberg. *Nuclear Physics A* **683**, 207 (2001).

[53] G. M. Temmer. *Reviews of Modern Physics* **30**, p498 (1958).

[54] K. C. Tripathy and R. Sahu. *Journal of Physics G: Nuclear and Particle Physics* **26**, 1271 (2000).

[55] D. P. Ahalpara *et al. Journal of Physics G: Nuclear and Particle Physics* **11**, 735 (1985).

[56] A. Arima and F. Iachello. *Physics Review Letters* **35**, 1069 (1975).

[57] E. Baldini-Neto *et al. Brazilian Journal of Physics* **33**, 2 (2003).

[58] G. Lotay *et al. Physical Review C* **84**, 035802 (2011).

[59] A. O. Macchiavelli *et al. Physical Review C* **61**, 041303(R) (2000).

[60] A. O. Macchiavelli *et al. PINGST 2000, Selected topics on N=Z nuclei*, 156 (2000).

[61] A. Bohr and B. R. Mottelson. *Nuclear Structure*. Benjamin-New York (1975).

[62] K. S. Krane. *Introductory Nuclear Physics*. John Wiley and Sons (1988).

[63] J. Lilley. *Nuclear Physics: Principles and Applications*. Wiley (2009).

[64] E. Fermi. *Zeitschrift für Physik* **88**, 161, (1934).

[65] E. Poirier *et al. Physical Review C* **69**, 034307 (2004).

[66] K. Schreckenbach *et al. Physics Letters B* **349**, 427 (1995).

[67] C. Rossi Alvarez. *Nuclear Physics News* **3**, 3 (1993).

[68] E. Farnea *et al. Nuclear Instruments and Methods in Physics Research A* **400**, 87 (1997).

[69] H. Grawe *et al. Zeitschrift für Physik A* **358**, 185 (1997).

[70] M. P. Carpenter. *Zeitschrift für Physik A* **358**, 261 (1997).

[71] A. Krämer-Flecken *et al. Nuclear Instruments and Methods in Physics Research A* **275**, 333 (1989).

[72] J. Gellanki *et al. Physical Review C* **80**, 051304(R) (2009).

[73] E. Grodner *et al. GSI Scientific Reports*, NUSTAR-EXPERIMENTS-16 (2009).

[74] H. Geissel *et al. Nuclear Instruments and Methods in Physics Research B* **70**, 286 (1992).

[75] H. Wollersheim *et al. Nuclear Instruments and Methods in Physics Research A* **537**, 637 (2005).

[76] J. Eberth *et al. Nuclear Instruments and Methods in Physics Research A* **369**, 135 (1996).

[77] S. Pietri *et al. Nuclear Instruments and Methods in Physics Research B* **261**, 1079 (2007).

[78] I. Petermann *et al. European Physical Journal A* **34**, 319 (2007).

[79] M. Hjorth-Jensen *et al. Physics Reports* **261**, 125 (1995).

[80] T. T. S. Kuo. Private Communication (1969).

[81] E. Caurier *et al. Physical Review Letters* **77**, 1954 (1996).

[82] K. A. Brueckner. *Physical Review* **97**, 1353 (1955).

[83] J. Goldstone. *Proceedings of the Royal Society A* **293**, 267 (1957).

[84] H. A. Bethe, B. H. Brandow, and A. G. Petschek. *Physical Review* **129**, 225 (1963).

[85] E. Caurier *et al.* Shell model code antoine. CRN, Strasbourg (1989).

[86] E. Caurier and F. Nowacki. *Acta Physica Polonica B* **30**, 705 (1999).

[87] K. C. Tripathy and R. Sahu. *Journal of Physics G: Nuclear and Particle Physics* **26**, 1271 (2000).

[88] A. N. Steer *et al. Nuclear Instruments and Methods in Physics Research* **A565**, 630 (2006).

[89] A. N. Deaken. Ph.D. thesis (2006).

[90] http://nucalf.physics.fsu.edu/~riley/gamma/.

[91] R.-D. Herzberg and P. T. Greenlees. *Progress in Particle and Nuclear Physics* **61**, 2 (2008).

[92] http://www.micronsemiconductor.co.uk.

[93] http://spie.org/x20060.xml.

[94] J. T. Anderson *et al. IEEE Transactions on Nuclear Science* **56**, 1 (2009).

[95] http://root.cern.ch/.

[96] http://radware.phy.ornl.gov/.

[97] T. Steinhardt. Diploma Thesis, University of Cologne (1997).

[98] P. Finlay *et al. Physical Review C* **78**, 025502 (2008).

[99] A. K. Singh *et al. Physical Review C* **59**, 5 (1999).

[100] S. Mohammadi *et al. Journal of Physics G: Nuclear and Particle Physics* **25**, 909 (1999).

[101] A. Gadea. GT decays into N = Z nuclei with A $\sim$ 50 − 60. RISING celebration day and HISPEC/DESPEC meeting, Darmstadt (October 2009).

[102] A. Gavron. *Physical Review C* **21**, 230 (1980).

[103] O. B. Tarasov and D. Basin. *Nuclear Instruments and Methods in Physics Research Section B* **204**, 174 (2003).

[104] H. M. David. Private Communication (2013).

[105] R. Wadsworth, D. Jenkins, *et al.* Identification of excited states in ^{70}Kr and ^{74}Sr. Research proposal, Jyväskylä laboratory.

[106] C. Langer. Important excitation energies of ^{58}Zn for the rp-rocess. Workshop on Future GRETINA Science Campaigns, Argonne National Laboratory (2013).